ALGERIAN DEMOCRATIC AND POPULAR REPUBLIC
MINISTRY OF HIGHER EDUCATION AND SCIENTIFIC RESEARCH

ABDELHAMID IBN BADIS UNIVERSITY - MOSTAGANEM FACULTY
OF SCIENCE AND TECHNOLOGY
DEPARTMENT OF ELECTRICAL ENGINEERING

THESIS

PRESENTED TO OBTAIN

LMD DOCTORATE DEGREE

Specialty: Electronics

Option: Microelectronics and Embedded Microsystems

By

AISSANI Ali

COMPARATIVE STUDY OF THE STRUCTURAL, ELECTRONIC, OPTICAL, AND THERMOELECTRIC PROPERTIES OF A SERIES OF NEW LEAD-FREE PEROVSKITE MATERIALS

(APPLICATION TO EMBEDDED SYSTEMS)

Publicly defended on 05/05/2025 before the jury composed of:

Zoubir AZIZ	Professor	Chair	UMAB - Mostaganem
HADRI Baghdad	Professor	Examiner	UMAB - Mostaganem
ZITOUNI Ali	Professor	Examiner	UMAB - Mostaganem
BENTATA Rachida	Professor	Examiner	Université de Mascara
BESBES Anissa	Professor	Supervisor	UMAB - Mostaganem
DJELTI Radouane	Professor	Co-Supervisor	UMAB - Mostaganem

Academic Year: 2025-2026

Acknowledgement

First and foremost, all praise and gratitude are due to Almighty Allah, the Most Compassionate and Most Merciful, whose infinite blessings, guidance, and mercy granted me the strength, perseverance, and determination to accomplish this work.

I would like to express my deepest gratitude to my supervisors, **Prof. Djelti Radouane** and **Prof. Besbes Anissa**, for their continuous guidance, valuable advice, scientific support, and constant encouragement throughout this research. Their expertise and dedication greatly enriched both this dissertation and my academic journey.

My sincere thanks are also extended to the **Technology and Solids Properties Laboratory**, Faculty of Science and Technology, University of Mostaganem, for providing an excellent scientific environment and research facilities. I am especially grateful to the director of the laboratory, **Prof. Bouadjemi Bouabdellah**, for his support and encouragement. I would also like to thank all laboratory members, particularly **Mrs. Kheira Hammou** and **Prof CHERID Samira, Dr. Benosmane Sara**, for their collaboration, kindness, and valuable assistance.

I am deeply honored to thank the distinguished members of the thesis examination committee: **Prof. Zoubir AZIZ** Chair of the committee, **Prof. HADRI Baghdad**, **Prof. ZITOUNI Ali**, and **Prof. BENTATA Rachida**, for their time, insightful comments, and valuable recommendations that contributed significantly to improving this dissertation.

I would further like to express my appreciation to the **CFD**, **CSD**, and **CSF** committees, especially the Vice Dean Prof. Sardou Miloud and Mrs. Hezil Latifa, for their remarkable administrative support and professionalism throughout the thesis defense procedures.

My sincere gratitude also goes to the **Ministry of Higher Education and Scientific Research of Algeria**, the **Faculty of Science and Technology at the University of Mostaganem**, and **Ondokuz Mayıs University in Turkey** for supporting and facilitating my academic mobility and research internships. Special thanks are due to **Prof. Nacemi Dege** and **Dr. Ibrahim Inanc** for their scientific guidance and encouragement during my internship period. I am equally grateful to **Dr. Rakan Bashir**, **Mrs. Emine Berrin Poyraz**, and **Mr. Okan Simsek** for their kindness, friendship, and invaluable support.

Finally, I would like to express my heartfelt gratitude to my parents, family, friends, and everyone who supported and encouraged me throughout this academic journey. Their love, patience, and belief in me have been a constant source of motivation and strength.

Dedication

First and foremost, I express my deepest gratitude to Almighty Allah, the Most Gracious and Most Merciful, whose infinite blessings, guidance, and mercy have accompanied me throughout this journey. Without His will and support, none of this accomplishment would have been possible.

With profound respect and sincerity, I dedicate this work to all those who have been a source of strength, inspiration, and support.

I dedicate this thesis to my beloved **parents**, whose unconditional love, sacrifices, and unwavering encouragement have been the cornerstone of all my achievements. Their guidance, values, and constant support have shaped my character and sustained me throughout this academic path. I also extend this dedication to my **brother** and **sisters**, whose affection and presence have always reminded me that I was never alone.

I am sincerely grateful to my supervisors, **Prof. Djelti Radouane** and **Prof. Anissa Besbes**, for their invaluable guidance, scientific insight, and continuous support, which were essential to the completion of this work and to my academic development.

I also extend my heartfelt appreciation to **Dr. Ouendadji Salima** for her valuable support, encouragement, and assistance throughout this academic journey.

I would like to acknowledge with respect my teachers and sheikhs who taught me the Holy Qur'an, whose wisdom and teachings have profoundly shaped my values and character.

My sincere gratitude goes to my dear friends, **Dr Lakhdar Benahmedi**, **Sidahmed Bendehiba**, **Imad Brahmi**, and **Samia Moulebhar**, whose loyalty, friendship, and constant encouragement have been a true source of strength and balance throughout this journey.

I am also deeply grateful to my PhD colleagues of the 2023 promotion—**Hamdi Cherif Mohammed**, **Mechehoud Noureddine**, **Messaoudi Abdelkarim**, **Bentahar Heythem**, **Khatar Abdelhak**, **Hamiche Korichi**, **Sarra Merabet**, **Righi Aya**, **Mechehoud Khedidja**, **Khantar Sidahmed**, and **Bilel Achir**—as well as colleagues from other promotions, including **Aissa Guesmia**, **Kessas Mohammed**, **Omar Belarbi**, **Amina Lahouali**, and **Fatima Zohra Benaouina**, for their companionship and support.

I also extend my appreciation to **Mrs. Kheira Hammou**, **Dr. Benosmane Sara**, **Dr. Mohammed Amine Boudjeltia**, **Dr.Kheira Bahnes**, and **Dr. Noureddine Saidi** for their guidance and encouragement.

Finally, I extend my sincere gratitude to all those who, in one way or another, have contributed, supported, or encouraged me throughout this journey.

TABLE OF CONTENTS

LIST OF FIGURES

LIST OF TABLES

NOMENCLATURE

ABX_3: General perovskite formula
$A_2BB'X_6$: Double perovskite formula
Ψ: Wave function
$\hat{H}$: Hamiltonian operator
E: Energy eigenvalue
Te: Total kinetic energy of electrons
Tn: Total kinetic energy of nuclei
Vee: Electron–electron interaction energy
Vnn: Nucleus–nucleus interaction energy
Ven: Electron–nucleus interaction energy
ħ: Reduced Planck's constant
∇^2: Laplacian operator
e: Elementary charge
ε_0: Vacuum permittivity
ρ(r): Electron density
Ne: Total number of electrons
E[ρ]: Total energy functional
F[ρ]: Universal functional (T+Vee)
Exc[ρ]: Exchange–correlation functional
Vext: External potential
φi(r): Kohn–Sham orbital
εi: Kohn–Sham eigenvalue
Veff(r): Effective potential
HF: Hartree–Fock approximation
SCF: Self-consistent field
DFT: Density Functional Theory
XC: Exchange–Correlation
LDA: Local Density Approximation
LSDA: Local Spin Density Approximation
GGA: Generalized Gradient Approximation
PBE: Perdew–Burke–Ernzerhof functional
PBEsol: PBE for solids
mBJ: Modified Becke–Johnson potential
DFT+U: DFT with Hubbard correction
APW: Augmented Plane Wave method
LAPW: Linearized Augmented Plane Wave method
FP-LAPW: Full-Potential Linearized Augmented Plane Wave
Ry: Rydberg unit of energy
C_{ij}: Elastic stiffness constants
U: Elastic strain energy per unit volume
B: Bulk modulus
G: Shear modulus
E: Young's modulus
ν: Poisson's ratio
A: Elastic anisotropy factor
B/G: Pugh ratio
CP: Cauchy pressure
DFT: Density Functional Theory
h: Thomson coefficient
E: Electric field
∇T: Temperature gradient
Q: Heat absorbed or released (Peltier effect)
I: Electric current
σ: Electrical conductivity
σ/τ: Electrical conductivity per relaxation time
κe: Electronic thermal conductivity
κL: Lattice thermal conductivity
κtot: Total thermal conductivity
τ: Relaxation time
J: Electrical current density
q: Heat current density
ε: Carrier energy
μ: Chemical potential
v(k): Carrier velocity (from band structure)
Ω: Unit cell volume
N_k: Number of k-points in sampling
ZT: Dimensionless thermoelectric figure of merit
Gth: Thermal conductance
W: Electrical work
BTE: Boltzmann Transport Equation
DOS: Density of States
ω: Angular frequency of the incident light
ε(ω): Complex dielectric function
$\varepsilon_1(\omega)$: Real part of dielectric function
$\varepsilon_2(\omega)$: Imaginary part of dielectric function
n(ω): Refractive index
k(ω): Extinction coefficient
α: Absorption coefficient
R(ω): Reflectivity
L(ω): Energy loss function
NIR: Near-Infrared region
VIS : Visible region
UV : Ultraviolet region
ε_0 (static): Static dielectric c

General Introduction

Perovskite-type materials occupy a central place in contemporary research in materials science and solid-state physics. First identified in 1839 by the mineralogist Gustav Rose, these compounds have steadily attracted growing interest due to their remarkable structural and functional versatility. Their archetypal crystal structure, denoted as ABX_3, where A and B represent cations and X is an anion (commonly oxygen or a halogen), serves as the foundation of an extraordinarily rich family of materials. This structure can be generalized to double perovskites of the $A_2BB'O_6$ type, in which two distinct cations occupy the B site, thereby enabling an even broader diversity of physical properties and functionalities.

One of the most compelling aspects of perovskites lies in the possibility of finely tuning their properties through cationic or anionic substitution. This tunability makes them particularly attractive for a wide range of strategic applications. For instance, in the field of photovoltaics, perovskite-based solar cells have achieved efficiencies exceeding 25% in less than two decades, a rate of progress unmatched by most other photovoltaic technologies. Beyond solar energy, these compounds also hold great promise in photonics and optoelectronics, where their strong light absorption and intense photoluminescence can be harnessed for efficient light-emitting devices and detectors. In addition, perovskites play an increasingly important role in energy storage and conversion technologies, whether as electrode materials for batteries or as redox-active catalysts. Certain members of this material family also exhibit noteworthy magnetic behaviors, opening the door to potential applications in spintronics, magnetic sensors, and multifunctional devices.

Despite these considerable advantages, perovskites still face two major obstacles that hinder their large-scale deployment. The first challenge is stability: many halide perovskites are prone to degradation when exposed to humidity, elevated temperatures, or prolonged light irradiation, which severely limits their long-term durability in devices. The second challenge concerns toxicity, particularly that of lead (Pb). The highest-performing halide perovskites generally contain lead, raising serious environmental and health concerns and creating barriers to their widespread industrial implementation.

In light of these challenges, significant research efforts are currently devoted to the development of alternative materials that are both lead-free and more stable, without sacrificing

high performance. In this context, theoretical ab initio methods, especially those based on density functional theory (DFT), provide a powerful framework for exploring and predicting the properties of new compounds prior to experimental synthesis. By employing DFT in combination with robust computational codes such as WIEN2k and BoltzTraP, it becomes possible to accurately evaluate a broad range of material characteristics, including structural, electronic, optical, elastic, and thermoelectric properties.

The present dissertation is firmly embedded within this research landscape. It offers a comparative study of oxide and halide perovskites, with the overarching goal of identifying lead-free compounds that combine structural stability with promising optoelectronic behavior and notable thermoelectric efficiency. More specifically, two families of materials are investigated: the simple oxide perovskites $CeBeO_3$ and $CeMgO_3$, and the halide double perovskites K_2BBiBr_6 (with B = Cu or Ag).

The manuscript is structured into five chapters. Chapter I presents the state of the art on simple and double perovskites, including a detailed overview of their crystallographic structures, stability criteria, main physical properties, synthesis techniques, as well as their most prominent applications and current scientific and technological challenges. Chapter II introduces the theoretical framework and computational methods employed, with particular emphasis on density functional theory, exchange correlation approximations, the full-potential linearized augmented plane wave (FP-LAPW) method, and their implementation within the WIEN2k code. Chapter III focuses on an in-depth investigation of the structural, electronic, optical, elastic, and thermoelectric properties of simple oxide perovskites. Chapter IV extends this analysis to halide double perovskites, examining their structural, electronic, mechanical, optical, and transport properties. Finally, Chapter V draws upon the insights gained throughout the thesis to discuss the prospects for integrating the studied materials into embedded systems, thereby bridging the gap between fundamental materials research and potential technological applications.

CHAPTER I

STATE OF THE ART ON SIMPLE AND DOUBLE PEROVSKITE

I.1 Introduction

Perovskites materials represent a unique class of inorganic crystalline solids that are widely recognized for their remarkable and varied physical properties. First discovered in 1839 by the German geologist Gustav Rose in the Ural Mountains of Russian **[1]**. Rose subsequently named this mineral in honor of Russian mineralogist Count Lev Alekseevich Von Pevosky (1792-1856) **[2]**. The significance of this discovery extends far beyond its historical origins. What began as a the identification of a single mineral has evolved into the recognition of an entire structural family encompassing thousands of compounds with the general formula ABX_3, where **A** and **B** represent cations of different sizes and **X** typically represents an anion, most commonly oxygen or halogen **[3]**. These compounds have become famous due to their fascinating material properties and their extensive applications, particularly in fields such as optoelectronics, catalysis, energy storage, and renewable energy technologies. Their versatility, ranging from high-performance photovoltaic devices to sensors and spintronic systems, makes them a central focus of modern materials research. **[4]**. **Figure I.1** represents natural perovskite mineral ($CaTiO_3$) crystal structure showing the characteristic cubic arrangement.

Figure I.1 Calcium Titanate Perovskite ($CaTiO_3$)

The typical perovskite crystal structure has drawn significant attention over the past decade, owing to its wide range of physical properties that have driven major advancements in various technological fields. For instance, these materials have demonstrated promising superconducting properties **[5]**, in addition to other exceptional characteristics such as high ionic conductivity and optical non-linearity **[6]**. Perovskites are generally classified into two categories: simple perovskites and complex perovskites, each of which exhibits distinct structural and functional attributes **[7]**.

I.2 Description of the simple perovskite structure

The simple perovskite structure is a highly efficient crystal configuration with a distinct atomic arrangement that influences its physical properties. In the perovskite structure, the **A** cation is typically large and occupies the corners of the unit cell, while the smaller **B** cation is located at the center, surrounded by six oxygen atoms arranged in an octahedral coordination. Oxygen atoms are positioned to form cubic and octahedral arrangements around the **A** and **B** cations, respectively. This arrangement leads to a stable and compact structure. Approximately 74% of the volume in a perovskite unit cell is occupied by atoms, leaving the remaining space unoccupied **[8]**. This packing efficiency indicates a tightly packed structure, which is crucial for the material's stability and its ability to accommodate different cations at both the **A** and **B** sites, enhancing its versatility in various applications. The atomic positions are typically defined as follows: **A** at **(0, 0, 0)**, **B** at **(0.5, 0.5, 0.5)** and **X** atoms (usually oxygen) at the positions **(0.5, 0.5, 0), (0.5, 0, 0.5)**, and **(0, 0.5, 0.5)** as shown in **Figure I.2**, **[9-10]**.

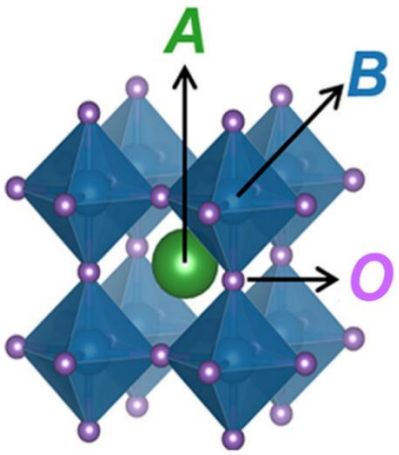

Figure I.2 Representation of the ABO_3 perovskite structure by the unit cell

I.2.1 From simple perovskite to double perovskite ($A_2BB'O_6$)

Double perovskites follow the general formula $A_2BB'O_6$, which results in a unit cell that is twice the size of a simple perovskite. This structure emerges from the combination of two materials, each having a perovskite-type framework, with one exhibiting an ABO_3 composition and the other an $AB'O_3$ composition. The ordered arrangement of the double perovskite $A_2BB'O_6$ is illustrated in **Figure I.3 [11]**. In this structure, each **B** or **B'** cation is surrounded by oxygen octahedra, with each **B** cation coordinating with six **B'** cations and vice versa. When there is a significant difference in the size or valence between the **B** and **B'** ions, they tend to occupy alternating positions in the crystal lattice. This results in an arrangement where **B**-type atoms are exclusively in contact with **B'**-type atoms, and vice versa, forming two interwoven

sublattices of BO_6 and $B'O_6$ octahedral. Other possible structural variations of double perovskites include $AA'B_2O_6$ or $AA'BB'O_6$. The versatility and adaptability of double perovskites, due to their unique atomic arrangement and the possibility of incorporating different cations at the **A**, **B** and **B'** sites, contribute to their potential applications in areas such as photocatalysis, magnetic materials and energy storage **[12-13]**. Their structure can also accommodate various substitutions, allowing for fine-tuning of their electronic and optical properties, which makes them particularly attractive for optoelectronic devices and solar energy applications **[14-15]**.

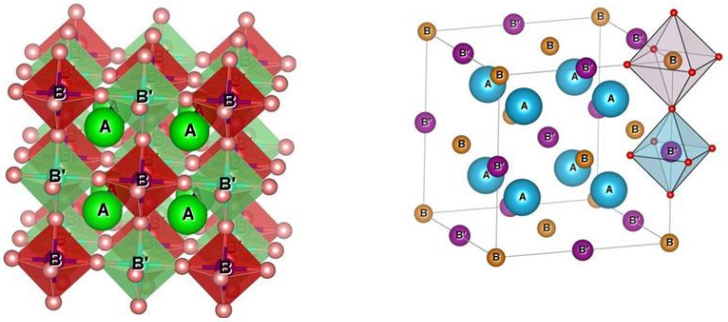

Figure I.3 Unit cell of the ordered double perovskite ($A_2BB'O_6$)

I.3 The structural stability of perovskites

In an ideal perovskite structure, the ions are in contact with each other, and the BX_6 octahedra are perfectly aligned, forming an undistorted three-dimensional network with cubic symmetry. The stability of this ideal structure depends on two factors:

c) Tolerance factor Goldschmidt analysis

The ABO_3 perovskite structure exhibits substantial flexibility, allowing for a wide array of applications based on the positions of the **A** and **B** cations. The relationship between the **A−O** and **B−O** bond lengths is fundamental for determining the various properties of these materials. In an ideal cubic crystal structure, the distance between the **B** and **O** ions is equal to $\boldsymbol{a/2}$ (where *a* represents the lattice constant) and the distance between the **A** and **O** ions is $\boldsymbol{a/\sqrt{2}}$. The relationship between the **A** and **B** atoms is given by:

$$\mathbf{R_A + R_O = \sqrt{2}(R_B + R_O)} \qquad (\mathbf{I.1})$$

However, in ABO_3-type perovskite compounds, this ideal equation is not always satisfied. In 1926, Victor Moritz Goldschmidt **[16]** introduced the concept of the tolerance factor, which has become a standard tool for assessing the structural stability of perovskites based on the

interatomic distances $\mathbf{R_A}$ and $\mathbf{R_O}$. The tolerance factor **(*t*)** is calculated by the following expression:

$$\mathbf{t} = \frac{\mathbf{R_A} + \mathbf{R_O}}{\sqrt{2}(\mathbf{R_B} + \mathbf{R_O})} \qquad (\mathbf{I.2})$$

Here, $\mathbf{R_A}$, $\mathbf{R_B}$ denote the ionic radii of the **A** and **B** cations, respectively, while R_O corresponds to the ionic radius of the oxygen anion.

The values of the ionic radii used for calculating ***t*** were empirically determined and are listed in the Shannon and Prewitt table **[17].**

Depending on the value of ***t***, structural deviations from the ideal cubic structure are observed. When the value of ***t*** approaches 1, the ideal cubic perovskite structure is retained. As long as ***t*** remains between 0.75 and 1.06, the material preserves a perovskite-like structure **[18]**. The ratio of the volume of the **A**-site cation polyhedron ($\mathbf{V_A}$) to that of the **B**-site cation ($\mathbf{V_B}$) is exactly 5. This ratio $\mathbf{V_A/V_B}$ is a useful parameter that characterizes the degree of distortion of the perovskite structure. The smaller this ratio, the greater the structural distortion.

Table I.1 presents the various crystal structures that emerge based on the value of the Goldschmidt tolerance factor.

Table I.1 Evolution of the crystal structure as a function of the tolerance factor value	
t < 0.75	Ilmenite
0.75 < t < 0.90	Orthorhombic Distortion
0.90 < t < 0.95	Orthorhombic Distortion
0.95 < t < 1.06	Cubic
t > 1.06	Hexagonal

d) Ionicity of the bonds

One of the critical parameters for determining the stability of a material is the ionicity of the anion-cation bond. The average ionic character of the ABO_3 perovskite structure can be quantified by examining the differences in electronegativity, as defined by Pauling's scale **[19]**.

$$\Delta\chi_{AB} = \chi_B - \chi_A \qquad (\mathbf{I.3})$$

$$\Delta\chi_{A0} = \chi_O - \chi_A \qquad (\mathbf{I.4})$$

Where $\Delta\chi_{AB}$ and $\Delta\chi_{AO}$ denote the electronegativity differences between cations **A** and **B**, and between cation A and the oxygen anions, respectively. The stability of the perovskite structure is enhanced when the involved bonds exhibit a significant ionic character. Lead-based perovskites, which exhibit a more covalent character, are generally less stable than more ionic perovskites such as $BaTiO_3$ **[20]**.

1.4 Crystallographic structure of Perovskites

Perovskites are a class of materials with a characteristic crystal structure that is of great interest due to their electrical, magnetic and optical properties. These materials typically crystallize in a cubic structure, but can also undergo distortions, leading to variations such as rhombohedral, orthorhombic or other lower symmetry structures as illustrated in (**Figure I.4**) **[21]**.

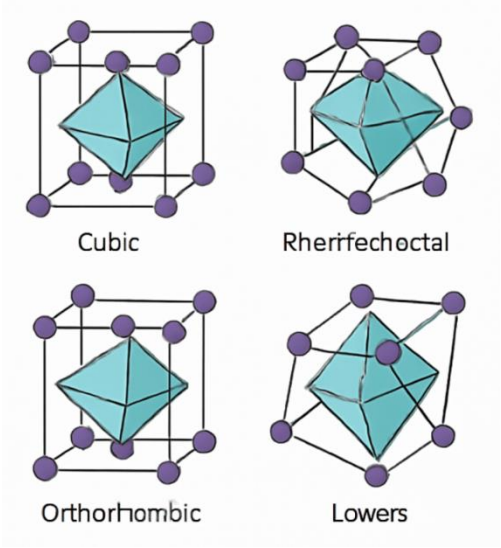

Figure I.4 Crystallographic structures of Perovskites: cubic, rhombohedral, orthorhombic, and lower symmetry variants

1.4.1 Ideal Cubic Perovskite Structure

The ideal perovskite is a simple cubic structure and belongs to the space group **Pm-3m**. It has a motif of one molecule per unit cell (**Z = 1**). The crystallographic motif of the perovskite ABX_3 contains five atoms (see **Figure I.2**). The larger **A** cations are located at the corners of the cube, with a coordination number of 12. These A cations are typically alkali ions (e.g., K^+, Na^+), alkaline-earth ions (e.g., Sr^{2+}, Ca^{2+}), or rare-earth ions (e.g., La^{3+}). The smaller **B** cations, which are six-coordinated, are usually transition metals (e.g., Mn^{3+}, Mn^{4+}, Ti^{4+}) and occupy the center of the cube. Oxygen anions, which are also six-coordinated, occupy the center of each face of the cube **[22]**.

In the case of manganite, such as $LaMnO_3$, the manganese forms octahedral MnO_6 units, as shown in **Figure I.2 [23]**. The ideal cubic perovskite structure is characterized by an electroneutrality condition, where the sum of the charges of the **A** and **B** cations equals the total charge of the oxygen anions. Depending on the charge of the cations, the material can adopt different oxidation states, leading to variations such as monovalent ($A^{+}B^{5+}$), divalent ($A^{2+}B^{4+}$), or trivalent ($A^{3+}B^{3+}$) oxidation states **[24]**.

As an illustration, the parent compound $LaMnO_3$ behaves as an insulating antiferromagnet due to super exchange coupling between Mn^{3+} ions **[25]**. However, by modifying the stoichiometry of oxygen or substituting La^{3+} with a divalent element (such as Sr^{2+}), Mn^{4+} ions appear and the material becomes metallic with a ferromagnetic double-exchange mechanism **[26]**.

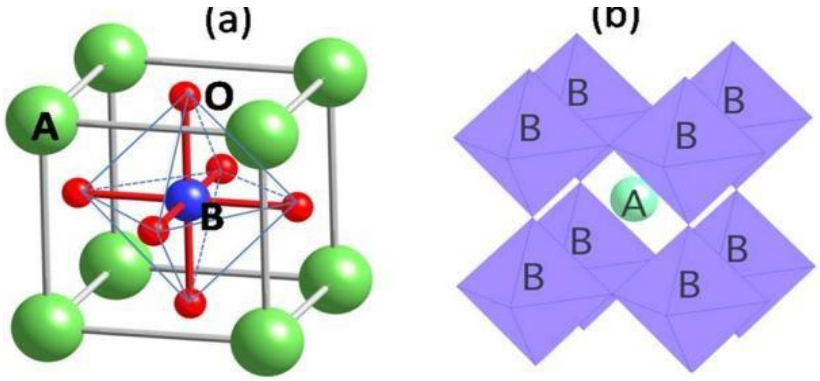

Figure 1.5 Structure model of an ideal perovskite

1.4.2 Distorted Perovskite Structures

While the ideal cubic structure is the most basic form, many perovskite compounds do not crystallize in this structure. Rather, they undergo distortions that lead to rhombohedral, orthorhombic, or other lower symmetry structures **[27]** These distortions often arise from factors such as changes in the ionic radii of the **A** and **B** cations or from electronic ordering phenomena like the Jahn-Teller effect **[28]**. The presence of different anions, such as chlorine (**Cl**) or iodine (**I**), can also influence the crystal structure, creating double perovskites or other variants with slightly different characteristics **[29]**. For example, the **A** and **B** cations may still retain their basic positions, but halide anions replace oxygen, leading to distinct structural modifications. Other examples of such perovskites include compounds like Sr_2FeMoO_6 **[30]**, which display similar distortion patterns depending on their specific ionic configuration.

It can be concluded that the crystallographic structure of perovskites is highly dependent on the ionic sizes of the constituent elements and the specific distortions that occur due to factors like

electronic ordering and ionic radii. These distortions can have significant impacts on the material's physical properties, making perovskites a versatile and important class of materials in both fundamental and applied research **[31]**.

I.5 General Properties of perovskites

Perovskites are a diverse family of crystalline materials, characterized by their structural flexibility, chemical richness and ability to exhibit multiple properties within a single phase. They are defined not just by their chemical formula, but by their intrinsic nature as adaptive, multifunctional solids capable of exhibiting complex electronic, magnetic, optical, and catalytic behaviors. This nature arises from their ordered three-dimensional architecture, which accommodates a wide variety of atomic species without compromising structural coherence. Classical oxide perovskites Such as, $SrTiO_3$ demonstrate both quantum paraelectricity and high electron mobility, making it useful in power electronics and as a substrate for thin-film deposition **[32-33]**. Perovskites can also be ferroelectric. $BaTiO_3$ was the first such material to be discovered and remains widely used in capacitors and ferroelectric memory devices due to its reversible electric polarization under an external field. Regarding piezoelectricity, $Pb(Zr_{1-x}Ti_x)O_3$(PZT) is considered the benchmark material, as it efficiently converts mechanical stress into electrical signals, which is crucial in ultrasound transducers and actuators **[34-35]**. Optically, many perovskites, especially halide perovskites, exhibit strong light absorption and tunable band gaps. $CH_3NH_3PbI_3$, for example, absorbs visible light efficiently and has an ideal bandgap (~1.55 eV) for solar energy conversion, enabling solar cell efficiencies exceeding 25%, which rivals traditional silicon technologies **[36-37]**. The all-inorganic variant $CsPbBr_3$ is notable for its stability and intense photoluminescence, making it suitable for LEDs and low-threshold lasers **[38]**. On the magnetic side, perovskites such as $La_{1-X}Ca_XMnO_3$ exhibit colossal magnetoresistance, characterized by a dramatic change in electrical resistance under the influence of a magnetic field, making them particularly attractive for spintronics and magnetic sensors **[39-40]**. Others, like $YFeO_3$ are antiferromagnetic, relevant in nonlinear optics and spin-wave devices **[41]**. In heterogeneous catalysis, perovskites are widely studied for their redox activity and oxygen mobility, for example, $LaCoO_3$ and $La_{1-X}Sr_XMnO_3$ serve as efficient electrodes in solid oxide fuel cells, while $SrFeO_{3-\delta}$ is known for its high oxygen ion conductivity, useful in gas separation membranes and chemical looping **[42-43]**. Thermally, perovskites like $BaZrO_3$ and $LaAlO_3$ are highly stable at >1000°C, used as substrates for the epitaxial growth of high-temperature superconductors and oxide films **[44-45]**. Despite their high optoelectronic efficiency, hybrid organic-inorganic perovskites, such as $CH_3NH_3PbI_3$, are

sensitive to moisture, heat and UV light, posing challenges for long-term stability in devices. Significant research is underway to enhance their robustness via encapsulation and chemical modifications **[46-47]**. Fundamentally, the nature of perovskites resides in their ability to host multiple physical phenomena in a unified crystal structure, making them essential materials for advanced technologies in energy, electronics, photonics and catalysis.

I.6 Methods of synthesis of compounds

Preparing of perovskite compounds, whether in a simple or double, is one of the most important steps in determining their purity, crystal quality, grain size and functional properties such as magnetism, conductivity and optical behavior. A wide range of synthesis methods has been developed, each suited to specific types of perovskites and applications. One of the most traditional and widely used techniques is solid-state synthesis, which involves high-temperature reactions between solid precursors. For example, early studies on double perovskites like Sr_2FeMoO_6 and Ba_2FeMoO_6 used this method by mixing oxide or carbonate powders such as Fe_2O_3, MoO_3 and $SrCO_3$ often with metallic Mo, followed by repeated calcination steps between 900°C and 1200°C. The challenge with this approach is incomplete reaction or formation of impurity phases, such as $SrMoO_4$ or $BaMoO_4$, especially when the synthesis is performed at lower temperatures or without a reducing atmosphere. Researchers have developed purification techniques, such as magnetic separation in CCl_4, to remove diamagnetic impurities **[48]**. To improve phase purity, especially for oxygen-sensitive perovskites, some studies used sealed silica ampoules under vacuum or controlled atmospheres. In these cases, adding metallic iron Inside the ampoule allowed for precise control of the oxygen partial pressure, which helped obtain pure phases but could still lead to oxygen vacancies if the reduction was too strong **[49]**. More recent approaches avoid ampoule-based synthesis and instead use gas mixtures, such as H_2/CO_2 or H_2/Ar, to control the atmosphere during high-temperature treatments **[50]**. These methods enable fine-tuning of oxygen stoichiometry, which is crucial for the electronic and magnetic properties of double perovskites. For example, Sr_2FeMoO_6 synthesized under 1% H_2 in Ar at 1200°C shows improved magnetic ordering due to better Fe/Mo cation ordering and reduced impurity phases **[51]** To synthesize nanostructured perovskites or to improve homogeneity, wet-chemical routes such as sol-gel methods are employed. Here, metal salts like $Fe(NO_3)_3$, $Sr(NO_3)_2$ and $(NH_4)_6Mo_7O_{24}$ are dissolved in nitric acid, forming a gel upon solvent evaporation **[52]**. Subsequent calcination at 700–1000°C under reducing conditions yields nanoparticles with grain sizes as small as 30–50 nm, depending on temperature **[53-54]**. Similarly, the citrate precursor method uses citric acid and metal salts to form a resin, which is

decomposed at moderate temperatures, followed by reduction at higher temperatures to form highly reactive precursor powders that easily transform into the perovskite phase **[55]**. Another increasingly popular method is combustion synthesis, which involves exothermic reactions between metal nitrates and organic fuels (e.g., hydrazine derivatives or glycine) **[56]**. This method is fast, producing fine powders (100–200 nm) with high surface area and short reaction times **[57]**. Combustion synthesis is especially useful for perovskites used in catalysis or as magnetic materials, where particle size and surface reactivity are important **[58]**. In all these methods, the choice of temperature, atmosphere, and precursor type is critical for achieving phase purity and desired functional properties. Modern synthesis also focuses on controlling cation ordering (especially in double perovskites), which can be enhanced by atomic-level mixing of precursors, as seen in polyacrylamide gel combustion or advanced sol-gel processes. These techniques have allowed the fabrication of highly ordered and pure perovskites with tailored properties for applications in spintronics, sensors, photovoltaics and fuel cells **[59]**. Several traditional and modern approaches can be distinguished for the synthesis of perovskites, such as solid-state reaction, sol-gel method, and combustion techniques. In the specific case of fluoro-perovskites, different routes are employed, including crystal growth by the Czochralski method and solid-state reactions. Among these, the Czochralski technique **[60]** remains the most widely used, as it enables the growth of large single crystals.

I.6.1 Czochralski crystal growth method

In this method, a single-crystal seed **(Figure I.6)**, or alternatively a platinum rod when a seed is unavailable, is brought into contact with the surface of the molten material in a crucible maintained close to its melting temperature. Capillary action causes the melt to rise a few millimeters and adhere to the seed, forming a triple interface of solid–liquid–vapor.

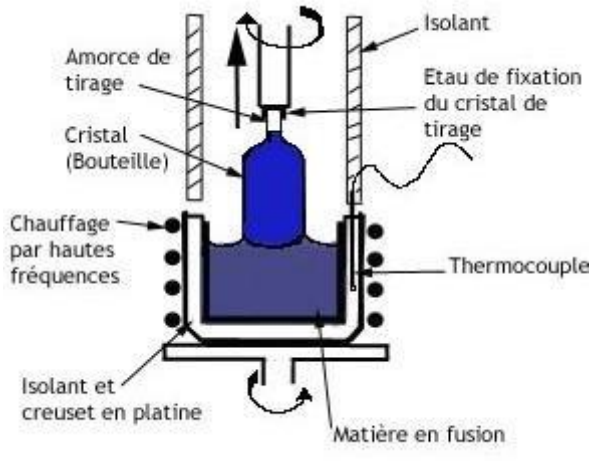

Figure I.6: Schematic diagram of the Czochralski method

While continuously rotating, the seed is slowly pulled upward at a recrystallization rate of about 0.6 to 2.5 mm/h, keeping the triple interface close to the melt surface. Under appropriate conditions, the material withdrawn from the melt develops into a single crystal **[61–62] (Figure I.7)**.

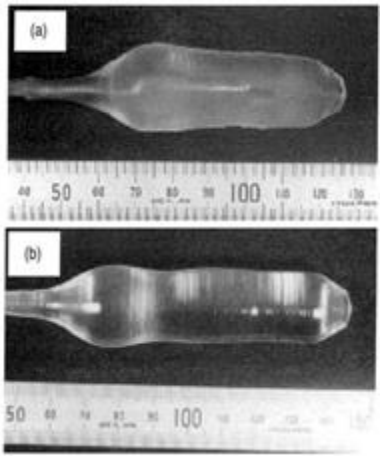

Figure I.7: Single crystals of $KMgF_3$ (a) and $BaLiF_3$ (b) grown by the Czochralski method.

I.6.2 Solid-state reaction method

A compound of the form $ALiF_3$ can be synthesized by a solid-state reaction starting from high-purity powders (99.9%). The stoichiometric starting mixture is prepared from LiF and AF_2 powders. Initially, the constituent elements are pre-dried at 150 °C under a controlled atmosphere (O_2, Ar, etc.). The starting powders are then weighed and thoroughly mixed in an agate mortar to homogenize the reaction mixture. Usually, the reactions are carried out in crucibles made of gold, platinum or alumina (pre-degassed at 600°C for 30 minutes). The heat treatment is performed in furnaces capable of heating under controlled atmosphere (O_2, Ar, N_2) or under vacuum, at high temperatures (>800 °C) to allow the solid-state reaction to proceed. The resulting products appear as crystallites typically about tens of microns in size.

I.7 Applications of Perovskites in modern technologies

a) Solar Cells

Perovskites have become essential in the field of solar energy due to their high light absorption**,** low-cost processing and high efficiency**.** A widely used simple perovskite is $CH_3NH_3PbI_3$ (methylammonium lead iodide). This material has been used in perovskite solar cells since 2009 and today enables devices with over 25% efficiency**,** thanks to its excellent optoelectronic properties and ease of fabrication at low temperatures**.** A more stable simple inorganic perovskite is $CsPbI_3$ **(**cesium lead iodide), which offers better thermal and humidity

stability**.** It is particularly suited for outdoor solar panels and is also used in tandem solar cells in combination with silicon **[63]**. As a lead-free alternative**,** the double perovskite $Cs_2AgBiBr_6$ (cesium silver bismuth bromide) has attracted interest. Although its solar efficiency is lower**,** it is non-toxic and chemically stable**,** making it a promising material for environmentally friendly solar cells **[64]**.

b) LEDs and Photodetectors

Perovskites are also used in light-emitting diodes (LEDs) and photodetectors due to their strong luminescence and ability to efficiently convert light into electricity or vice versa. A well-known simple perovskite used in LEDs is $CsPbBr_3$ (cesium lead bromide), which emits bright green light with high color purity and is used in display technology and lighting. For photodetectors, a widely studied simple perovskite is $CH_3NH_3PbBr_3$ (methylammonium lead bromide), which is sensitive to visible light and is used in cameras, motion detectors, and medical imaging devices **[65]**. As a lead-free option**,** the double perovskite $Cs_2AgBiCl_6$ (cesium silver bismuth chloride) is being developed for blue-emitting LEDs**.** It offers better environmental safety**,** although its efficiency is still being improved **[66]**.

c) Catalysis and Batteries

Oxide perovskites are extensively used in catalysis and energy storage**,** especially due to their stability**,** conductivity**,** and ability to promote chemical reactions. A widely applied simple perovskite in catalysis is $LaMnO_3$ (lanthanum manganite), which is used in fuel cell electrodes and automotive catalytic converters for cleaning exhaust gases. Another important simple perovskite**,** $LaFeO_3$ (lanthanum ferrite), is employed for carbon monoxide oxidation and in air purification systems. It is known for its good catalytic activity and chemical durability. In battery technology, the simple perovskite $Li_{3X}La_{2/3-x}TiO_3$ **(**LLTO**)** is used as a solid electrolyte in solid-state lithium batteries**.** It is valued for its high lithium-ion conductivity and enhanced safety**,** compared to liquid electrolytes **[67]**. A practical example of a double perovskite in catalysis and sensing is Ba_2FeMoO_6 (barium iron molybdate). It has good electrical conductivity and thermal stability, making it suitable for chemical sensors and multi-functional catalytic devices **[68]**.

I.8 Synthesis of Perovskite compounds - Challenges and opportunities

One of the foremost challenges in the development of perovskite-based technologies is ensuring their long-term stability and resistance to degradation. Many perovskites, particularly halide types, are known to degrade when exposed to air, water vapor, light and elevated

temperatures. For example, the **2D** hybrid perovskite $(BA)_2PbI_4$ (where BA = butylammonium) offers improved moisture resistance over **3D** perovskites but still suffers from photochemical degradation under continuous illumination **[69]**. Perovskite films can also experience phase transitions for instance, $CsPbBr_3$, while more thermally stable than some organic-inorganic perovskites, may degrade at high temperatures or under intense light exposure, leading to loss of optical and electronic performance **[70]**. The migration of halide ions (e.g., Br^-) within the crystal lattice under an electric field also contributes to instability, causing performance drift in devices like LEDs and solar cells **[71]**. To address these issues, compositional engineering has been explored, such as incorporating rubidium or potassium ions to stabilize the perovskite lattice **[72]**, or using core shell nanostructures, where the perovskite core is coated with a protective shell, such as SiO_2, to block moisture **[73]**. Additionally, encapsulation techniques using polymer barriers (e.g., polyvinylidene fluoride) and inert gas-filled packaging have successfully extended device life under real-world conditions **[74]**. While significant progress has been achieved, ensuring decades-long operational stability comparable to silicon-based technologies remains an urgent and promising area of research.

In addition to instability, toxicity concerns, particularly regarding heavy metal content, pose a significant obstacle to the mass deployment of perovskite materials. The primary concern is environmental contamination due to lead (Pb) leaching from damaged or discarded devices. To reduce risk, researchers have developed bismuth-based perovskite derivatives, such as $MA_3Bi_2I_9$, which offer a safer alternative, albeit with lower efficiency due to indirect band gaps **[75]**. Another example of a non-toxic perovskite system is $Cs_2AgInCl_6$, a copper-based perovskite, explored for photon detection with promising safety and stability profiles **[76]**. Additionally, antimony chalcogenides like Sb_2S_3 are being researched as non-toxic light absorbers in thin-film solar cells **[77]**. These alternatives, while safer, often exhibit inferior charge transport or lower light absorption than lead-based perovskites. Some strategies to mitigate lead exposure include barrier layers to prevent leakage and the development of recycling protocols with lead-capture resins that recover toxic elements from end-of-life devices **[78]**. The search for high-performance, environmentally benign perovskites remains a significant challenge and opportunity in the field.

Another major challenge is the compatibility of perovskites with other materials and processes required for integration into commercial devices. For example, in perovskite-silicon tandem solar cells, perovskites must be processed at low temperatures to avoid damaging the silicon layer, while maintaining film uniformity and interfacial stability **[79]**. Additionally, materials

like zinc oxide (ZnO) used as electron transport layers may react chemically with perovskites, causing interfacial degradation and performance loss **[80]**. In photodetectors, aligning energy levels between perovskites and transport layers such as PTAA or PEDOT: PSS is critical for efficient charge extraction, but often leads to voltage losses if mismatched **[81]**. In battery systems, perovskite-based solid electrolytes must interface with lithium or sodium metal anodes without inducing dendrite formation or electrochemical breakdown **[82]**. Solutions include the use of buffer layers like MoO_3 to improve adhesion and prevent degradation, and the adoption of vapor deposition methods to achieve precise control of film growth. Flexible electronics also demand that perovskite layers maintain integrity on plastic substrates like polyethylene terephthalate (PET), which is challenging under mechanical stress. These challenges underline the need for comprehensive interface engineering and scalable fabrication processes, which offer rich opportunities for future technological integration.

Ultimately achieving extremely high efficiency in a variety of applications is one of the greatest opportunities in Perovskite research. The power conversion of Perovskite solar cells is already beyond 25% and when combined with silicon, they go over 30%, which gets close to or even better than old semiconductor technologies. For LEDs, adding certain elements to perovskite nanocrystals like $CsPbBr_3:Ni^{2+}$ makes them shine brighter, lose less energy as heat, and last longer, so they work well for advanced lighting and screen displays **[83]**. In LEDs, doped perovskite nanocrystals such as $CsPbBr_3:Ni^{2+}$ have shown enhanced light emission, reduced non-radiative losses and improved stability, making them suitable for high-performance lighting and display technologies **[84]**. Nevertheless, defects, grain boundaries, and ion migration continue to limit device efficiency and consistency. Strategies such as halide mixing (e.g., Cl^- and I^- blends), defect passivation using small molecules like thiocyanate or formamide and advanced light management layers are being actively explored to push perovskites towards theoretical efficiency limits **[85]**.

I.9 Thesis Motivation

The motivation of this work lies in the fact that most high-performance perovskites contain lead, a toxic element that is harmful to both the environment and human health, thereby limiting their large-scale use and integration into embedded devices. To overcome this limitation, the design and exploration of new lead-free perovskites, which are safer and more sustainable, represent a research direction that is both strategic and innovative. In this perspective, the present thesis proposes a comprehensive comparative study of the structural, electronic, optical, and thermoelectric properties of a series of new lead-free perovskite materials.

The objective is twofold :

1. To understand, through **ab initio** calculations and advanced numerical analyses, the influence of chemical composition and crystallographic parameters on the fundamental properties of these materials.
2. To identify compounds that offer an optimal balance between stability, optoelectronic performance, and thermoelectric efficiency, with a view toward practical applications in embedded systems, where miniaturization, energy efficiency, and durability are essential.

This doctoral work thus aims to make a significant contribution to the search for sustainable alternative materials that combine high performance with environmental friendliness, fully aligning with the current challenges of energy and technological transition.

References

[1] Bowman, H. L. On the structure of Perovskite from the Burgumer Alp, Pfitschthal, Tyrol. *Mineral. mag. j. Mineral. Soc.* **15**, 156–176 (1908).

[2] Souza, E. C. C. D. & Muccillo, R. Properties and applications of perovskite proton conductors. *Mat. Res.* **13**, 385–394 (2010).

[3] *B. Pradhan, Perovskite Optoelectronic Devices*. (Springer International Publishing, Cham, 2024). doi:10.1007/978-3-031-57663-8.

[4] Yang, W. S. *et al.* High-performance photovoltaic perovskite layers fabricated through intramolecular exchange. *Science* **348**, 1234–1237 (2015).

[5] Rao, C. N. R. Perovskite oxides and high-temperature superconductivity. *Ferroelectrics* **102**, 297–308 (1990).

[6] Ishihara, T. *Perovskite Oxide for Solid Oxide Fuel Cells*. (Springer Science & Business Media, 2009).

[7] Kolesnik, S., Dabrowski, B. & Chmaissem, O. Structural and physical properties of SrMn1−xRuxO3 perovskites. *Phys. Rev. B* **78**, 214425 (2008).

[8] Bouchentouf Idriss, Y. Étude du premier principe des propriétés structurales, magnétiques, optoélectroniques, élastiques et thermoélectriques d'un alliage double pérovskites AA'BB 'O6. thèse université de Mascara-Algérie (2024).

[9] Gaulding, E. A. *et al.* Package Development for Reliability Testing of Perovskites. *ACS Energy Lett.* **7**, 2641–2645 (2022).

[10] Gao, P., Konrad, D., Aghazada, S. & Nazeeruddin, M. K. Molecular Engineering of Functional Materials for Energy and Opto-Electronic Applications. *Chimia* **69**, 253 (2015).

[11] Hossain, A., Atique Ullah, A. K. M., Sarathi Guin, P. & Roy, S. An overview of La2NiMnO6 double perovskites: synthesis, structure, properties, and applications. *J Sol-Gel Sci Technol* **93**, 479–494 (2020).

[12] Contents list. *Energy Environ. Sci.* **12**, (2019) 433–441.

[13] De Teresa, J. M., Serrate, D., Blasco, J., Ibarra, M. R. & Morellon, L. Impact of cation size on magnetic properties of (A A ′) 2 FeReO 6 double perovskites. *Phys. Rev. B* **69**, 144401 (2004).

[14] Fu, L., Li, B., Li, S. & Yin, L. Magnetic, Electronic, and Optical Properties of Perovskite Materials. in *Revolution of Perovskite* (eds Arul, N. S. & Nithya, V. D.) 43–59 (Springer Singapore, Singapore, 2020). doi:10.1007/978-981-15-1267-4_2.

[15] Absike, H., Baaalla, N., Lamouri, R., Labrim, H. & Ez-zahraouy, H. Optoelectronic and photovoltaic properties of Cs_2AgBiX_6 (X = Br, Cl, or I) halide double perovskite for solar cells: Insight from DENSITY FUNCTIONAL THEORY. *Intl J of Energy Research* **46**, 11053–11064 (2022).

[16] Goldschmidt, V. M. Die Gesetze der Krystallochemie. *Naturwissenschaften* **14**, 477–485 (1926).

[17] Shannon, R. D. & Prewitt, C. T. Effective ionic radii in oxides and fluorides. *Acta Crystallogr B Struct Sci* **25**, 925–946 (1969).

[18] Roth, R. S. Classification of Perovskite and Other ABO3-Type Compounds[1]. *Journal of Research of the National Bureau of Standards* **58**, 75 (1957).

[19] Pauling, L. *The Nature of the Chemical Bond and the Structure of Molecules and Crystals: An Introduction to Modern Structural Chemistry*. vol. 18 (Cornell university press, 1960).

[20] Acosta, M. *et al.* BaTiO3-based piezoelectrics: Fundamentals, current status, and perspectives. *Applied Physics Reviews* **4**, (2017).

[21] Johnsson, M. & Lemmens, P. Crystallography and chemistry of perovskites. *arXiv preprint cond-mat/0506606* (2005).

[22] Kumar Yadav, A. & Gautam, C. R. A review on crystallisation behaviour of perovskite glass ceramics. *Advances in Applied Ceramics* **113**, 193–207 (2014).

[23] Phan, M.-H. *et al.* Manganese perovskites for room temperature magnetic refrigeration applications. *Journal of Magnetism and Magnetic Materials* **316**, e562–e565 (2007).

[24] Zhang, J., Zhao, Y., Shen, Y., Gao, X. & Ma, J. Strain–induced robust ferromagnetism and exchange bias effect in epitaxial LaMnO3/SrFeO2. 5 bilayer. *Journal of Alloys and Compounds* 181931 (2025).
[25] Zakhvalinskii, V. S., Laiho, R., Lisunov, K. G. & Petrenko, P. A. Preparation and Magnetic Properties of $LaMnO_{3+}$ δ (0≤ δ≤ 0.154). (2006).
[26] Rivero, P., Meunier, V. & Shelton, W. Electronic, structural, and magnetic properties of LaMnO 3 phase transition at high temperature. *Physical review B* **93**, 024111 (2016).
[27] Cai, Y. *et al.* Computational study of halide perovskite-derived A2BX6 inorganic compounds: chemical trends in electronic structure and structural stability. *Chemistry of Materials* **29**, 7740–7749 (2017).
[28] Borges, R. P. *et al.* Magnetic properties of the double perovskites A2FeMoO6; A= Ca, Sr, Ba. *Journal of Physics: Condensed Matter* **11**, L445 (1999).
[29] Liu, X. *et al.* Influence of halide choice on formation of low-dimensional perovskite interlayer in efficient perovskite solar cells. *Energy & Environmental Materials* **5**, 670–682 (2022).
[30] Luz, D. S. *et al.* Spectroscopic, lattice dynamic, first-principles electronic and optical insights, and electrocatalytic performance of the Sr_2FeMoO_6 double perovskite for hydrogen evolution reaction: Luz et al. *Applied Physics A* **131**, 478 (2025).
[31] Chakraborty, R. D. Electrochemical and Electrostatic Control of Optical Properties in Electrolyte-Gated Perovskite Oxides for Active Metasurfaces. (University of Minnesota, 2025).
[32] Shi, X.-L. *et al.* SrTiO3-based thermoelectrics: Progress and challenges. *Nano Energy* **78**, 105195 (2020).
[33] Peña, M. A. & Fierro, J. L. G. Chemical structures and performance of perovskite oxides. *Chemical reviews* **101**, 1981–2018 (2001).
[34] Thomas, R., Dube, D. C., Kamalasanan, M. N. & Chandra, S. Optical and electrical properties of BaTiO3 thin films prepared by chemical solution deposition. *Thin solid films* **346**, 212–225 (1999).
[35] Jaffe, B., Cook, W. R. & Jaffe, H. The piezoelectric effect in ceramics. *Piezoelectric ceramics* 7–21 (1971).
[36] Kojima, A., Teshima, K., Shirai, Y. & Miyasaka, T. Organometal halide perovskites as visible-light sensitizers for photovoltaic cells. *Journal of the american chemical society* **131**, 6050–6051 (2009).
[37] Zhou, F. *et al.* Low-voltage, optoelectronic $CH_3NH_3PbI_{3-x}Cl_x$ memory with integrated sensing and logic operations. *Advanced functional materials* **28**, (2018).
[38] Protesescu, L. *et al.* Nanocrystals of cesium lead halide perovskites (CsPbX3, X= Cl, Br, and I): novel optoelectronic materials showing bright emission with wide color gamut. *Nano letters* **15**, 3692–3696 (2015).
[39] Y. Ignacio III, Processing and Optimization of Bulk $La_{1-x}Ca_xMnO3\pm\delta$, thesis University Undergraduate Research Fellow, Texas (1998).
[40] Dagotto, E., Hotta, T. & Moreo, A. Colossal magnetoresistant materials: the key role of phase separation. *Physics reports* **344**, 1–153 (2001).
[41] Warshi, M. K., Mishra, V., Mishra, V., Kumar, R. & Sagdeo, P. R. Possible origin of ferromagnetism in antiferromagnetic orthorhombic-YFeO3: a first-principles study. *Ceramics International* **44**, 13507–13512 (2018).
[42] Bande, A.-A. Compréhension et modélisation du comportement optique de $LaCoO_3$ dans les capteurs solaires thermiques. (Université de Lorraine, 2023).
[43] Schüler, L. Grenzflächen-und Verspannungseffekte in $La_{1-x}Sr_xMnO_3$-Dünnschichten. (2024).
[44] Ryu, K. H. & Haile, S. M. Chemical stability and proton conductivity of doped BaCeO3–BaZrO3 solid solutions. *Solid State Ionics* **125**, 355–367 (1999).
[45] Christen, H. M. & Eres, G. Recent advances in pulsed-laser deposition of complex oxides. *Journal of Physics: Condensed Matter* **20**, 264005 (2008).
[46] Yin, W.-J., Yang, J.-H., Kang, J., Yan, Y. & Wei, S.-H. Halide perovskite materials for solar cells: a theoretical review. *Journal of Materials Chemistry A* **3**, 8926–8942 (2015).
[47] Leguy, A. M. *et al.* The dynamics of methylammonium ions in hybrid organic–inorganic perovskite solar cells. *Nature communications* **6**, 7124 (2015).

[48] Kobayashi, K.-I., Kimura, T., Sawada, H., Terakura, K. & Tokura, Y. Room-temperature magnetoresistance in an oxide material with an ordered double-perovskite structure. *Nature* **395**, 677–680 (1998).
[49] Shelke, A. R., Ghule, A. V., Lee, Y. P., Lokhande, C. D. & Deshpande, N. G. Investigations on magnetic properties and magnetocaloric effects in electron-doped La1− xZrxMnO3. *Journal of Alloys and Compounds* **692**, 522–528 (2017).
[50] Jehng, J. M., Chen, W.-Z. & Wachs, I. E. Enhancing Low-Temperature Co2 Methanation Via Ni-O-Ce Interactions: A Multi-Spectroscopic Study. *Available at SSRN 5236073*.
[51] Ceravola, R. *et al.* Topochemical nitridation of Sr_2FeMoO_6, Chem.Commun, 55 (2019) 3105.
[52] Alkahder, I. & Shawabkeh, R. A. Thermal Catalysis Effects of Ca $(NO_3)_2$, Mg $(NO_3)_2$, KNO_3, and Fe $(NO_3)_3$ on Olive Mill Solid Waste. *Int. J. of Thermal & Environmental Engineering* **20**, 29–33 (2023).
[53] Rida, K., Peña, M. A., Sastre, E. & Martinez-Arias, A. Effect of calcination temperature on structural properties and catalytic activity in oxidation reactions of LaNiO3 perovskite prepared by Pechini method. *Journal of Rare Earths* **30**, 210–216 (2012).
[54] Li, J. *et al.* Temperature-dependent photoluminescence of inorganic perovskite nanocrystal films. *RSC advances* **6**, 78311–78316 (2016).
[55] Chandradass, J. & Kim, K. H. Nano-LaFeO3 powder preparation by calcining an emulsion precursor. *Materials Chemistry and Physics* **122**, 329–332 (2010).
[56] Thakur, S., Mann, D. S., Sangale, S. S., Kwon, S.-N. & Na, S.-I. Hydrazine derivative-based surface passivator for efficient and stable perovskite solar cells. *Journal of Power Sources* **630**, 236124 (2025).
[57] Zhang, Y. & Park, N.-G. A thin film (< 200 nm) perovskite solar cell with 18% efficiency. *Journal of Materials Chemistry A* **8**, 17420–17428 (2020).
[58] Mukasyan, A. S., Costello, C., Sherlock, K. P., Lafarga, D. & Varma, A. Perovskite membranes by aqueous combustion synthesis: synthesis and properties. *Separation and Purification Technology* **25**, 117–126 (2001).
[59] Huang, K. & Martí, A. A. Recent trends in molecular beacon design and applications. *Analytical and bioanalytical chemistry* **402**, 3091–3102 (2012).
[60] G.A. Sycheva, Influence of the presence of bubbles on the parameters of crystal nucleation in the $26Li_2O \cdot 74SiO_2$ glass. *Glass Phys Chem* **35**, 602–612 (2009).
[61] T.fukuda, K. shimamura, A Yoshikawa and E.G. Villora, Crystal growth of new functional materials for electro-optical applications, OPTO-Electronics Review (2), 109-116 (2001).
[62] A. Duvel, M. Wilkening, R.Uecker, S. Wegner, V. Sepelak and P. Heitjans, Mechanosynthesized nanocrystalline $BaLiF_3$: The impact of grain boundaries and structural disorder on ionic transport, *Phys. Chem. Chem. Phys.*, 12 (2010) 11251-11262.
[63] Dou, L. *et al.* Solution-processed hybrid perovskite photodetectors with high detectivity. *Nature communications* **5**, 5404 (2014).
[64] Slavney, A. H., Hu, T., Lindenberg, A. M. & Karunadasa, H. I. A bismuth-halide double perovskite with long carrier recombination lifetime for photovoltaic applications. *Journal of the American chemical society* **138**, 2138–2141 (2016).
[65] Li, Y. *et al.* Controlling cation segregation in perovskite-based electrodes for high electro-catalytic activity and durability. *Chemical Society Reviews* **46**, 6345–6378 (2017).
[66] Inaguma, Y. *et al.* High ionic conductivity in lithium lanthanum titanate. *Solid State Communications* **86**, 689–693 (1993).
[67] Swarnkar, A. *et al.* Quantum dot–induced phase stabilization of α-CsPbI3 perovskite for high-efficiency photovoltaics. *Science* **354**, 92–95 (2016).
[68] McClure, E. T., Ball, M. R., Windl, W. & Woodward, P. M. Cs2AgBiX6 (X= Br, Cl): new visible light absorbing, lead-free halide perovskite semiconductors. *Chemistry of Materials* **28**, 1348–1354 (2016).
[69] Tsai, H. *et al.* High-efficiency two-dimensional Ruddlesden–Popper perovskite solar cells. *Nature* **536**, 312–316 (2016).
[70] Sutton, R. J. *et al.* Bandgap-tunable cesium lead halide perovskites with high thermal stability for efficient solar cells. *Advanced Energy Materials* **6**, 1502458 (2016).

[71] Jeong, S.-H. *et al.* Characterizing the efficiency of perovskite solar cells and light-emitting diodes. *Joule* **4**, 1206–1235 (2020).
[72] Saliba, M. *et al.* Cesium-containing triple cation perovskite solar cells: improved stability, reproducibility and high efficiency. *Energy & environmental science* **9**, 1989–1997 (2016).
[73] Su, R. *et al.* Wideband and low-loss surface acoustic wave filter based on 15° YX-$LiNbO_3/SiO_2$/Si structure. *IEEE Electron Device Letters* **42**, 438–441 (2021).
[74] Sun, R. *et al.* Over 24% efficient poly (vinylidene fluoride)(PVDF)-coordinated perovskite solar cells with a photovoltage up to 1.22 V. *Advanced Functional Materials* **33**, 2210071 (2023).
[75] Krishnamoorthy, T. *et al.* Lead-free germanium iodide perovskite materials for photovoltaic applications. *Journal of Materials Chemistry A* **3**, 23829–23832 (2015).
[76] Ma, R. *et al.* Four-phonon scattering and wave-like phonon tunneling drive glassy ultralow lattice thermal conductivity in Cs2AgInCl6. *Chinese Physics Letters* (2025).
[77] Kumar, P., Khan, M. Q., Suganthi, S., Ahmad, K. & Oh, T. H. Progress in Sb2Se3 and Sb2S3-Based Solar Cells: SCAPS-1D and Experimental Investigations. *ChemistrySelect* **10**, e202404430 (2025).
[78] Li, W., Mi, T., Tian, T., Yang, M. & Pang, H. Mitigating Lead Toxicity in Halide Perovskite Solar Cells: Strategies for Sustainable Development. *Inorganics* **13**, 123 (2025).
[79] Bush, K. A. *et al.* 23.6%-efficient monolithic perovskite/silicon tandem solar cells with improved stability. *Nature Energy* **2**, 1–7 (2017).
[80] Wang, J. T.-W. *et al.* Efficient perovskite solar cells by metal ion doping. *Energy & Environmental Science* **9**, 2892–2901 (2016).
[81] Ke, Q. B., Wu, J.-R., Lin, C.-C. & Chang, S. H. Understanding the PEDOT: PSS, PTAA and P3CT-X hole-transport-layer-based inverted perovskite solar cells. *Polymers* **14**, 823 (2022).
[82] Beladona, S. U. M. *et al.* A review of perovskite-based lithium-ion battery materials. *Vietnam Journal of Science and Technology* **62**, 813–835 (2024).
[83] Al-Ashouri, A. *et al.* Monolithic perovskite/silicon tandem solar cell with> 29% efficiency by enhanced hole extraction. *Science* **370**, 1300–1309 (2020).
[84] Ajeel, H. A. & Al-Bahrani, M. R. Enhancement of Electric Efficiency and Structural Phase Change of CsPbBr3 Caused by Ni2+ Doping, Iraqi Journal of Applied Physics, 20 (2024).
[85] Abdi-Jalebi, M. *et al.* Maximizing and stabilizing luminescence from halide perovskites with potassium passivation. *Nature* **555**, 497–501 (2018).

CHAPTER II

DENSITY FUNCTIONAL THEORY AND METHODS OF CALCUL

II.1 Introduction

Finding an exact solution to the Schrödinger equation for systems with many electrons is one of the most challenging problems in quantum chemistry and solid-state physics. When a system has *N* electrons, its wave function depends on 3*N* spatial coordinates plus *N* spin coordinates. This complexity grows so quickly that it becomes impossible to handle for systems of realistic size. To get around this, density functional theory (DFT) introduced by Hohenberg, Kohn and Sham in the 1960 takes a completely different path. By contrast, of working with the massive 3*N*-dimensional wave function, DFT focuses on the electron density ρ(r), which depends only on the three spatial coordinates, no matter how many electrons are in the system. This shift in perspective has completely changed computational quantum chemistry, making it possible to model materials with hundreds or even thousands of atoms while keeping a high level of accuracy. Walter Kohn was honored with the 1998 Nobel Prize in Chemistry for his role in developing this pioneering method.

II.2 Schrödinger Equation

In multi-particle systems with strong electron-electron interactions, an exact solution of the Schrödinger equation is only possible through approximations. At the level of ab initio methods, two main approaches stand out : Hartree-Fock (HF) methods and post-Hartree-Fock methods, which are widely used in chemistry.

- The **Density Functional Theory (DFT)** approach, more commonly used by physicists, aims, like other **ab initio** methods, to solve the Schrödinger equation **[1]** without relying on parameters adjusted to experimental results, in order to determine the energy (E) and the wave function (Ψ) of a quantum system.

$$H\Psi = E\Psi \qquad \text{(II. 1)}$$

Where H is the Hamiltonian operator, representing the total energy of the system **[2]**.

$$H = T_e + T_n + V_{ne} + V_{ee} + V_{nn} \qquad \text{(II.2)}$$

$Te = -\frac{1}{2}\sum_i \nabla_i^2$ is the kinetic energy of the electrons,

$T_n = -\frac{1}{2}\sum_A \frac{\nabla_A^2}{M_A}$ is the kinetic energy of the nuclei,

$V_{ne} = -\sum_i \sum_A \frac{Z_A}{R_{Ai}}$ is the potential energy of nucleus–electron attraction,

$V_{ee} = \sum_{i<j} \frac{1}{r_{ij}}$ is the potential energy of electron–electron repulsion, and

$V_{nn} = \sum_{A<B} \frac{Z_A Z_B}{R_{AB}}$ is the potential energy of nucleus–nucleus repulsion.

In the case of an isolated cluster, this Hamiltonian, expressed in atomic units ($\hbar^2 = e^2 = m^2$), is written as follows:

$$H = -\frac{1}{2}\sum_i \nabla_i^2 - \frac{1}{2}\sum_A \frac{\nabla_A^2}{M_A} - \sum_i \sum_A \frac{Z_A}{R_{Ai}} + \sum_{i<j} \frac{1}{r_{ij}} + \sum_{A<B} \frac{Z_A Z_B}{R_{AB}} \qquad \text{(II. 3)}$$

i and ***j*** are indices of the electrons, ***A*** and ***B*** are indices of the nuclei, $\boldsymbol{M_A}$ and $\boldsymbol{Z_A}$ are respectively the mass and the charge of a given nucleus and $\boldsymbol{R_{Ai}}$, $\boldsymbol{r_{ij}}$ and $\boldsymbol{R_{AB}}$ are respectively the nucleus–electron, electron-electron, and nucleus-nucleus distances.

In this chapter, we will discuss the various levels of approximation necessary to solve the Schrödinger equation for a complex system. These approximations, common to both the Hartree-Fock (HF) and density functional theory (DFT) methods, will be presented while neglecting relativistic effects; consequently, the Dirac equation will not be addressed. In first-principles calculations, the primary quantity of interest is the energy of the electronic ground state for a given geometric arrangement. Once the total energy is obtained with sufficient accuracy, other properties can be derived from it. The main difficulty in a first-principles calculation lies in the strong electron-electron interaction. The motion of one electron is correlated with that of all other electrons in the system ; for this reason, the true ground-state wave function cannot be expressed as a simple product of individual electron wave functions. This dependence of the system's wave function on the coordinates of all electrons is so complex that only the hydrogen atom can be treated exactly.

- The adiabatic (Born–Oppenheimer) approximation consists of separating nuclear motion from electronic motion.
- The orbital approximation, which stems from the equivalence between an interacting particle system and an independent particle system.

In the Hartree–Fock method, this is reflected in the decomposition of the multi-electron wave function into a product of single-electron spin–orbitals, whereas in DFT, the electronic density of the system is expressed as the sum of the densities associated with each particle.

II.3 Approximations proposed to solve the Schrödinger equation

a) Born-Oppenheimer approximation

This approximation **[3]** is based on the fact that the mass of any nucleus is significantly greater than that of an electron. For this reason, the motion of the nuclei relative to the electrons can be neglected. Consequently, electrons are considered to move in a potential created by fixed atoms. In this context, the kinetic energy of the nuclei is zero (T_n=0), and the Coulomb energy (V_{nn}) arising from nucleus–nucleus repulsion becomes a constant. At this stage, we move from a problem requiring the solution of the Schrödinger equation for a system of N electrons and M nuclei to solving the Schrödinger equation for a system of N electrons experiencing the potential of the nuclei.

The Hamiltonian then contains only the following electronic and nuclear contributions:

$$H_{él} = -\frac{1}{2}\sum_i \nabla_i^2 - \sum_i \sum_A \frac{Z_A}{R_{Ai}} + \sum_{i<j} \frac{1}{r_{ij}} \qquad \text{(II. 4)}$$

$$H_n = -\frac{1}{2}\sum_A \frac{\nabla_A^2}{M_A} + \sum_{A<B} \frac{Z_A Z_B}{R_{AB}} \qquad \text{(II. 5)}$$

We now need to solve the Schrödinger equation for $\boldsymbol{H_{el}}$ in order to determine the electronic energy $\boldsymbol{E_{el}}$ and the wave function $\boldsymbol{\Psi_{el}}$ of the system:

$$H_{el}\Psi = E_{el}\Psi \qquad \text{(II. 6)}$$

Despite these simplifications, solving this equation remains extremely challenging because, for a system of N electrons, it depends on 3*N* spatial coordinates. This is why it is often coupled with the Hartree approximation.

b) Hartree Fock approximation

In 1927, Hartree proposed a method to calculate approximate multi-electron wave functions by expressing them as products of single-electron wave functions **[4]**. Each electron is associated with an orbital, and the total wave function is written as a product of single-particle wave functions, which are orthogonal to one another.

$$\boldsymbol{\psi} = \boldsymbol{\psi_1(r_1).\psi_2(r_2).\psi_3(r_3)\ldots.\psi_N(r_N)} \qquad \text{(II. 7)}$$

In 1930, Fock demonstrated that Hartree's method does not respect the anti-symmetry principle of the wave function [5]. Indeed, according to Pauli's exclusion principle, two electrons cannot simultaneously occupy the same quantum state.

The Hartree-Fock method [6] provides an approximate solution to the Schrödinger equation for a quantum system with n electrons and **N** nuclei, in which the poly-electronic wave function $\boldsymbol{\psi_{HF}}$ is written as a Slater determinant composed of single-electron spin-orbitals that respect the anti-symmetry of the wave function.

$$\Psi(x_1, x_2, x_3, \ldots, x_N) = \frac{1}{\sqrt{N!}} \begin{vmatrix} \psi_1(x_1) & . & . & \psi_N(x_1) \\ . & . & . & . \\ . & . & . & . \\ \psi_1(x_N) & . & . & \psi_N(x_N) \end{vmatrix} \quad \text{(II. 8)}$$

Or

$$\psi_i(x) = \phi_i(r_i)\alpha_i(\zeta_i) \quad \text{(II. 9)}$$

With $\boldsymbol{\zeta_i}$ as the spin variable and the spin $\left(\pm\frac{1}{2}\right)$ functions are orthonormal.

$$\int \alpha^* (\zeta_i)\alpha(\zeta_j)d\tau = \delta(\zeta_i, \zeta_j) \quad \text{(II. 10)}$$

II.4 Density Functional Theory (DFT)

While Hartree–Fock methods express the energy of a system as a functional of its wave function **(Ψ)**, density functional theory (DFT) methods [7] treat the energy as a functional of the system's electronic density **(ρ)**. One of the main advantages of DFT is that it solves the Schrödinger equation using only the observable **ρ**, defined in physical space $\mathbf{R^3}$, rather than in the **3N**-dimensional configuration space, where the Hartree–Fock wave function is defined. However, this benefit of avoiding the many-body problem disappears when an explicit analytical expression for the energy as a functional of the density is required. Before exploring the basics of density functional theory, we should first define its core concept: the electronic density **(ρ)**.

a) Electronic density

In identifying the various contributions to the Hamiltonian, we define electrons as indivisible and indistinguishable particles. Indeed, an electron cannot be localized as an individual particle; however, its probability of presence within a volume element can be estimated, which corresponds to the electronic density **(ρ)**. Electrons must therefore be

considered collectively as an electronic cloud, and the electronic density allows us to determine the regions of space where electrons are most likely to be found. These electrons are primarily localized near the nuclei. The electronic density **ρ(r)** is a positive function that depends solely on the three spatial coordinates **(x, y, z)**. This quantity vanishes at infinity and, when integrated over all space, equals **N** **[8]**.

b) Hohenberg-Kohn theorem

In contrast to the method developed by Hartree-Fock, in which the energy of the system is a functional of the wave function $\boldsymbol{\Psi}(\vec{\boldsymbol{r}})$, the DFT method based on the two theorems of Hohenberg and Kohn expresses the energy as a functional of the electronic density $\boldsymbol{\rho}(\vec{\boldsymbol{r}})$. This approach significantly simplifies the solution of the Schrödinger equation. Indeed, the many-electron problem is replaced by $\boldsymbol{\rho}(\vec{\boldsymbol{r}})$, which depends only on the spatial coordinates. The fundamental principle of DFT is based on the reformulation of an **N**-body quantum problem into a single-particle problem, with the electronic density as the main variable. Work on density functional theory began in 1964 with physicists Hohenberg and Kohn, who formulated two essential theorems. The two theorems, also referred to as postulates, are presented as follows :

➢ First postulate of the Hohenberg-Kohn theorem

The ground-state energy of a system of interacting electrons in the presence of an external potential $\mathbf{V_{ext}}$ is determined by the ground-state electronic density $\boldsymbol{\rho}(\vec{\boldsymbol{r}})$. Density functional theory establishes a one-to-one correspondence between the external potential and the electronic density. Since the electronic density determines the total number of electrons, it also uniquely specifies the wave function and, consequently, the electronic properties of the system. Therefore, for a given system, the energy can be expressed as follows :

$$E[\rho(\vec{r})] = F_{HK}[\rho(\vec{r})] + \int \rho(\vec{r}) V_{ext}(\vec{r}) d^3\vec{r} \qquad \text{(II. 11)}$$

With:

$\boldsymbol{V_{ext}}(\vec{\boldsymbol{r}})$ represents the external potential influencing the particles of the system. As for $\boldsymbol{F_{HK}}[\boldsymbol{\rho}(\vec{\boldsymbol{r}})]$, it is the Hohenberg-Kohn functional, expressed by:

$$F_{HK}[\rho(\vec{r})] = T_e[\rho(\vec{r})] + V_e - E[\rho(\vec{r})] \qquad \text{(II. 12)}$$

➢ **Second postulate of the Hohenberg-Kohn theorem**

The total functional energy **E(ρ)** becomes minimal when the electronic density **ρ(r)** matches that of the ground state **ρ₀(r)**. The total energy of the system can therefore be expressed as follows:

$$E(\rho_0) = \min E(\rho) \qquad \text{(II.13)}$$

c) Kohn-Sham equations

In 1965, Kohn and Sham proposed a method in which the wave function $\boldsymbol{\psi_{KS}}$ represents a system of **n** non-interacting electrons moving under an effective potential $\hat{\boldsymbol{v}}_{\boldsymbol{eff}}(\vec{\boldsymbol{r}})$. The Kohn-Sham equations are coupled through the electronic density $\boldsymbol{\rho(r)} = \sum_{\boldsymbol{i}} \boldsymbol{\psi_i(r)}^{*}\boldsymbol{\psi_i(r)}$, with this coupling accounted for via an iterative, self-consistent procedure. The orbitals can be expanded using different basis sets ; once a basis is chosen, the orbitals are employed to compute an improved density **(ρ)** through the self-consistent cycle. Kohn and Sham demonstrated that the true electronic density corresponds to the self-consistent solution of this set of one-particle Schrödinger-like equations, now known as the Kohn-Sham equations.

$$\left\{-\frac{1}{2}\nabla^2 + V_{KS}(r)\right\}\phi_i(r) = \varepsilon_i\phi_i(r) \qquad \text{(II. 14)}$$

$$\rho(r) = \sum_{occup}|\phi_i(r)|^2 \qquad \text{(II. 15)}$$

$$V_{KS}(r) = V_{ext}(r) + V_H(r) + V_{XC}(r) \qquad \text{(II. 16)}$$

With

$\boldsymbol{V_{XC}(r)}$: The exchange-correlation potential, which is given by

$$V_{XC}(r) = \frac{\partial E_{XC}[\rho(r)]}{\partial\rho(r)} \qquad \text{(II. 17)}$$

And

$$V_H(r) = \int \rho(r)\frac{1}{|r-r'|}dr' \qquad \text{(II. 18)}$$

The total energy is obtained from the solution of the Kohn-Sham equations using the following equation:

$$E(\rho) = \sum_{ioccup}\varepsilon_i - \int\frac{\rho(r)\rho(r')}{|r-r'|}drdr' + E_{XC}(\rho) - \int V_{XC}(r)\rho(r)dr \qquad \text{(II. 19)}$$

II.5 Exchange and correlation treatment

As mentioned earlier, within the framework of the Kohn-Sham equations, density functional theory (DFT) is, in principle, an exact method (apart from the Born-Oppenheimer approximation and the numerical approaches discussed previously). In this sense, the electronic density that minimizes the total energy is exactly the density of the interacting **N**-electron system. However, DFT remains inapplicable in practice because the exchange-correlation potential which also includes the correction to the kinetic energy is unknown. Therefore, it is necessary to approximate this potential. Two main types of approximations exist : the Local Density Approximation (LDA) and the Generalized Gradient Approximation (GGA), along with derived methods based on non-local approaches.

a) Local Density Approximation (LDA)

The Local Density Approximation (LDA) **[9]** is based on the model of a uniform electron gas and represents the simplest approach for expressing the exchange-correlation energy. It is described as:

$$E_{xc}[\rho] = \int \varepsilon_{xc}\big(\rho(r)\big)dr \qquad (\text{II. } 20)$$

$$with \quad \varepsilon_{XC} = \varepsilon_{XC}^{hom\,o}\big(\rho(r)\big)$$

Where $\boldsymbol{\varepsilon_{XC}^{hom(\rho)}}$ is the exchange-correlation energy per electron in a uniform electron gas of density **ρ**. There is also a version of LDA that accounts for electron spin: this is the Local Spin Density Approximation (LSDA) **[10-11]**. The exchange-correlation energy $\boldsymbol{E_{XC}}$ becomes a functional of the two spin densities, spin-up and spin-down, as follows:

$$\varepsilon_{XC}(\rho) = \varepsilon_X(\rho) + \varepsilon_C(\rho) \qquad (\text{II. } 21)$$

$\boldsymbol{\varepsilon_x}$ is the exchange energy, and $\boldsymbol{\varepsilon_C}$ is the correlation energy.

In the Local Density Approximation (LDA), the total exchange-correlation energy $\boldsymbol{Exc[\rho]}$ is written as:

$$E_{xc} = \frac{e^2}{2}\int d^3r\rho(r)\varepsilon_{xc}[\rho(r)] \qquad (\text{II. } 22)$$

The correlation energy, on the other hand, is overestimated, but since it contributes only weakly to the total energy, the error is small. When the electronic density is considered locally uniform, systems where the density changes abruptly cannot be described accurately.

b) Generalized Gradient Approximation (GGA)

The LDA approach was based on the electron gas model and thus assumed a uniform electronic density. However, atomic or molecular systems are often very different from a homogeneous electron gas, and, more generally, all real systems can be considered inhomogeneous, meaning that the electronic density exhibits spatial variation. Methods known as GGA (Generalized Gradient Approximation) **[12-13]**, sometimes also referred to as **n** on-local methods, were developed to account for this variation in density by expressing the exchange and correlation energies as a function of both the density and its gradient (i.e., its first derivative). Generally, the exchange-correlation energy in the GGA approximation is defined as:

$$E_{XC}^{GGA} = \int f\big(\rho(r), \nabla\rho(r)\big)\, dr \qquad \text{(II. 22)}$$

The GGA is implemented through various parametrizations of the exchange-correlation functional **[14]**. It generally provides good results, improving cohesive energies and lattice parameters. However, the improvement over LDA is not always systematic, as GGA can sometimes overcorrect LDA **[15–16]**. Several expressions for the exchange and correlation energies have been proposed. In principle, these methods can be combined in different ways, but in practice, only a few combinations are widely used. Of particular note is the exchange-correlation functional proposed by Perdew and Wang (PW91) **[17]**, which has been employed here. The GGA approximation has proven effective in many cases and is known to yield better results than LDA, especially for magnetic systems. It also provides a more reliable description of systems with large variations in electronic density.

c) Modified Becke-Johnson approximation (mBJ)

The mbJ functional was initially introduced by Becke-Johnson **[18]** and was later refined by Tran and Blaha **[19]**. Known as the modified Becke-Johnson Potential (or the TB potential: Tran-Blaha), this approach quickly showed its superiority when compared to traditional calculation methods like LDA and GGA. The expression for the mBJ potential proposed by Tran and Blaha is given as follows:

$$V_{X,\sigma}^{BJ}(r) = V_{X,\sigma}^{BR}(r) + \frac{1}{\pi}\sqrt{\frac{5}{6}}\sqrt{\rho_\sigma(r)}\,\frac{1}{\rho_\sigma(r)} \qquad \text{(II. 23)}$$

Here, $\boldsymbol{\rho_\sigma(r) = \sum_{i=1}^{N} |\psi_i(r)|^2}$ represents the electron density.

$$t_\sigma(r) = \frac{1}{2}\sum_{i=1}^{N} \nabla\psi_i^*(r) \,.\, \nabla\psi_i \qquad \text{(II. 24)}$$

Denotes the kinetic energy density, while the Becke-Roussel exchange potential, was developed to represent the Coulomb potential generated by the exchange hole **[20]**.

$$V_{X,\sigma}^{BR}(r) = -\frac{1}{b_\sigma(r)}(1 - e^{-x_\sigma(r)} - \frac{1}{2}x_\sigma(r)e^{-x_\sigma(r)} \qquad \text{(II. 25)}$$

The term $\boldsymbol{b_\sigma(r)}$ is calculated using the following expression:

$$b_\sigma(r) = \left[\frac{x_\sigma^3(r)e^{-ix_\sigma(r)}}{8\pi\rho_\sigma(r)}\right]^{1/3} \qquad \text{(II. 26)}$$

The term $\boldsymbol{x_\sigma}$ can be determined through an equation that incorporates $\boldsymbol{\rho_\sigma}$, $\boldsymbol{\nabla_{\rho_\sigma(r)}}$, $\boldsymbol{\nabla^2\rho_{\sigma(r)}}$, and $\boldsymbol{t_\sigma}$, where **σ** refers to the spin notation.

$$x_\sigma = \alpha + \beta\left(\frac{1}{V_{cell}}\int_{cell}\left|\frac{\nabla\rho(r)}{\rho_\sigma(r)}\right| d^3(r)\right)^{1/2} \qquad \text{(II. 27)}$$

Here, **α** and **β** are adjustable parameters with values of -0.012 (dimensionless) and 1.023 $Bohr^{1/2}$, respectively **[21]**, and $\mathbf{V_{cell}}$ represents the volume of the unit cell. The modified BJ potential (as given in equation **II.27**) is thus expressed in an enhanced form:

$$V_{X,\sigma}^{BJ}(r) = cV_{X,\sigma}^{BR}(r) + (3c - 2)\frac{1}{\pi}\sqrt{\frac{5}{6}}\sqrt{\rho_\sigma(r)}\frac{1}{\rho_\sigma(r)} \qquad \text{(II. 28)}$$

The primary modification in this formulation is the inclusion of the parameter **c**. It is important to note that when **c = 1**, the expression goes back to the original Becke-Johnson form. This parameter was selected to vary linearly with the square root of the mean of $\frac{\boldsymbol{\nabla\rho(r)}}{\boldsymbol{\rho_\sigma(r)}}$.

In general, the band gap increases monotonically with respect to the value of **c**, and with the use of **Eq. II.28**, this approach works reliably for a broad range of materials, from small-band-gap semiconductors to large-band-gap insulators. Notably, even the 22 eV band gap of Ne can be accurately reproduced, as well as the band gaps in transition metal oxides.

d) The LDA, GGA and mBJ Approximations with Spin Polarization

In magnetic systems, the electronic densities depend on spin polarization, meaning that the majority spin density **(ρ↑)** and the minority spin density **(ρ↓)** are not identical. In this context, the

exchange-correlation energies can be described using different approximations, such as the Local Density Approximation (LDA), the Generalized Gradient Approximation (GGA) and the mBJ (modified Becke-Johnson) method, depending on whether or not gradient corrections are introduced **[22]**.

The expression for the exchange-correlation energy in the LDA approach is given by:

$$E_{xc}^{LDA}[\rho\uparrow(r),\rho\downarrow(r)] = \int [\rho\uparrow(r),\rho\downarrow(r)]\varepsilon_{LDA}[\rho\uparrow(r),\rho\downarrow(r)]d^3r \qquad (II.29)$$

In the GGA approximation, gradient corrections are introduced and the exchange-correlation energy becomes a function of not only the electronic densities but also their gradients:

$$[\rho\uparrow(r),\rho\downarrow(r)] = \int [\rho(r),\varepsilon_{GGA}]\left[\rho\uparrow(r),\rho\downarrow(r),\nabla_\rho\uparrow(r),\nabla_\rho\downarrow(r)\right]d^3r \qquad (II.30)$$

The mBJ method is used to improve the description of systems with strong gradients, particularly in the case of semiconductors and insulators. This method introduces a correction to the Becke-Johnson potential function to better model electronic properties in systems where the LDA and GGA approximations may fail, especially for threshold energies and band gaps. Thus, these approximations allow for a more precise modeling of effects related to spin polarization and exchange-correlation interactions in magnetic materials.

e) The LDA, GGA and mBJ Approximations with Hubbard Correction

The LDA and GGA methods, although effective for many systems, often underestimate the gap in semiconductors and insulators. This is particularly problematic for systems with ***d***- and ***f***-orbitals, where the intra-site Coulomb repulsion (U, the Hubbard term) becomes significant. To address this issue, the DFT+U method was developed, combining DFT with a Hubbard Hamiltonian to better account for strong Coulomb interactions between localized electrons **[22-23]**. This approach adjusts the exchange-correlation energy by introducing an additional term *U*, as expressed by:

$$\hat{H}_{Hubbard} = \frac{U}{2}\sum_{m,m\prime\sigma}\hat{n}_{m,\sigma}\hat{n}_{m\prime,-\sigma} + \frac{(U-J)}{2}\sum_{m\neq m\prime,\sigma}\hat{n}_{m,\sigma}\hat{n}_{m\prime,\sigma} \qquad (II.31)$$

The total energy in DFT+U becomes **[24-25]**:

$$E_{DFT+U} = E_{DFT} + \frac{(U-J)}{2}\sum_{m\sigma}\left(\hat{n}_{m,\sigma} - \hat{n}_{m\prime,\sigma}^2\right) \qquad (II.32)$$

This approach improves the description of strongly correlated systems, particularly by adjusting the parameters U and J using constrained LSDA calculations or experimental data **[26]**. For systems that demand more accurate a better modeling of strong interactions, the mbJ method is also employed.

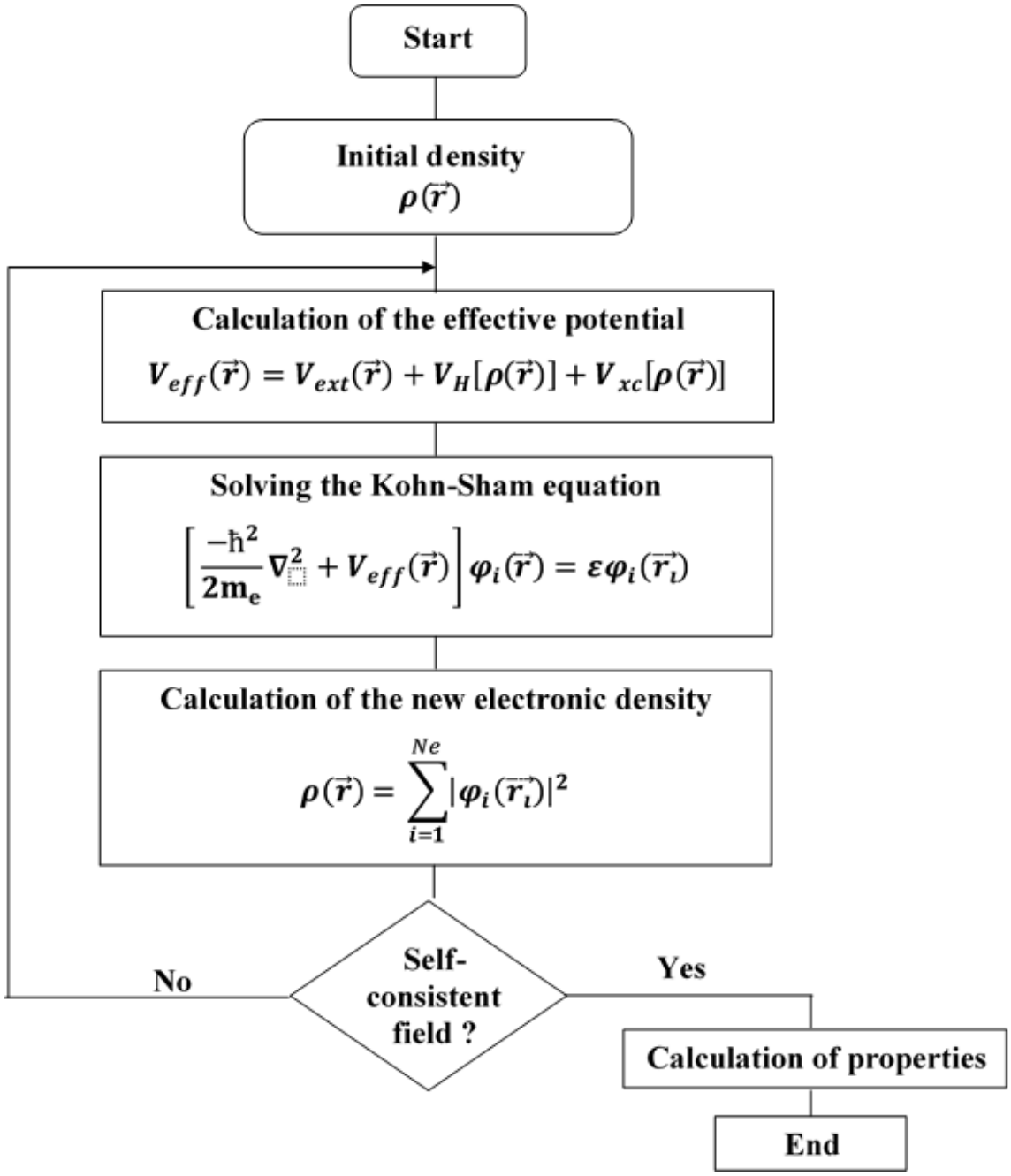

Figure II.1 Diagram of density functional theory (DFT)

II.6 Linearized Augmented Plane Wave method (FP-LAPW)

a) The APW Method

The Augmented Plane Wave (APW) method, first introduced by Slater **[27-28]** and later expanded by Andersen **[29]**, was subsequently refined into its linearized form, known as the LAPW method. In the LAPW formulation, the potential is continuous at the boundary of the "muffin-tin" (MT) sphere and can be expressed as follows:

$$V(r) = \begin{cases} \sum_{lm} V_{lm}(r) Y_{lm}(r) & inside\ the\ sphere \\ \sum V_k e^{ikr} & outside\ the\ sphere \end{cases} \quad (II.33)$$

Back in 1937, Slater **[27]** introduced the APW method by noting that, in the vicinity of an atomic nucleus, the potential and wave functions can be approximated using the Muffin-Tin (MT) model. Specifically, both the potential and wave functions exhibit characteristics similar to those of an isolated atom: they vary rapidly but preserve spherical symmetry within any MT sphere of radius **R**. Moreover, in the interstitial region between atoms, the potential and the wave functions are comparatively smooth. From the above, the wave functions of the electrons in the crystal are then expanded in different basis sets depending on the region: radial solutions of the Schrödinger equation inside the MT sphere and plane waves in the interstitial region (**Figure.II.2**).

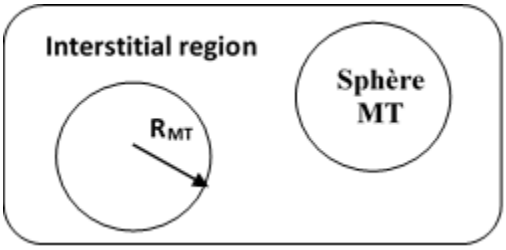

Figure II.2 *Muffin-Tin Potential*

Thus, the wave function **φ(r)** assumes the following form:

$$\varphi(r) = \begin{cases} \frac{1}{\Omega^{1/2}} \sum_G C_G\, e^{i(G+k)r} r > R_\alpha \\ \sum_{lm} A_{lm}\, U_l(r) Y_{lm}(r) r < R_\alpha \end{cases} \quad (II.34)$$

Here, **R** is the radius of the MT sphere, **V** is the volume of the unit cell, C_G and A_{lm} represent the expansion coefficients. The function $U_l(r)$ is a regular solution to the radial part of the Schrödinger equation, and is defined as:

$$\left\{-\frac{d^2}{dr^2}+\frac{l(l+1)}{r^2}+V(r)-E_l\right\}rU_l(r)=0 \qquad \text{(II. 35)}$$

V(r) denotes the muffin-tin potential and E_l is the linearization energy. The radial functions defined in **Eq. (II.35)** are orthogonal to all core eigenstates. However, this orthogonality no longer holds at the sphere boundary as shown by the Schrödinger equation.

$$(E_2-E_1)rU_1U_2=U_2\frac{d^2rU_1}{dr^2}-U_1\frac{d^2rU_2}{dr^2} \qquad \text{(II. 36)}$$

In this context, U_1 and U_2 represent the radial solutions corresponding to the energies E_1 and E_2 respectively. The overlap is obtained using equation (**II.36**) together with integration by parts. Slater justifies the choice of these functions by noting that plane waves are exact solutions of the Schrödinger equation for a constant potential. Whereas, the radial functions are exact solutions for a spherical potential, with E_l being an eigenvalue. This approximation is highly accurate for materials with a face-centered cubic structure, but its accuracy diminishes as the crystal symmetry decreases. To maintain the continuity of the wave function at the MT sphere boundary, the coefficients A_{lm} must be expressed in terms of the C_G coefficients of the plane waves in the interstitial regions. After performing algebraic calculations, the relationship is:

$$A_{lm}=\frac{4\pi i^l}{\Omega^{1/2}U_l(R_\alpha)}\sum C_G j_l(|K+g|R_\alpha)Y^*_{lm}(K+G) \qquad \text{(II.37)}$$

The origin is taken at the center of the sphere and the coefficients A_{lm} are determined from the plane wave coefficients C_G. The energy parameters E_l serve as the variational parameters in the APW method. The functions indexed by *G* become compatible with the radial functions inside the spheres, forming Augmented Plane Waves (APWs). These APWs satisfy the Schrödinger equation within the spheres, but only at the specific energy E_l. As a result, the energy E_l must correspond to the energy of the ***G*** indexed band. Therefore, the energy bands for a given k-point cannot be obtained through by simple diagonalization; instead, the secular determinant must be treated as a function of energy. In its conventional form, the APW method, faces difficulties related to the function $U_l(R_\alpha)$, which appears in the denominator of equation (**II.37**). Specifically, depending on the value of the parameter E_l, $U_\alpha(R_\alpha)$ may approach zero at the MT sphere surface, causing a separation between the radial functions and the plane wave functions. To address this issue, several modifications to the APW method have been proposed, particularly those by Koelling **[30]** and

Andersen [31]. These improvements involve representing the wave function **φ(r)** inside the spheres as a linear combination of the radial functions $\mathbf{U_l(r)}$ and their energy derivatives, $\mathbf{U_l(r)}$, which ultimately lead to the development of the Full Potential-Linearized Augmented Plane Wave (FP-LAPW) method.

b) Concept of the FP-LAPW method

In the FP-LAPW method, the basis functions within the MT spheres are expressed as linear combinations of the radial functions $\boldsymbol{U_l(r)Y_{lm}(r)}$ and their energy derivatives $\dot{\boldsymbol{U}}_{\boldsymbol{l}}\boldsymbol{Y_{lm}(r)}$. The functions $\boldsymbol{U_l}$ are defined in the same way as in the APW method, while the function $\dot{\boldsymbol{U}}_{\boldsymbol{l}}\boldsymbol{(r)Y_{lm}(r)}$ must satisfy the following equation:

$$\left\{-\frac{d^2}{dr^2}+\frac{l(l+1)}{r^2}+V(r)-E_l\right\}r\dot{U}_l(r)=rU_l(r) \qquad \text{(II. 38)}$$

In the non-relativistic case, these radial functions ensure continuity with the plane waves outside the MT sphere at its surface. Once augmented in this way, the wave functions constitute the basis functions (LAPWs) of the FP-LAPW method.

$$\varphi(r)=\begin{cases}\dfrac{1}{\Omega^{1/2}}\displaystyle\sum_G C_G e^{i(G+K)r} & r>R_\alpha \\ \displaystyle\sum_{lm}\left[A_{lm}U_l(r)+B_{lm}\dot{U}_l(r)\right]Y_{lm}(r) & r<R_\alpha\end{cases} \qquad \text{(II. 39)}$$

Where the coefficients $\boldsymbol{B_{lm}}$ correspond to the function $\dot{\boldsymbol{U}}_{\boldsymbol{l}}$ and are of the same nature as the coefficients $\boldsymbol{A_{lm}}$. The LAPW functions are plane waves only in the interstitial regions, similar to the APW method. Inside the spheres, the LAPW functions are better suited than the APW functions. Indeed, if $\boldsymbol{E_l}$ deviates slightly from the band energy **E**, a linear combination will better reproduce the radial function than the APW functions. Consequently, the function $\boldsymbol{U_l}$ can be expanded in terms of its derivative $\dot{\boldsymbol{U}}_{\boldsymbol{l}}$ with respect to the energy $\boldsymbol{E_l}$.

$$U_l(E,r)=U_l(E_l,r)+(E-E_l)\dot{U}_l(E,r)+0((E-E_l)^2) \qquad \text{(II. 40)}$$

Where $\boldsymbol{0((E-E_l)^2)}$ represents the quadratic energy error.

The FP-LAPW method ensures the continuity of the wave function at the MT sphere boundary. However, this procedure is slightly less precise compared to the APW method, which reproduces wave functions with very high accuracy. In FP-LAPW, the wave functions incur an error of order $\mathbf{(E-E_l)^2}$, while the band energies have an error of order $\mathbf{(E-E_l)^4}$. Despite this, the LAPW form of

the functions remains highly effective, enabling all valence bands over a large energy range to be obtained using a single $\mathbf{E_l}$. When this is not possible, the energy window can generally be split into two parts, which is a significant simplification compared to the APW method. In general, if $\mathbf{U_l}$ is zero at the surface of the sphere, its derivative $\mathbf{U_{l'}}$ will be non-zero. Therefore, the issue of continuity at the MT sphere surface does not arise in the FP-LAPW method. Takeda and Kubler **[32]** proposed a generalization of the LAPW method in which N radial functions and their (N−1) derivatives are used. Each radial function has its own parameter $\mathbf{E_{li}}$, ensuring that errors related to linearization are avoided. The standard FP-LAPW method is recovered for N=2 and $\mathbf{E_{l1}}$ close to $\mathbf{E_{l2}}$, while for N>2N, the errors can be further reduced. Unfortunately, using higher-order derivatives to ensure convergence requires significantly more computational time than the standard FP-LAPW method. Singh modified this approach by adding local orbitals to the basis without increasing the cutoff energy of the plane waves.

II.7 Wien2k code

The Wien2k code is an implementation of the FP-LAPW method. It was developed by Blaha and his collaborators **[33]**. Its applications are numerous, including calculations of the electric field gradient **[34–35]**, studies of high-temperature superconducting systems, minerals **[36]**, transition metal surfaces, and non-ferromagnetic oxides. The Wien2k code consists of several independent programs that are interconnected through C-shell scripts. The calculations are performed in three main steps. The role of the different programs is illustrated in **Figure II.3**.

a) **Initialization**: To determine the properties of a given material, the starting data must be generated, which is found in the file case.struct. This file contains the lattice parameters, the crystal structure, the muffin-tin radii, symmetry operations, etc. This step is performed to prepare the SCF cycle. These elements are generated by a series of small programs:

NN: Provides the distances between nearest neighbors and helps determine the muffin-tin sphere radius.

LSTART: Generates the atomic densities and determines how the different orbitals are treated in the band structure calculation (i.e., core states and valence states with or without local orbitals, etc.).

SYMMETRY: Generates spatial symmetry operations, identifies atomic site point groups, constructs LM expansions for lattice harmonics, and determines local rotation matrices.

KGEN: Generates a k-mesh in the Brillouin zone**.**

DSTART: Generates a starting density for the SCF cycle by superimposing the atomic densities generated in LSTART.

b) SCF Calculation: The SCF cycle includes the following steps:

- **LAPW0:** Generates the potential from the density.
- **LAPW1:** Calculates the valence bands (eigenvalues and eigenvectors).
- **LAPW2:** Calculates the valence densities from the eigenvectors.
- **LCORE:** Calculates the core states and densities.
- **MIXER:** Mixes the valence and core densities to produce the new density.

c) Property Calculation: The calculation of physical properties is performed using the following programs:

- **OPTIMISE:** Determines the total energy as a function of volume, which is used to calculate the lattice parameter, compressibility modulus, and its derivative.
- **TETRA:** Calculates the total and partial density of states.
- **SPAGHETTI:** Calculates the band structure using the eigenvalues generated by LAPW1.
- **OPTIC:** Calculates the optical properties.
- **XSPEC:** Calculates the absorption and emission X-ray spectra structures.

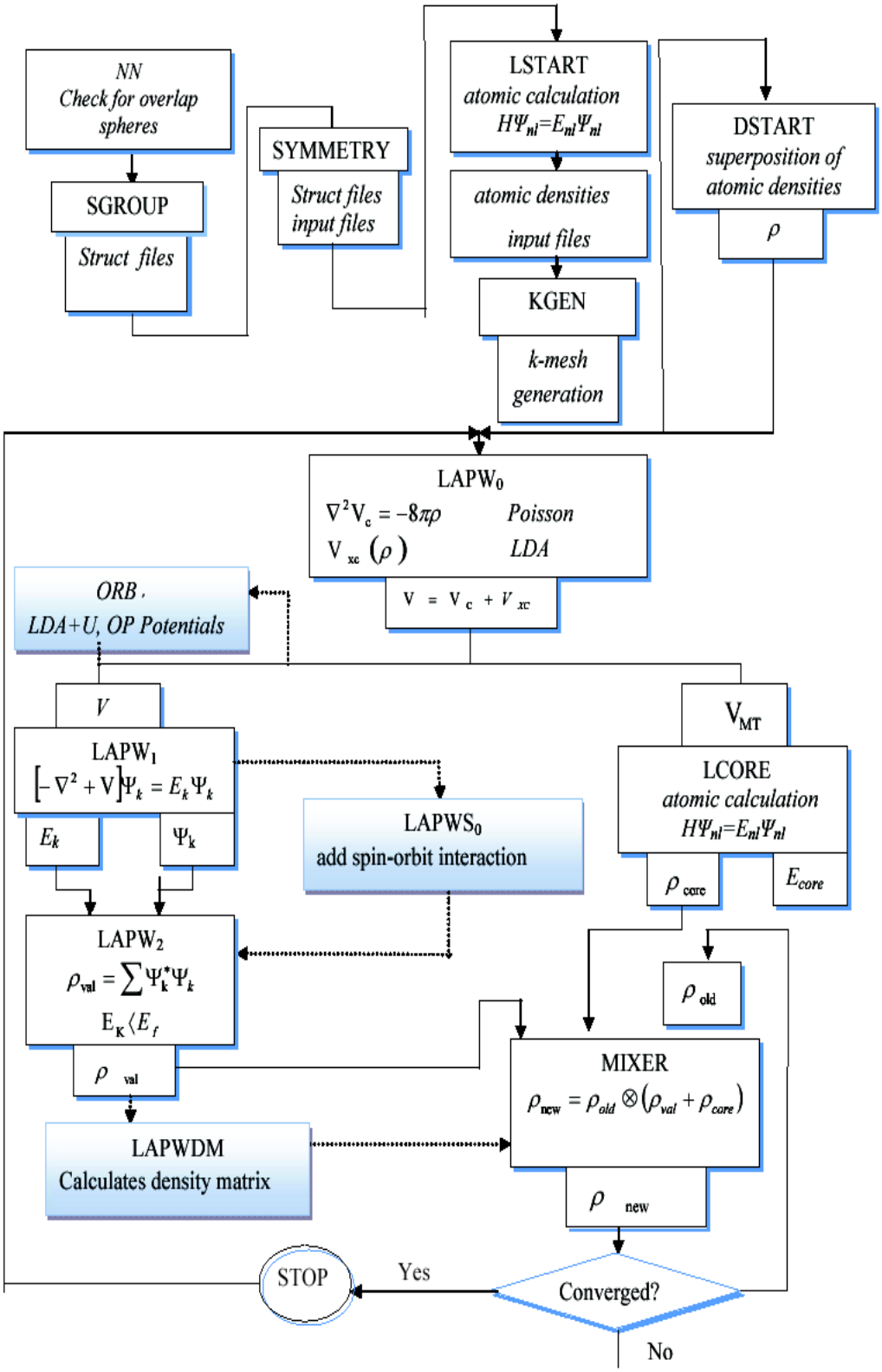

Figure II.3 Wien2k Code **[18]**

References

[1] Lovenberg, W. *Iron-Sulfur Proteins: Biological Properties*. vol. 1 (Academic Press, 1973).

[2] Scheller, F. *et al.* Studies on electron transfer between mercury electrode and hemoprotein. *Biochim Biophys Acta* **412**, 157–167 (1975).

[3] Wrightstone, R. N., Smith, L. L., Wilson, J. B., Vella, F. & Huisman, T. H. Some physicochemical properties of hemoglobin-manitoba (alpha2 102Ser replaced by Arg (G9) beta2). *Biochim Biophys Acta* **412**, 283–287 (1975).

[4] Hartree, D. R. Mathematical Proceedings of the Cambridge Philosophical Society. *The Wave Mechanics of an Atom with a Non-Coulomb Central Field. Part II. Some Results and Discussion* **24**, 111 (1928).

[5] Fock, V. Näherungsmethode zur Lösung des quantenmechanischen Mehrkörperproblems. *Zeitschrift für Physik* **61**, 126–148 (1930).

[6] Rivail, J.-L. *Eléments de Chimie Quantique à l'usage Des Chimistes*. (EDP Sciences, 1999).

[7] Hohenberg, P. & Kohn, W. Inhomogeneous electron gas. *Physical review* **136**, B864 (1964).

[8] Parr, R. G. Density functional theory of atoms and molecules. in *Horizons of Quantum Chemistry: Proceedings of the Third International Congress of Quantum Chemistry Held at Kyoto, Japan, October 29-November 3, 1979* 5–15 (Springer, 1989).

[9] Starkloff, T. & Joannopoulos, J. D. Local pseudopotential theory for transition metals. *Physical Review B* **16**, 5212 (1977).

[10] Perdew, J. P. & Yue, W. Accurate and simple density functional for the electronic exchange energy: Generalized gradient approximation. *Physical review B* **33**, 8800 (1986).

[11] Perdew, J. P. & Zunger, A. Self-interaction correction to density-functional approximations for many-electron systems. *Physical review B* **23**, 5048 (1981).

[12] Skriver, H. L. Calculated structural phase transitions in the alkaline earth metals. *Physical Review Letters* **49**, 1768 (1982).

[13] Chadi, D. J. (110) surface atomic structures of covalent and ionic semiconductors. *Physical Review B* **19**, 2074 (1979).

[14] Chadi, D. J. Theoretical study of the atomic structure of silicon (211),(311), and (331) surfaces. *Physical review B* **29**, 785 (1984).

[15] Tomanek, D., Aligia, A. A. & Balseiro, C. A. Calculation of elastic strain and electronic effects on surface segregation. *Physical review B* **32**, 5051 (1985).

[16] Zhong, W., Li, Y. S. & Tomanek, D. Effect of adsorbates on surface phonon modes: H on Pd (001) and Pd (110). *Physical Review B* **44**, 13053 (1991).

[17] Korringa, J. On the calculation of the energy of a Bloch wave in a metal. *Physica* **13**, 392–400 (1947).

[18] Blaha, P., Schwarz, K. & Luitz, J. WIEN97 User's Guide. *Technical University Vienna, Vienna* (1997).

[19] Blaha, P. & Schwarz, K. Electric field gradient in Cu_2O from band structure calculations. *Hyperfine Interactions* **52**, 153–159 (1989).

[20] Dufek, P., Blaha, P. & Schwarz, K. Determination of the nuclear quadrupole moment of 57 Fe. *Physical review letters* **75**, 3545 (1995).

[21] Schwarz, K., Ambrosch-Draxl, C. & Blaha, P. Charge distribution and electric-field gradients in $YBa_2Cu_3O_{7-x}$. *Physical Review B* **42**, 2051 (1990).
[22] Lardjane, S. Etude des propriétés structurales, électroniques et magnétiques du semi-conducteur magnétique dilué: ZnO dopé au cobalt. (These, Université de Technologie de Belfort-Montbeliard; Université Abou Bekr …, 2013).
[23] Anisimov, V. I., Zaanen, J. & Andersen, O. K. Band theory and Mott insulators: Hubbard U instead of Stoner I. *Physical Review B* **44**, 943 (1991).
[24] Dudarev, S. L., Botton, G. A., Savrasov, S. Y., Humphreys, C. J. & Sutton, A. P. Electron-energy-loss spectra and the structural stability of nickel oxide: An LSDA+ U study. *Physical Review B* **57**, 1505 (1998).
[25] Dudarev, S. L., Liechtenstein, A. I., Castell, M. R., Briggs, G. A. D. & Sutton, A. P. Surface states on NiO (100) and the origin of the contrast reversal in atomically resolved scanning tunneling microscope images. *Physical Review B* **56**, 4900 (1997).
[26] Shishkin, M., Marsman, M. & Kresse, G. Accurate quasiparticle spectra from self-consistent GW calculations with vertex corrections. *Physical review letters* **99**, 246403 (2007).
[27] Slater, J. C. Wave functions in a periodic potential. *Physical Review* **51**, 846 (1937).
[28] Herring, C. A new method for calculating wave functions in crystals. *Physical Review* **57**, 1169 (1940).
[29] Andersen, O. K. Linear methods in band theory. *Physical Review B* **12**, 3060 (1975).
[30] Koelling, D. D. & Arbman, G. O. Use of energy derivative of the radial solution in an augmented plane wave method: application to copper. *Journal of Physics F: Metal Physics* **5** (1975) 2041.
[31] Singh, D. Ground-state properties of lanthanum: Treatment of extended-core states. *Physical Review B* **43**, 6388 (1991).
[32] Takeda, T. & Kubler, J. Linear augmented plane wave method for self-consistent calculations. *Journal of Physics F: Metal Physics* **9**, 661 (1979).
[33] Tran, F. WIEN2k: an augmented plane wave plus local orbitals program for calculating crystal properties. (2018).
[34] Harrison, W. A. Effective charges and piezoelectricity. *Physical Review B* **10**, 767 (1974).
[35] Harrison, W. A. & Ciraci, S. Bond-orbital model. II. *Physical Review B* **10**, 1516 (1974).
[36] Penn, D. R. Wave-number-dependent dielectric function of semiconductors. *Physical review* **128**, 2093 (1962).

CHAPTER III

SIMPLE PEROVSKITE $CeBO_3$ (B = Be, Mg)

III.1 Introduction

Perovskite oxides have attracted considerable attention due to their exceptional structural flexibility and diverse physical properties, including electronic, optical, and thermoelectric characteristics. Owing to this versatility, they are promising candidates for applications in energy-related devices, optoelectronics, superconductivity, and catalysis. These materials are also of fundamental interest because even slight modifications in their crystal structure or chemical composition can significantly influence their physical behavior. To contribute to a better understanding of perovskite oxide properties, we have investigated the structural, elastic, electronic, and thermoelectric characteristics of the compound **$CeBeO_3$** and **$CeMgO_3$**. Our theoretical predictions are compared with available experimental data and previous theoretical studies on similar perovskite oxides.

III.2 Calculation methods and data

In our work, we employed an ab initio method, namely the full-potential linearized augmented plane-wave method (FP-LAPW) **[1]**, which is based on density functional theory (DFT) **[2]** as implemented in the WIEN2k code **[3]**. Among the exchange-correlation functionals, the generalized gradient approximation (GGA) **[4-5]** and the Tran and Blaha modified Becke-Johnson method (TB-mBJ) **[6]** were selected for this study. The explicit valence electrons for the $CeBeO_3$ and $CeMgO_3$ primal cell are Ce ($4f^1 5d^1 6s^2$), Be ($2s^2$), Mg ($3s^2$) and O ($2s^2 2p^4$). Muffin tin radius (RMT) values of 2.44 a.u, 1.49 a.u and 1.73 a.u were used to Ce, Be/Mg, and O elements respectively. Other input parameters, such as k-point mesh (K_{MAX}), RMT*wave-vector, Gaussian parameter and the maximum angular momentum were selected to 12*12*12, 7.0, 12 and 10 respectively. The energy interval between core and valence states was set to -6.0 Ry. The convergence criteria for the structure relaxation are set as 10^{-3} eV/atom and 0.03 eV/ Å for the energies and forces, respectively. Mechanical parameters were derived from elastic constants using the IRELAST package developed by J. Morteza **[7]**. Optical responses were determined by the complex dielectric function **$\varepsilon(\omega)$** through the Kramer–Kronig relation **[8-10]**. The electron transport properties are determined under a fine mesh of 46×46×46 by the semi-classical Boltzmann transport equation (BTE) **[11]** as given in the BoltzTraP code.

III.3 Structural properties

The crystal structure of **$CeBeO_3$** and **$CeMgO_3$** perovskite materials, drawn using the Vesta software **[12]** is shown in **Figure III.1**. These compounds crystallize in a cubic structure with the space group $\boldsymbol{Pm-3m}$ $(\boldsymbol{N°221})$**,** where the trivalent inorganic cation (Ce^{3+}) occupies

the **A** site, the divalent cations (Be^{2+} or Mg^{2+}) is situated at the **B** site, and the oxygen anion is positioned at site **X**. In this structure, each B-site cation coordinates with six oxygen anions forming a network of corner-sharing $[BO_6]^{4-}$ octahedra. The cerium atom resides in the cuboctahedral cavity formed between the octahedra, occupying the eight corners of the cubic lattice [position 1a (0, 0, 0)]. The beryllium (magnesium) ions are located at the lattice center [position 1b (½, ½, ½)], while the oxygen atoms are positioned in the middle of each edge [position 3d (0, 0, ½)] **[13-15]**.

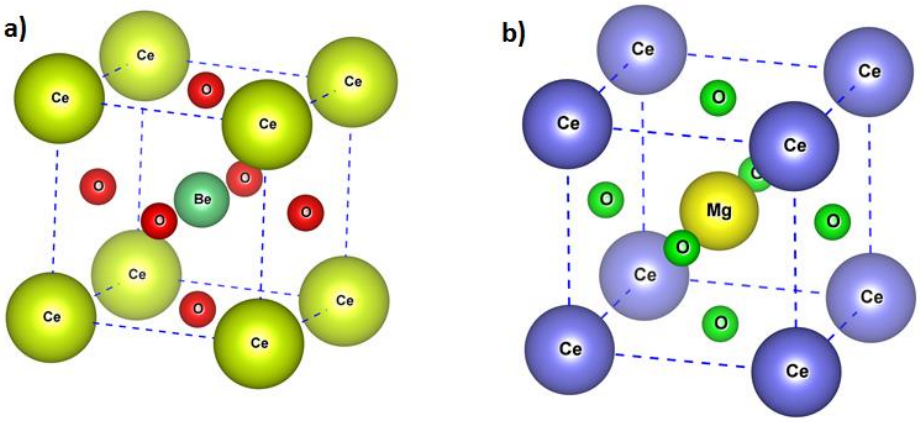

Figure III.1: Crystal structure for $CeBeO_3$ and $CeMgO_3$ perovskite compounds

The equilibrium structural parameters of the **$CeBeO_3$** and **$CeMgO_3$** compounds were determined by calculating the total energy for various lattice parameters and fitting the calculated values to the Birch–Murnaghan equation of state given by the following expression:

$$E_T(V) = \frac{B_0 V}{B_0'}\left[\frac{\left(V_0/V\right)}{B_0' - 1} + 1\right] + E_0 - \frac{V_0 B_0}{B_0' - 1} \qquad \textbf{(III. 1)}$$

Where V_0 is the static equilibrium volume of the primitive cell**,** E_0 is the total energy per primitive cell at equilibrium**,** B_0 is the bulk modulus and B_0' **is** its pressure derivative at constant temperature. The values of V_0 and E_0 are obtained from the minimum of the $E_T(V)$ curve**,** while the bulk modulus **B** is determined from the curvature at V_0 using the following relation **(III.2)**.

$$B_0 = V\frac{d^2E_T}{dV^2} \qquad \textbf{(III. 2)}$$

The optimization computations were conducted in the nonmagnetic (NM), ferromagnetic (FM), and antiferromagnetic (AFM) states. For both perovskites, the lowest ground state energies were observed in the NM configuration, with energy values of -18212.408936 Ry for **$CeBeO_3$** and -18583.482478 Ry for **$CeMgO_3$**. Consequently, all subsequent computations will be

performed in this non-magnetic state, as it represents the most energetically stable state. The calculated lattice parameters are 3.60 Å for $CeBeO_3$ and 3.85 Å for $CeMgO_3$. These values are in perfect harmony with those of other oxide perovskite, type semiconductor, such as $SrVO_3$ (3.86 Å) **[16]**, $CsGaO_3$ (3.75 Å) **[17],** and $AgNbO_3$ (3.95 Å) **[18]**. In comparison to $CeBeO_3$ perovskite, the $CeMgO_3$ compound exhibits a larger $\mathbf{a_0}$ value, attributed to the larger atomic radius of Mg (1.45 Å) compared to Be (1.12 Å). For a more detailed description of the crystal structure, we calculated bond lengths, including Ce-O, Ce-Be, Ce-Mg, Be-O, and Mg-O. The values, summarized in **Table III.1**, reveal an increasing trend as the B cation varies from Be to Mg. This variation in bond lengths is likely influenced by the electronegativity difference and the size between Be and Mg atoms. Furthermore, the lattice parameter of **$CeBeO_3$** perovskite is 7% larger than that of **$CeMgO_3$** perovskite, a proportion reflected in the average lengths of Be-O and Mg-O bonds. This comparative rate is consistent across the two-perovskite structures.

Table III.1 *Calculated structural equilibrium lattice constant* $\boldsymbol{a}(\text{Å})$*, the pressure derivatives* ***B'****, ground state energies* ***Emin (Ry)****, cohesive energy* $\boldsymbol{E_{coh}(eV/atom)}$*, formation energy* $\Delta\boldsymbol{H_f(eV/atom)}$ *and bond length* (Å) *of* ***$CeBeO_3$*** *and* ***$CeMgO_3$*** *perovskites.*

Alloys	State	a	B_0'	Emin	Ec	ΔH_f	Bond length
$CeBeO_3$	**NM**	**3.60**	**4.36**	**-18212.408936**	**-6.44**	**-1.18**	Ce-O = 2.54 Be-O = 1.80 Ce-Be = 3.11
	FM	3.60	4.24	-18212.408667	-6.43	-1.14	
	AFM	3.62	4.11	-18212.408515	-7.23	-1.14	
$CeMgO_3$	**NM**	**3.85**	**4.25**	**-18583.482478**	**-5.85**	**-1.11**	Ce-O = 2.72 Mg-O = 1.92 Ce-Mg = 3.33
	FM	3.85	4.01	-18583.482473	-5.87	-1.09	
	AFM	3.88	4.39	-18583.482453	-6.77	-1.10	

In order to evaluate the structural stability and potential synthesis of both materials, we calculate the formation energies $\Delta\boldsymbol{H_f}$ $(\boldsymbol{eq\ III.3})$ and cohesion energies $\boldsymbol{E_{coh}}$ $(\boldsymbol{eq\ III.4})$ **[19]**.

$$\Delta H_f = E_{XYZ_3}^{tot} - \left(E_X^{bulk} + E_Y^{bulk} + 3E_Z^{bulk}\right) \qquad (\mathbf{III.3})$$

$$E_{coh} = E_{XYZ_3}^{tot} - \left(E_X^{iso} + E_Y^{iso} + 3E_Z^{iso}\right) \qquad (\mathbf{III.4})$$

Where $E_{XYZ_3}^{tot}$ represents the total energy of the primitive cell, $\mathbf{E_{bulk}}$ is the energy per atom of constituent atoms in bulk and $\mathbf{E^{iso}}$ is the energy of an isolated atom. The negative values obtained for ΔH_f (**$CeBeO_3$**: -0.434 Ry, **$CeMgO_3$**: -0.408 Ry) indicate thermodynamic stability in both compounds, confirming the feasibility of their synthesis. Additionally, the negative values of E_{coh} (refer to **Table III. 1**) substantiate the structural stability of these perovskites.

III.4 Electronic properties

A comprehensive understanding of a material's electronic structure is essential for predicting and tailoring its physical and chemical properties. For the cubic perovskites **$CeBeO_3$** and **$CeMgO_3$**, this requires a detailed analysis of their electronic band structures and densities of states (both total and partial). These analyses offer key insights into the distribution of electronic states across different energy ranges and reveal the nature of bonding interactions among Ce, the **B**-site cations (Be/Mg), and **O** atoms. In particular, they help identify the dominant atomic orbitals contributing to the valence and conduction bands, clarify hybridization effects, and assess how **B**-site substitution influences the electronic behavior. Such insights are crucial for optimizing these materials for electronic, optical, and energy-related applications.

a) Band structure

In this part, we explore the electronic properties of oxide cubic perovskites **$CeBO_3$** (B= Be and Mg), properties which are summed up by the energy band structures by using the GGA approximation, we determined that the band gaps for the **$CeBeO_3$** and **$CeMgO_3$** compounds are 0.47 and 0.33 eV, respectively. To address the underestimation of the band gap resulting from the GGA approximation, we employed the Tran-Blaha modified Becke-Johnson (TB-mBJ) approach. This adjustment led to a significant enhancement in the band gaps **(Table III. 2)**, resulting in new values of 0.73 eV (+55%) for **$CeBeO_3$** and 0.51 eV (+54%) for **$CeMgO_3$**. Similar improvements have been observed in various perovskite materials, including $CsMgCl_3$ **[20]**, $PbGeO_3$ **[21]**, $TlPbCl_3$ **[22]** and $ANbO_3$ **[23]**. These low values of bandgap energies allow easy transport of electrons from the VBM to VBM; thus, optical absorption and conductivity may become more advantageous for optoelectronic applications. **Figure III. 2**, gives along the following k-path: **R-Γ-X-M-Γ**, the electronic band structures of the **$CeBeO_3$** and **$CeMgO_3$** materials calculated by the TB-mBJ approach. The electronic band structure provides us the energy range in which a probable number of electrons exist (energy band) and the region where there are no electrons (gap band). One can see that the minima of conduction band (CBM) and

maxima of valence band (VBM) do not overlap with each other around the Fermi level. This implies that both **$CeBeO_3$** and **$CeMgO_3$** exhibit semiconductor behavior. Both predicted perovskites, **$CeBeO_3$** and **$CeMgO_3$**, exhibit energy bandgaps of an indirect nature (Σ-M for **$CeBeO_3$** and M-X for **$CeMgO_3$**).

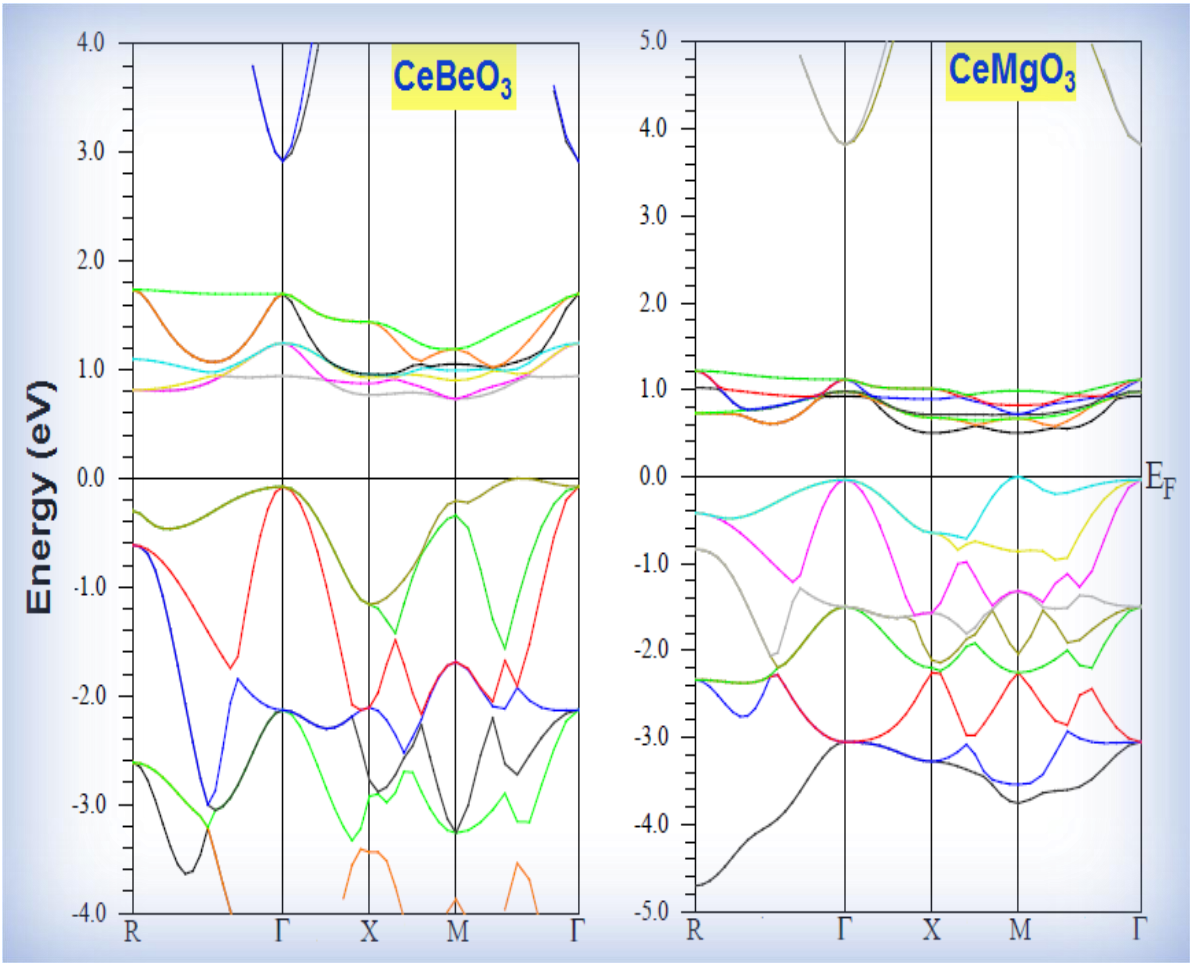

Figure III.2: The band structures for (a) **$CeBeO_3$** and (b) **$CeMgO_3$** calculated using TB-mBJ approximation.

A modification in the conduction band minimum is observed when the **B**-cation site is replaced by a less electronegative element with a larger ionic radius ($r_{Mg} > r_{Be}$), leading to a decrease in the gap energy **(Eg)**. This modification in **Eg** values results in a shift of the band gap towards the infrared region. The valence band maximum (VBM) and the conduction band minimum (CBM) are formed through a covalent interaction between the Ce-4f and O-2p states, and the gap between them arises from their hybridization. The range of the obtained bandgap values has also been noticed in many oxide perovskite such as $BaTbO_3$ **[24]**, $CuScO_3$ and $CuSnO_3$ **[25]**, Mn_2ScTaO_6 **[26]**, Mn_2FeMoO_6 **[27]** and $BiFeO_3$ **[28].**

Table III. 2 Calculated band gap E_g*, optical gap of* **$CeBeO_3$** *and* **$CeMgO_3$** *perovskites*			
Alloy	**Gap (eV)**		**Optical Gap (eV)**
	GGA	**TB-mBJ**	**TB-mBJ**
$CeBeO_3$	0.47	0.73	0.95
$CeMgO_3$	0.33	0.51	0.53

b) Density of state

In order to gain a deeper understanding of the electronic characteristics of the cubic oxide perovskites **$CeBO_3$** (where B = Be or Mg), we conducted a comprehensive analysis of their electronic density of states (DOS). The DOS represents the distribution of electronic states as a function of energy, indicating the number of states available for occupation at each energy level. To further refine this analysis, we examined the partial density of states (PDOS), which decomposes the total DOS into contributions from specific atomic orbitals (**s**, **p**, **d**, and **f**). This approach provides valuable information on the role of each element in chemical bonding and the nature of orbital interactions within the crystal structure.

For these calculations, we employed the Tran-Blaha modified Becke-Johnson (TB-mBJ) potential, which is well-known for improving the accuracy of band gap estimations compared to standard GGA approximations. Using this method, we computed both the total DOS (TDOS) and the PDOS, taking the Fermi level as the zero-energy reference point. The results are illustrated in **Figures III.3** and **III.4**, where we present the TDOS and PDOS plots for **$CeBeO_3$** and **$CeMgO_3$** in their non-magnetic configurations. These plots cover an energy window ranging from -10 eV to +10 eV, which includes all significant features of the electronic structure. The Fermi energy (**En**) is marked by a dashed vertical line for clarity.

A closer examination of the TDOS graphs (**Figures III.3a** and **III.4a)** reveals four distinct energy regions, each corresponding to different electronic contributions. The first region extends from approximately -7 eV to 0 eV for **$CeBeO_3$** and from -5 eV to 0 eV for **$CeMgO_3$**. This energy interval is predominantly influenced by the strong contribution of the oxygen **2p** orbitals, as shown in the PDOS plots (**Figures III.3b** and **III.4b**). These oxygen-derived states play a fundamental role in the valence band formation and highlight the significant hybridization between **O-2p** and the cation states within the perovskite lattice.

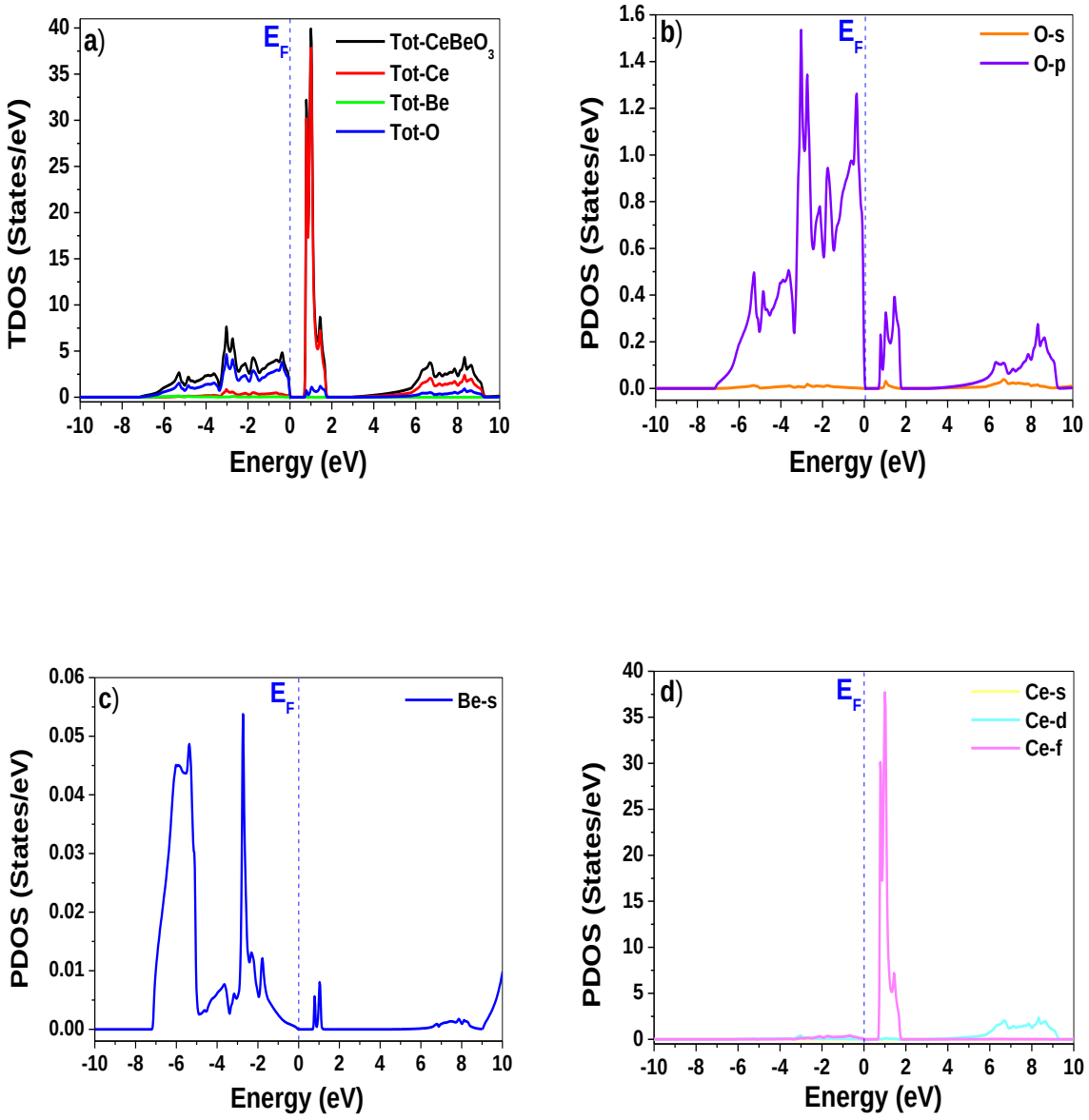

Figure III.3 Total and partial density of states (TDOS / PDOS) for $CeBeO_3$ calculated using TB-mBJ approximation.

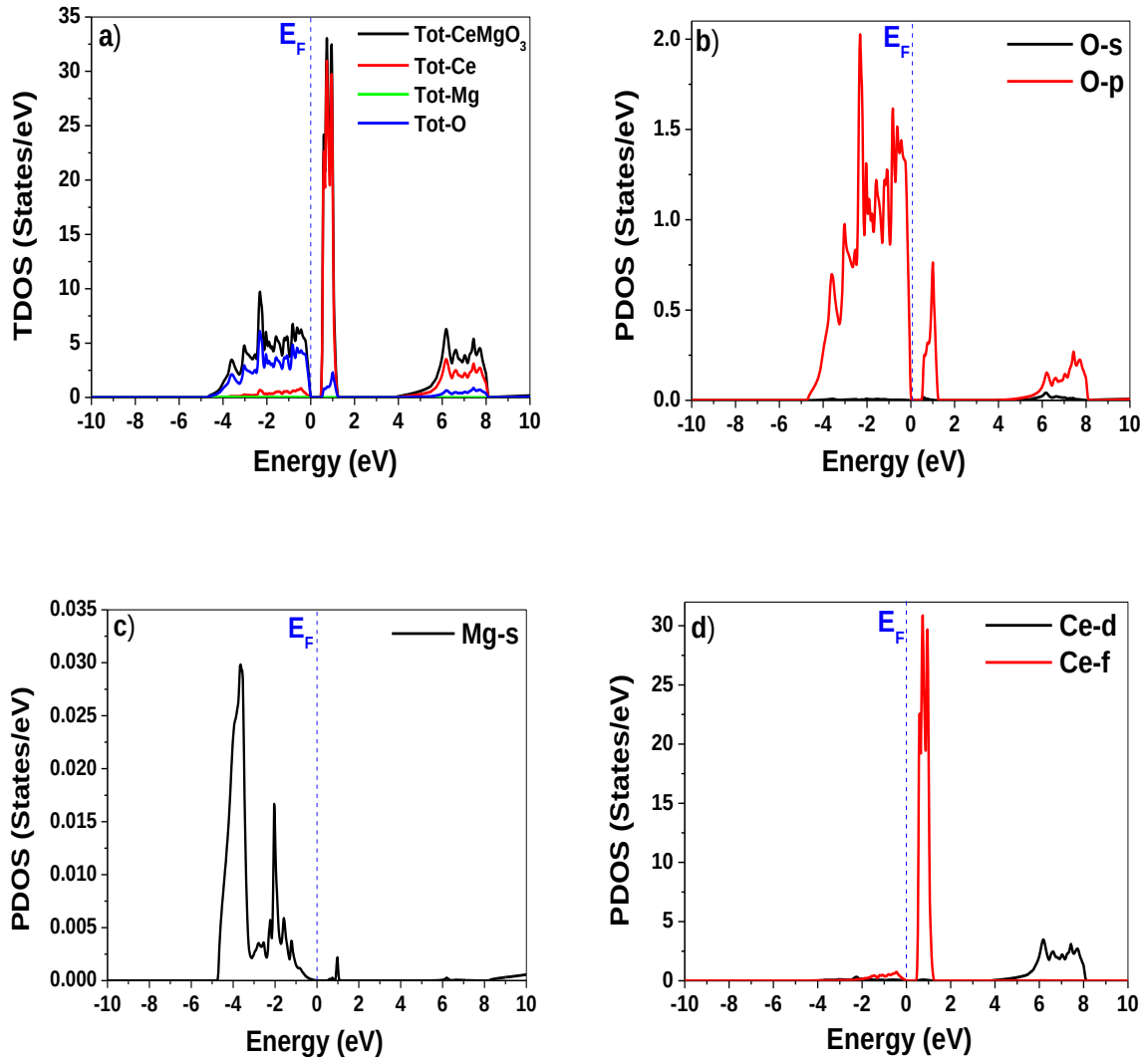

Figure III.4 Total and partial density of states (TDOS / PDOS) for $CeMgO_3$ calculated using TB- mBJ approximation.

The other elements present in the structure contribute only very weakly to these energy regions, their influence being practically negligible (as illustrated in **Figures III.3c, III.3d,** and **III.4c, III.4d**). The second energy region is characterized by the appearance of a moderate interval, estimated at about 0.73 eV for **$CeBeO_3$** and 0.51 eV for **$CeMgO_3$**, which confirms the semiconducting nature of these perovskite materials. The third energy region extends from 1.7 to 2.9 eV for **$CeBeO_3$** and from 1.2 to 3.8 eV for **$CeMgO_3$** ; this zone is dominated by the contribution of the **Ce-4f** orbitals, indicating a strong involvement of the **4f** electrons in the electronic states located at these energy levels. Finally, beyond 5 eV, the energy spectrum is mainly governed by the **Ce-5d** orbitals, reflecting a transition toward more dispersive and higher-energy electronic states.

III.5. Elastic properties

The elasticity of a solid describes its ability to undergo small deformations under external mechanical stresses. These stresses are represented by tensors that specify both the force direction and the plane on which they act. For cubic perovskites such as **$CeBeO_3$** and **$CeMgO_3$**, elastic properties are closely linked to fundamental solid-state characteristics, including the equation of state, specific heat, thermal expansion, Debye temperature, and melting point. Elastic constants provide essential insights into the bonding strength between adjacent atomic planes, the anisotropic nature of the bonding, and the overall structural stability of these materials.

The three independent elastic constants for a cubic single crystal are **C_{11}**, **C_{12}** and **C_{44}**. The crystal's resistance to uniaxial compression along the principal directions, or to tensile or compressive stress applied on the (100) planes along the [100] direction, is represented by the elastic constant **C_{11}**. The resistance to shear stress applied on the (100) plane along the [010] direction is reflected in the elastic constant **C_{44}**. On the other hand, **C_{12}** alone does not have a straightforward physical meaning, but when paired with other constants, it offers more insight into the elastic behavior of cubic materials. For instance, the following expression can be used to estimate the bulk modulus **B** by combining **C_{11}** and **C_{12}**:

$$B = \frac{1}{3}(C_{11} + 2C_{12}) \qquad (\mathbf{III.5})$$

Understanding the three independent elastic constants **C_{11}**, **C_{12}**, **C_{44}** [29] is fundamental for assessing essential mechanical properties such as hardness, stiffness, ductility, brittleness, stability, and the nature of atomic bondings. These constants serve as the basis for deducing other mechanical parameters like shear modulus (G), elastic anisotropy factor (A), Young's modulus (ν), and Poisson's ratio (ν). Equations **(III.5)** to **(III.9)** provide the mathematical expressions through which these main mechanical parameters can be estimated [30].

$$G = \frac{C_{11} - C_{12} + 3C_{44}}{5} \qquad (\mathbf{III.6})$$

$$A = \frac{2C_{44}}{C_{11} - C_{12}} \qquad (\mathbf{III.7})$$

$$E = \frac{9BG}{3B + G} \qquad (\mathbf{III.8})$$

$$\nu = \frac{3B - E}{6B} \qquad (\mathbf{III.9})$$

Examining the elastic constants achieved at zero pressure **(Table III.3),** we find that the mechanical stability given by Born-Huang criteria [31] **($C_{11} - C_{12} > 0$)**; **($C_{11} + 2C_{12} > 0$)**; **($C_{11} > 0$)**; **($C_{44} > 0$)** and **($C_{12} < B < C_{11}$)** is entirely satisfied for both perovskites. The **C_{11}** elastic constant signifies the material's flexibility in intermolecular interactions along the lattice direction, while **C_{12}** and **C_{44}** denote flexibility resulting from phase transformation [32]. In the case of **$CeBeO_3$**, the **C_{11}** value surpasses those of **C_{12}** and **C_{44}**, indicating low resistance to shear deformation and greater resistance to unidirectional compression [33]. Both perovskites exhibit high compressibility modulus values, confirming their resistance to compression and limited flexibility or deformability. The shear modulus, also known as the rigidity modulus (G), quantifies the change in bond angle when a material experiences elastic shear stress. The order of magnitude of the calculated shear modulus values (168 GPa for **$CeMgO_3$** and 90 GPa for $CeBeO_3$) indicates that both materials exhibit covalent and rigid behavior. Young's modulus measures a material's ability to resist changes in length during lengthwise compression. Covalently bonded and hard materials typically have higher values of Young's modulus, as observed in the studied compounds. Poisson's ratio can predict the bonding nature in solids. A completely covalent crystal is characterized with a Poisson's ratio equal or less than 0.1 (as in the case of **$CeMgO_3$**). A perfectly metallic compound possesses a Poisson's ratio equal to or greater than 0.33 [34]. The Poisson's ratio of **$CeBeO_3$** lies between 0.1 and 0.33, indicating that the chemical bonding is a combination of metallic and covalent natures [35]. Anisotropy factor (A) defines if a material acts in an isotropic or anisotropic direction. A value of $A \neq 1$ indicates anisotropic behavior, while A=1 signifies isotropy. The anisotropy factor of **$CeBeO_3$** is larger than that of **$CeMgO_3$**, this may be is due to the increase in atomic radius ($R_{Mg} > R_{Be}$). Both perovskites exhibit elastically anisotropic behavior, with an anisotropy factor greater than unity ($A > 1$) [36], indicating that mechanical properties vary in all directions. The recorded degree of anisotropy is insignificant, thus implying a low probability of microcrack formation. The Pugh B/G criterion is employed to predict the ductility and fragility of a material [37]. Materials are considered ductile when $B/G > 1.75$ and brittle when $B/G < 1.75$. Based on the values listed in **Table III. 3**, we can conclude that **$CeBeO_3$** is ductile and **$CeMgO_3$** is brittle.

Table III.3 *The computed elastic constants* ***Cij (GPa),*** *bulk modulus* ***B(GPa)****, Shear modulus* ***G(GPa)****, Young's modulus* ***E(GPa)****, Poisson's ratio* (**ν**)*, anisotropic factor* (***A)****, and Pugh's ratio* ***(B/ G)*** *of* **$CeBeO_3$** *and* **$CeMgO_3$** *perovskites.*

Alloys	C_{11}	C_{12}	C_{44}	B	G	E	ν	A	B/G
$CeBeO_3$	251.61	126.54	106.33	168.27	90.95	231.20	0.27	1.58	1.85
$CeMgO_3$	345.04	43.01	180.82	143.66	168.91	364.05	0.08	1.20	0.85

III.6 Optical properties

The comprehension of optical properties, including the complex dielectric function $\varepsilon(\omega)$, absorption coefficient $a(\omega)$, refractive index $n(\omega)$, reflectivity $R(\omega)$, and energy loss function $L(\omega)$, is pivotal for determining the suitability of ternary **$CeBO_3$** (B = Be and Mg) oxide-perovskites in diverse applications within the optoelectronic field and allied devices. The response of these materials to electromagnetic radiation is linked to the speed of electron transition and recombination. In the context of semiconductor-type materials, such as the compounds under investigation, the research focuses exclusively on inter-band transitions due to their significant role. It's worth noting that intra-band transitions are more pertinent to materials with a metallic nature **[38]**.

III.6.1 Computational approach for optical properties

The description of these optical effects requires parameters that quantify, on both a macroscopic and intrinsic scale, the interaction between an electromagnetic wave and a material medium (excluding scattering, which also depends on the material's morphology). According to Maxwell's equations in a medium, the response of a material to an electromagnetic wave can be completely characterized by three fundamental parameters that fully describe the material. The general equations of electromagnetism for macroscopic fields in a vacuum, in the presence of charges and currents, can be expressed in the SI system as follows :

$$\nabla.\vec{D} = \rho \qquad \nabla.\vec{B} = 0$$

$$\nabla \times \vec{H} = \vec{j} + \frac{\partial \vec{D}}{\partial t} \qquad (\mathbf{III.10})$$

$$\nabla.\vec{E} = -\frac{\partial \vec{B}}{\partial t}$$

These equations are sufficient to describe the entire interaction of an electromagnetic wave with matter, provided the assumptions mentioned above are satisfied. In these equations ρ and $\vec{j}$ are

considered the sources of the electric and magnetic fields, $\vec{D}$ and $\vec{H}$. All of these quantities are vectors $\vec{j}$, $\vec{D}$ and $\vec{B}$ (except **ρ**) are related in pairs through constitutive relations:

$$\vec{j} = \bar{\sigma}\,\vec{E}, \qquad \vec{D} = \bar{\varepsilon}\,\vec{E}, \qquad \vec{B} = \bar{\mu}\,\vec{H} \tag{III.11}$$

Here, we assume the media are linear, meaning that $\vec{j}$, $\vec{D}$ and $\vec{B}$ do not depend on higher-order powers of $\vec{E}$ and $\vec{H}$. The dielectric function $\bar{\varepsilon}$ can be considered a local quantity that depends only on the angular frequency **ω**, since in the optical range the wave vector $\vec{k}$ is small.

In the case of a dynamic field, the dielectric constant **ε(ω)** is a complex function (**eq. III.12)**:

$$\varepsilon(\omega) = \varepsilon_1(\omega) + i\varepsilon_2(\omega) \tag{III.12}$$

Where $\varepsilon_2(\omega)$ represents the real transition between the occupied and unoccupied states while $\varepsilon_1(\omega)$ depicts the electronic polarizability under incident light [39]. The imaginary part of the dielectric function $\varepsilon_2(\omega)$ is derived from the electronic band structure computations with the help of the following relation

$$\varepsilon_2(\omega) = \left(\frac{4\pi^2 e^2}{m^2\omega^2}\right)\sum_{i,j}\int \langle i|M|j\rangle^2 f_i(1-f_i)\delta\left(E_j - E_i - \omega\right)d^3k \tag{III.13}$$

Where e, m, ω and M represent the electron charge, electron mass, photon frequency and dipole matrix, respectively. E_i is the electron energy of the initial state, E_j is the electron energy of the final state, and f_i is the Fermi occupation factor of the single-particle state i. The real part $\varepsilon_1(\omega)$ of the dielectric function derives from $\varepsilon_2(\omega)$ by using the Kramers-Kronig relations [40-42]:

$$\varepsilon_1(\omega) = 1 + \frac{2}{\pi}P\int_0^{\infty}\frac{\omega'\varepsilon_2(\omega')}{\omega'^2 - \omega^2}d\omega' \tag{III.14}$$

Where P is the Cauchy principal value.

Other important optical parameters, such as the absorption coefficient $a(\omega)$, reflectivity $R(\omega)$, and refractive index $n(\omega)$, can be determined from the calculated values of the real and imaginary parts of the dielectric function. These fundamental quantities make it possible to derive the necessary relationships to characterize the optical behavior of the material [43]. They also provide an essential basis for analyzing optoelectronic performance and designing photonic devices.

$$a(\omega) = \frac{\sqrt{2\omega}}{c}\left(\sqrt{\varepsilon_1^2(\omega) + \varepsilon_2^2(\omega)} - \varepsilon_1(\omega)\right)^{1/2} \quad \textbf{(III. 15)}$$

$$R(\omega) = \left|\frac{\sqrt{\varepsilon(\omega)} - 1}{\sqrt{\varepsilon(\omega)} + 1}\right|^2 \quad \textbf{(III. 16)}$$

$$n(\omega) = \left[\frac{\sqrt{\varepsilon_1{}^2(\omega) + \varepsilon_2{}^2(\omega)} + \varepsilon_1(\omega)}{2}\right]^{1/2} \quad \textbf{(III. 17)}$$

a) The dielectric function

The dielectric function $\boldsymbol{\varepsilon(\omega)}$ serves as a crucial descriptor of a material's optical properties, offering insights into its linear response to an external electromagnetic field. **Figure III. 5a** illustrates the evolution of the real part $\boldsymbol{\varepsilon_1(\omega)}$, of the dielectric function across an incident energy spectrum from 0 to 12 eV. The real part $\boldsymbol{\varepsilon_1(\omega)}$, essentially unveils the degree of polarization exhibited by the material, a parameter determined through the Kramers-Kronig transformation **[44]**. The static dielectric constant, $\boldsymbol{\varepsilon_1(\omega)}$ manifests distinctively in **$CeBeO_3$** and **$CeMgO_3$**, with values of 14.22 and 105.28, respectively. The optical response of the **$CeBeO_3$** compound gradually increases from the zero-frequency limit and reaches its maximum value of 21.06 at 0.90 eV, then it tends towards low values with an almost linear profile in the visible and ultraviolet range. For the **$CeMgO_3$** compound, the value of $\boldsymbol{\varepsilon_1(\omega)}$ shows a drastic decrease, in the energy interval between 0 and 0.45 eV, it goes from its maximum value of 105.28 towards a negative value of -4,10. Between 0.45 and 0.85 eV, $\boldsymbol{\varepsilon_1(\omega)}$ goes from a negative value of -4.10 to 8.55, then it relapses in the visible and ultraviolet range to show a similar behavior to that of the **$CeBeO_3$** perovskite. The occurrence of negative values in $\boldsymbol{\varepsilon_1(\omega)}$ indicates energy loss within the material, resulting in poor light transmission and significant reflection. Particularly in the ultraviolet (UV) range, for energies surpassing 4 eV, $\boldsymbol{\varepsilon_1(\omega)}$ tends to hover around zero. This observation suggests the possible emergence of plasmonic-type oscillations **[45]**. Plasmonic oscillations can influence the behavior of light within the material, affecting its transmission and reflective properties. The absorption of photon energy by a material is quantified by the imaginary part of the dielectric function $\boldsymbol{\varepsilon_2(\omega)}$. The calculation of $\boldsymbol{\varepsilon_2(\omega)}$ involves the use of momentum matrix elements between occupied and unoccupied electronic states **[46]**. From **Figure III. 5b**, one can observed the rapid increase in $\boldsymbol{\varepsilon_2(\omega)}$ in the low energy area of **$CeMgO_3$** compared to **$CeBeO_3$**, leading to maximum peaks at 0.14 eV for $CeMgO_3$ and 1.16 eV for $CeBeO_3$. Beyond these peak values, a rapid decrease in $\boldsymbol{\varepsilon_2(\omega)}$ becomes apparent, a phenomenon associated with plasmon oscillations **[47]**. The highest

values of the real and imaginary components of the dielectric function in **$CeBO_3$** compounds (where B is either Be or Mg) manifest prominently within the infrared domain. This trend aligns with observations in various oxide-perovskites, including $NdInO_3$ **[48]**, $MgZnO_3$ **[49]**, $CsGaO_3$ **[17],** and $BaRuO_3$ **[50]**.

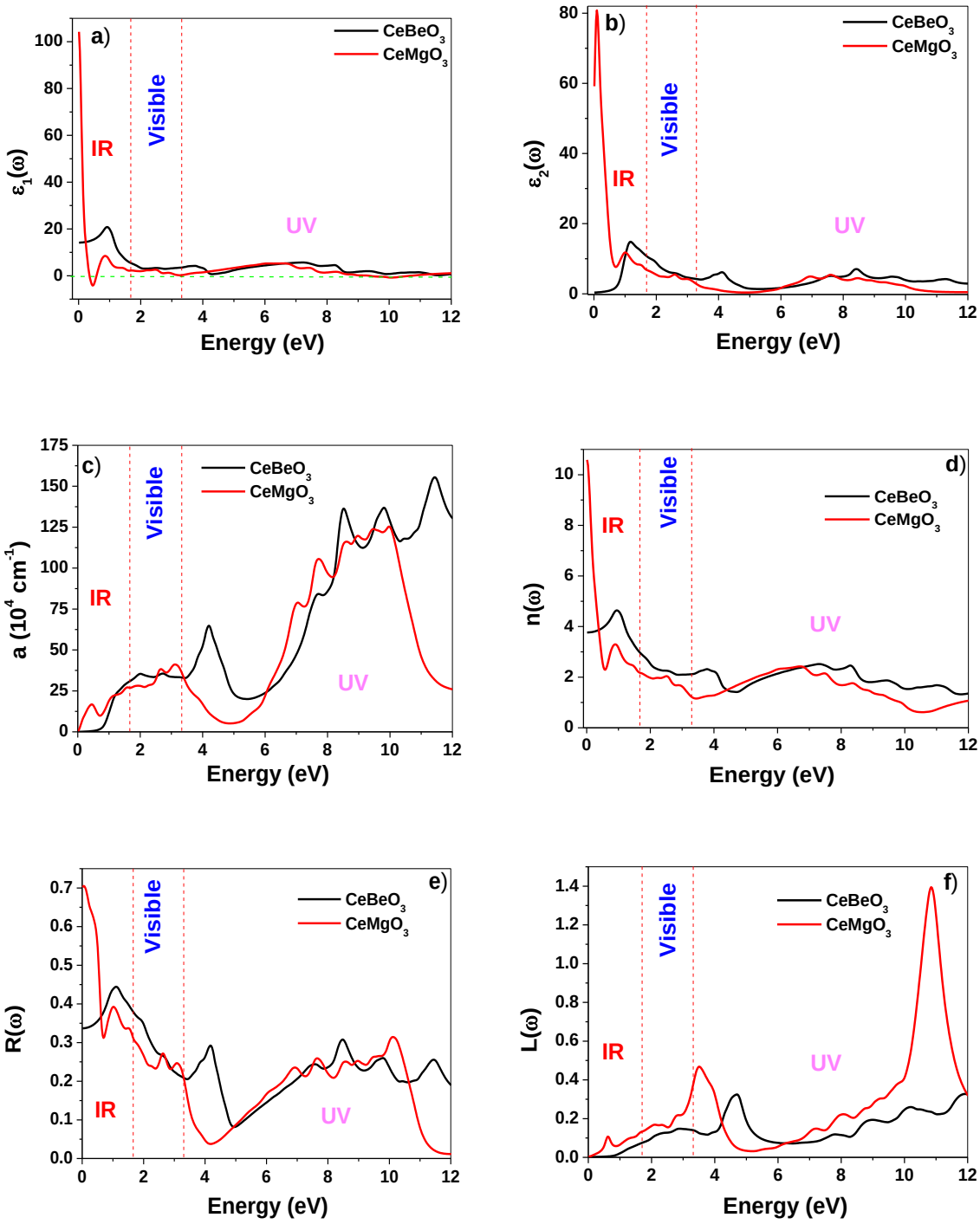

Figure III.5 Illustration of (a) real $\varepsilon_1(\omega)$ and (b) imaginary $\varepsilon_2(\omega)$ component of dielectric function, (c) absorption coefficient $a(\omega)$, (d) refractive index $n(\omega)$, (e) reflectivity $R(\omega)$ and (f) electron energy loss $L(\omega)$ for **$CeBeO_3$** and **$CeMgO_3$** perovskite compounds.

b) The absorption coefficient

The absorption coefficient $\boldsymbol{\alpha(\omega)}$ makes it possible to see the adequacy of a semiconductor against photocatalytic application. In **Figure III. 5c**, it is evident that all peaks originate from the origin, indicating zero photon absorption in the absence of light, specifically for zero incident photon energy. Within the visible domain, both ternary oxides perovskites exhibit a comparable absorption rate, approximately 40.10^4 cm^{-1}. This absorption rate surpasses values reported for various oxide perovskites, including $SrVO_3$, $BaVO_3$ **[16]**, $CaZrO_3$, $CaHfO_3$ **[51]**, and $CsNbO_3$ **[52]**. The maximum absorption coefficients $\boldsymbol{\alpha(\omega)}$ for **$CeBeO_3$** and **$CeMgO_3$** compounds are noteworthy, reaching values of 155.10^4 and 126.10^4 cm^{-1}, respectively. These peaks are observed in the ultraviolet range at energies of 11.42 eV and 9.95 eV. At higher energies within the ultraviolet domain, both perovskites exhibit a substantial absorption potential. This behavior hints at the possibility of interband transitions rather than the conventional valence band - conduction band transitions. The absorption spectrum width of both **$CeBeO_3$** and **$CeMgO_3$** perovskites spans a wide energy range, indicating their capacity to absorb frequencies across the spectrum.

c) The refractive index

The transparency of a material to light radiation is a property characterized by the refractive index $\boldsymbol{n(\omega)}$ **[53]. Figure III. 5d** gives the evolution of $\boldsymbol{n(\omega)}$ as a function of the photon energy for **$CeBO_3$** (B = Be, Mg) compounds. The static values $\mathbf{n(0)}$ are of 3.78 and 10.56 respectively for the **$CeBeO_3$** and **$CeMgO_3$** compounds. The highest values of $\mathbf{n(\omega)}$ are achieved in the near infrared range. Among both investigated perovskites, **$CeBeO_3$** has slightly elevated $\mathbf{n(\omega)}$ compared to **$CeMgO_3$**, i.e. the incident photons interact with more valence electrons, causing thus more polarization associated with a reduction in the speed of light. It can be seen that the substantial reflection occurred in the infrared region, domain where both perovskites exhibit their weakest absorption. The drop of the refractive index values in the visible domain is a result of the optical dispersion, i.e.; light separation into individual colors.

d) Reflectivity

Figure III. 5e depicts the evolution of reflectivity $\mathbf{R(\omega)}$ with respect to phonon energy. Reflectivity quantifies the percentage of light that a surface reflects under a given frequency of electromagnetic waves. The static values of $\mathbf{R(\omega)}$ are 34% and 70% for **$CeBeO_3$** and **$CeMgO_3$** compounds, respectively. In the energy range of 0 to 1.5 eV, $CeMgO_3$ exhibits a high reflectivity of around 71%, while $CeBeO_3$ shows a value of 44%. This result suggests that **$CeMgO_3$** is nearly opaque in the infrared domain. With a low $\mathbf{R(\omega)}$ value, approximately below

3% recorded around 4 eV (near-ultraviolet domain), **$CeMgO_3$** demonstrates a highly transparent character, positioning it as a potential candidate for transparent coatings **[54]**. Due to their interband transition, the two perovskites exhibit their maximum values of $\mathbf{R}(\boldsymbol{\omega})$ at low energy. In the visible range, the **$CeBeO_3$** compound has more throughput to that of **$CeMgO_3$**, making it good for lower excitation gap solar systems.

e) Energy loss function

Figure III .5f illustrates the variation of the energy loss function $\boldsymbol{L(\omega)}$ as a function of photon energy for **$CeBeO_3$** and **$CeMgO_3$** compounds. In the visible domain, $\boldsymbol{L(\omega)}$ is observed to be less than 0.15 for $CeBeO_3$ and 0.35 for **$CeMgO_3$** compound. Both perovskites exhibit a substantial increase in $\boldsymbol{L(\omega)}$ values in the ultraviolet (UV) range. The **$CeMgO_3$** compound displays two prominent peaks in the UV region. The first peak, measuring 0.47, is situated at 3.54 eV, while the more intense peak, with a value of 1.39, is located at 10.80 eV. For the **$CeBeO_3$** compound, a notable peak of 0.32, situated at 4.68 eV, has been observed. This peak corresponds to a decline in $\boldsymbol{\varepsilon_1(\omega)}$ within the same energy range. These energy losses are attributed to electronic excitations and the diffusion of fast electrons through the material. The maximum value of $\boldsymbol{L(\omega)}$ observed in the UV range is also found in this same energy range in other perovskite **[55]**.

The static values of the permittivity coefficient $\boldsymbol{\varepsilon_1(0)}$, refractive index $\boldsymbol{n(\omega)}$, and reflectivity $\boldsymbol{R(\omega)}$ are listed in **Table III.4**. As a conclusion to this optical study, the determined band gap energies of 0.73 eV for **$CeBeO_3$** (equivalent to 1698 nm in the Near Infrared) and 0.51 eV for **$CeMgO_3$** (equivalent to 2431 nm in the Near Infrared) suggest that these compounds may not be directly suitable for solar cells due to their band gap less than 1 eV. Nevertheless, external factors such as temperature, pressure, or doping hold the potential to modify their properties.

Table III. 4 *Calculated band gap* $\boldsymbol{E_g}$*, optical gap, static dielectric constant* $\boldsymbol{\varepsilon_1(0)}$*, static refractive index* $\boldsymbol{n(0)}$ *and static reflectivity* $\boldsymbol{R(0)}$ *of* **$CeBeO_3$** *and* **$CeMgO_3$** *perovskites.*

Alloys	$\boldsymbol{\varepsilon_1(0)}$	$\boldsymbol{n(0)}$	$\boldsymbol{R(0)}$
$CeBeO_3$	14.22	3.78	0.34
$CeMgO_3$	105.28	10.56	0.70

However, these semiconductor perovskites exhibit promise in the realm of optoelectronic components, finding applications in devices like light-emitting diodes (LEDs) and photodiodes.

Moreover, they can be harnessed for specific types of transistors and electronic devices, serving purposes such as near-infrared light sensors, heat sensors, or responding to other stimuli **[56-59]**. With narrow band gap of 0.73 eV and an absorption coefficient of 4.10^5 cm^{-1} in visible range, the **$CeBeO_3$** perovskite has potential suitability for absorbing specific wavelengths of sunlight, pointing to its potential utilization in certain contexts. In the absence of experimental data on bandgap energies and static dielectric constants, it becomes imperative to rely on first-principles predictions as the primary tool to obtain crucial optical information about these compounds.

III.7 Thermoelectric properties

Assessing the suitability of a compound for thermoelectric applications requires a comprehensive understanding of how temperature affects its transport properties. In this work, we employ the BoltzTraP code **[11]** within the framework of the constant relaxation time approximation for charge carriers, which is widely used for predicting thermoelectric performance. Based on semi-classical Boltzmann transport equations (BTE) **[60]**, this approach enables the calculation of essential transport parameters, including the Seebeck coefficient (**S**), electrical conductivity (**σ/τ**), and electronic thermal conductivity (**κe/τ**). Furthermore, the dimensionless figure of merit (**ZT**), which combines these properties with thermal and electrical contributions, is also evaluated to provide an overall measure of thermoelectric efficiency.

$$\sigma_{\alpha\beta}(T,\mu) = \frac{1}{\Omega}\int \sigma_{\alpha\beta}(\varepsilon)\left[-\partial f_{\mu}(T,\varepsilon)\right]d\varepsilon \qquad (III.18)$$

$$\kappa_{\alpha\beta}(T,\mu) = \frac{1}{e^2 T\Omega}\int \sigma_{\alpha\beta}\varepsilon(\varepsilon-\mu)^2 \ \frac{\partial f_{\mu}(T,\varepsilon)}{d\varepsilon} \qquad (III.19)$$

$$S = \frac{e}{T\sigma}\int \sigma_{\alpha\beta}(\varepsilon)(\varepsilon-\mu)\left[\frac{-\partial f_{\mu}(T,\varepsilon)}{\partial\varepsilon}\right] \qquad (III.20)$$

$$ZT = \frac{S^2\sigma T}{\kappa} \qquad (III.21)$$

Ω, f, μ, σ, κ, S and **Z** denotes respectively the unit-cell volume, Fermi-Dirac distribution function, chemical potential, electrical conductivity, thermal conductivity, Seebeck coefficient and merit factor. All transport properties are examined as functions of temperature (300, 600, and 900 K) and chemical potential (μ) within the range of –0.10 to +0.10 eV.

III.7.1 Temperature dependence of thermoelectric properties

e) Seebeck coefficient

One can see from **Fig III. 6a**, that the Seebeck coefficient (S) of the **$CeMgO_3$** compound achieves its maximum value of 279 μV/K at the room temperature. In contrast, the **$CeBeO_3$** compound attains its utmost value of 248 μV/K at 100 K while its value recorded at room temperature is of 241 μV/K. Throughout the entire temperature spectrum considered in this study, the Seebeck coefficients (S) consistently maintain positive values, indicating that holes are the dominant charge carriers, classifying these compounds as n-type conductors. As the temperature increases, there is a gradual decrease in the Seebeck coefficient (S) values. This trend is attributed to the diminishing contribution of high-energy charge carriers **[61]**. The nearly flat conduction band of **$CeMgO_3$**, as shown in the band structure, indicates a high Seebeck coefficient.

f) Electrical conductivity

The variation of the electrical conductivity per relaxation time (**σ/τ**) as a function of temperature for the **$CeBO_3$ (B = Be, Mg)** semiconductor perovskites is illustrated in **Figure III.6b**. This parameter plays a crucial role in evaluating the charge transport behavior of thermoelectric materials. The observed trend reveals a pronounced increase in **σ/τ** with rising temperature for both compounds, which is a characteristic feature of semiconducting materials. This significant growth in conductivity strongly supports and confirms the semiconducting nature that was previously inferred from the electronic band structure analysis. In the low-temperature region, around 100 K, both materials exhibit relatively low **σ/τ** values, reflecting the limited thermal excitation of charge carriers at these temperatures. However, as the temperature increases, thermal activation becomes more effective, leading to a sharp rise in **σ/τ**. For temperatures above 100 K, **$CeBeO_3$** consistently displays slightly higher σ/τ values compared to **$CeMgO_3$**, suggesting that the substitution of Be at the **B**-site provides a more favorable environment for carrier mobility or density. Quantitatively, for **$CeBeO_3$**, **σ/τ** increases significantly from 2.53×10^{18} $(\Omega \cdot m \cdot s)^{-1}$ at 100 K to 7.52×10^{19} $(\Omega \cdot m \cdot s)^{-1}$ at 1200 K, representing an almost 30-fold enhancement. In comparison, **$CeMgO_3$** exhibits a rise from 6.14×10^{17} $(\Omega \cdot m \cdot s)^{-1}$ at 100 K to 3.78×10^{19} $(\Omega \cdot m \cdot s)^{-1}$ at 1200 K, corresponding to a more than 60-fold increase. This notable increase with temperature indicates that both perovskites maintain a strong thermally activated conduction mechanism, which is consistent with their moderate band gaps predicted in the electronic structure calculations. These observations highlight that temperature has a significant impact on charge transport in these materials, and the higher **σ/τ** values of **$CeBeO_3$** may suggest

better potential for thermoelectric performance under high-temperature conditions compared to **$CeMgO_3$**.

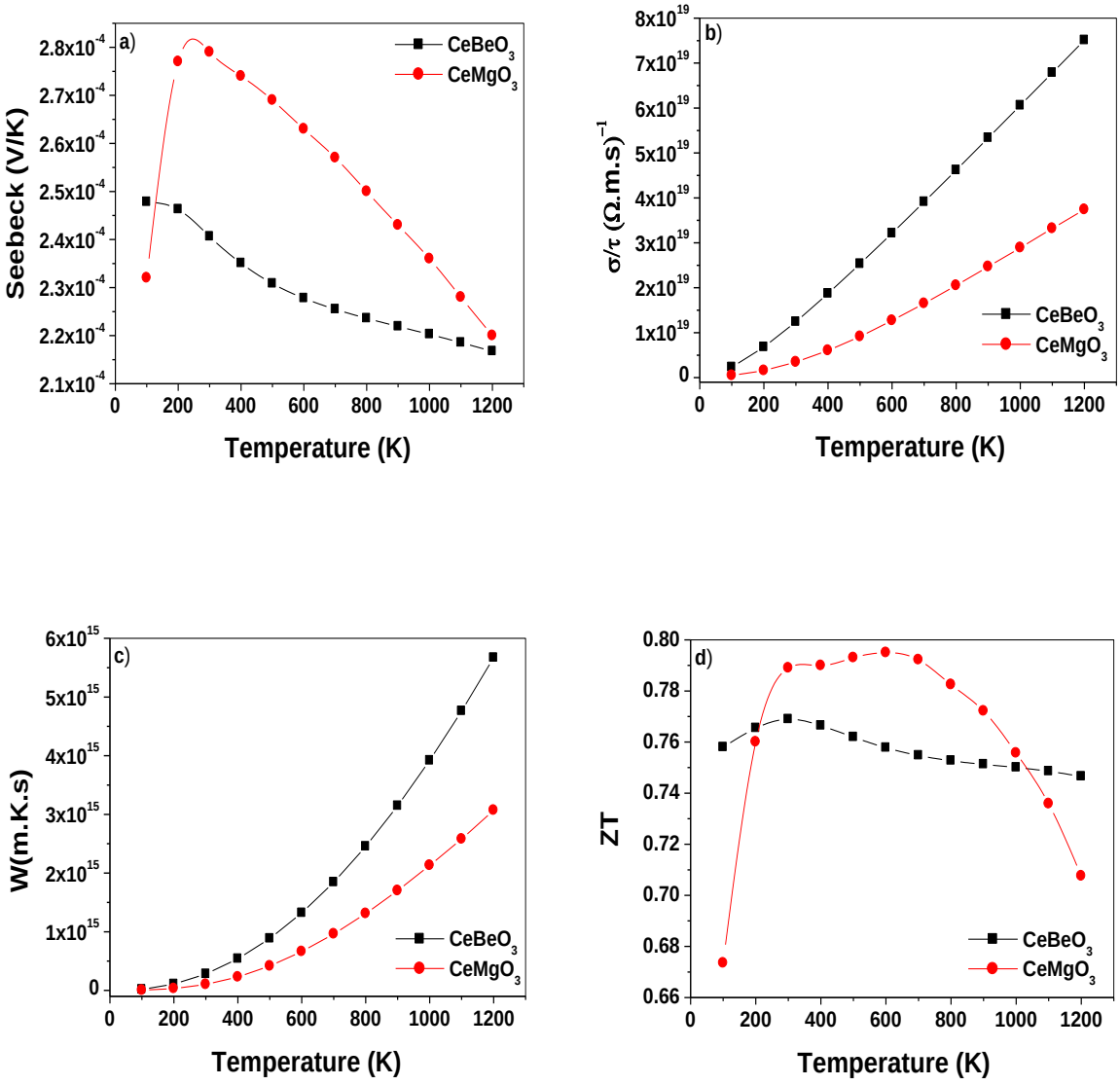

Figure III.6: Evolution versus temperature of (a) Seebeck coefficient, (b) electrical conductivity, (c) thermal conductivity and (d) Merit factor for $CeBeO_3$ and $CeMgO_3$ perovskite compounds.

g) Thermal conductivity

As shown in **Figure III.6c**, which plots the electronic thermal conductivity (κ_e/τ) of **$CeBO_3$** (B = Be, Mg) as a function of temperature **[62]**, κ_e/τ remains relatively low at low temperatures. At room temperature, the values for **$CeMgO_3$** and **$CeBeO_3$** perovskites are approximately **1.02 × 10^{14} W·m^{-1}·K^{-1}·s^{-1}** and **2.78 × 10^{14} W·m^{-1}·K^{-1}·s^{-1}**, respectively. At ambient temperature, these κ_e/τ values for both compounds are lower than those reported in the literature for $PbGeO_3$

[21] and $SrGeO_3$ **[63]** perovskites. With a temperature increase in steps of 100 K, κ_e/τ rises almost linearly and reaches optimal values of **3.06 × 10^{15} W·m^{-1}·K^{-1}·s^{-1}** and **5.69 × 10^{15} W·m^{-1}·K^{-1}·s^{-1}** at 1200 K for **$CeMgO_3$** and **$CeBeO_3$**, respectively. This linear behavior indicates that the electronic contribution to thermal transport is strongly temperature-dependent, which is consistent with the semiconducting nature of these materials. The higher κ_e/τ observed in **$CeBeO_3$** compared to **$CeMgO_3$** can be attributed to its lower lattice constant, which promotes better electron mobility.

h) Merit Factor

The merit factor (ZT) is one of the most important parameters for evaluating a material's potential in thermoelectric applications. Research in this area has shown that thermoelectric applications typically require ZT values approaching or exceeding 1. To achieve this, a material must exhibit high electrical conductivity and low thermal conductivity **[64]**. At 300 K, the ZT values obtained for **$CeMgO_3$** and **$CeBeO_3$** perovskites are 0.79 and 0.77, respectively (**Figure III.6d**). These values indicate that both materials possess excellent thermoelectric properties at room temperature. Moreover, these ZT values at 300 K surpass those reported for many oxide perovskites such as $NdCoO_3$, $PrCoO_3$ **[65]**, $LaFeO_3$ **[66]**, $TiGaO_3$, and $AgGaO_3$ **[67]**. Furthermore, the ZT values for both studied perovskites remain consistently above 0.70 across the entire temperature range from ambient up to 1200 K. This stability over a wide temperature range highlights their suitability for high-temperature thermoelectric devices, which is critical for waste heat recovery in industrial and automotive applications. Additionally, maintaining such high ZT values indicates a well-balanced combination of electrical and thermal transport properties, reflecting the effectiveness of their crystal structure in minimizing phonon contribution. These results suggest that **$CeMgO_3$** and **$CeBeO_3$** are promising candidates for next-generation thermoelectric systems where both performance and thermal stability are essential.

III.7.2 Thermoelectric properties versus chemical potential

e) Seebeck coefficient

Figure III. 7a and **8a** illustrates the evolution of the Seebeck coefficient according to the chemical potential ($\boldsymbol{\mu}$) at different temperatures and delimits the areas where the charge carriers is of **n**-or **p-type**. The positive values of ($\boldsymbol{\mu}$) is assigned to n-type doping level while p-type doping is attributed to negative values of $\boldsymbol{\mu}$. For $\mu - E_F = 0$ and T=300K, the value of the Seebeck coefficient in the n-type doping region is of 260 µV/K and 301µV/K for the **$CeBeO_3$** and **$CeMgO_3$** compounds, respectively. One can see in the valence band range that the value of

S remains almost zero up to the Fermi level then it gradually increases in the conduction band. In the conduction band range, a decrease in **S** values is observed with increasing temperature. For both studied perovskites, the utmost value of **S** take place in the positive side of chemical potential, which confirms the p-type nature of the charge carriers. The observed maximum Seebeck coefficient (**S**) values, reaching 1281 µV/K for **$CeBeO_3$** and 848 µV/K for **$CeMgO_3$**, at 300 K provide a crucial indication that these compounds hold substantial promise as excellent thermoelectric materials, particularly at room temperature.

i) Electrical conductivity

From **Figures III.7b** and **8b**, it is evident that all the curves overlap, indicating that temperature has an insignificant effect on the electrical conductivity (**σ/τ**). This behavior is typical for both studied alloys.

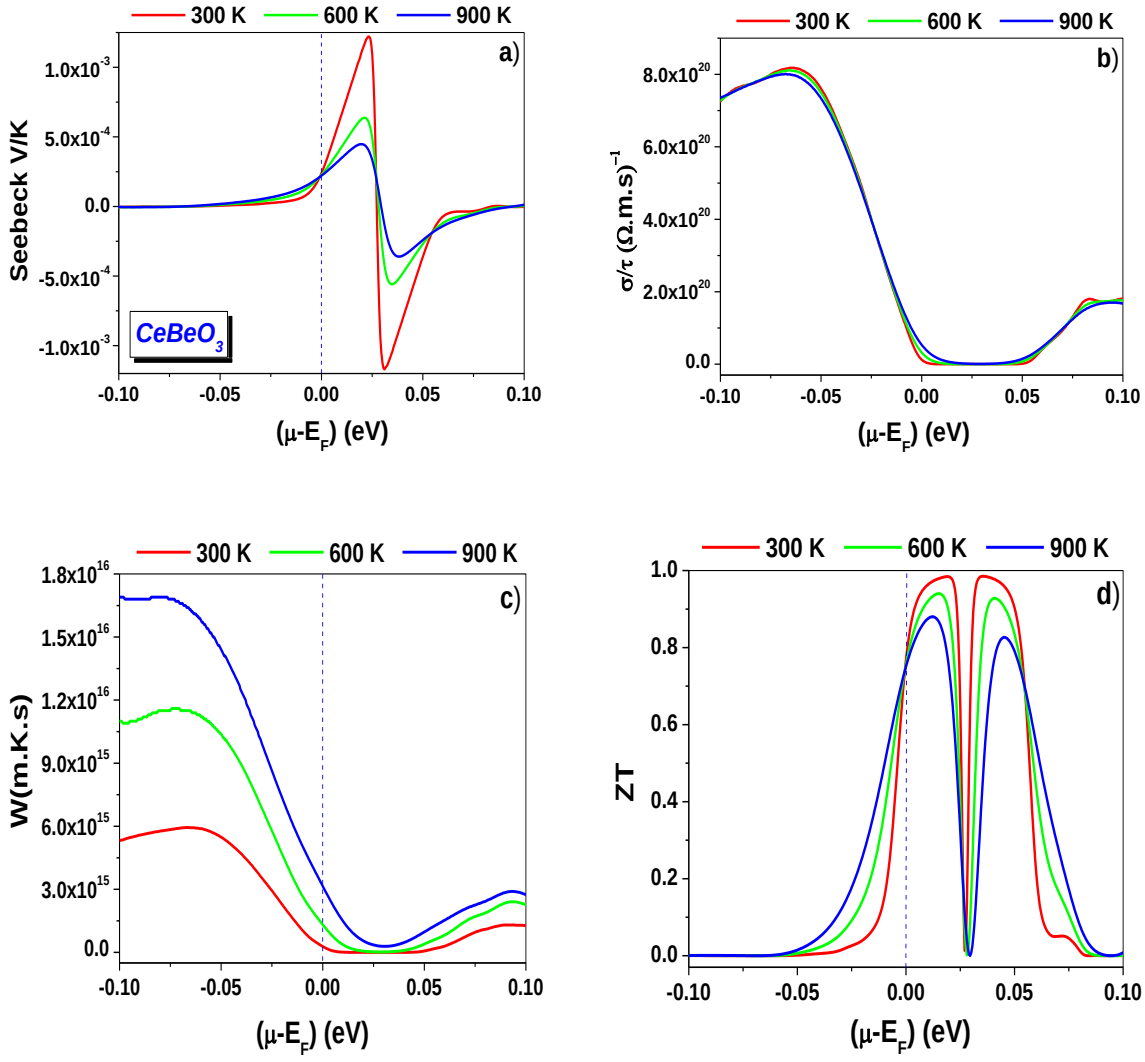

Figure III.7 Evolution versus chemical potential of (a) Seebeck coefficient, (b) electrical conductivity, (c) thermal conductivity and (d) Merit factor of $CeBeO_3$ at 300, 600 and 900K

The **σ/τ** values are higher in the **p**-type region than in the **n**-type region. For **$CeBeO_3$**, the electrical conductivity remains zero within the energy range of 0 to 0.05 eV, while for **$CeMgO_3$**, it is zero from 0 to 0.035 eV. It becomes nonzero in the regions where the Seebeck coefficient reaches its optimal values. This trend suggests that the transport properties are mainly controlled by the position of the chemical potential rather than the temperature variation.

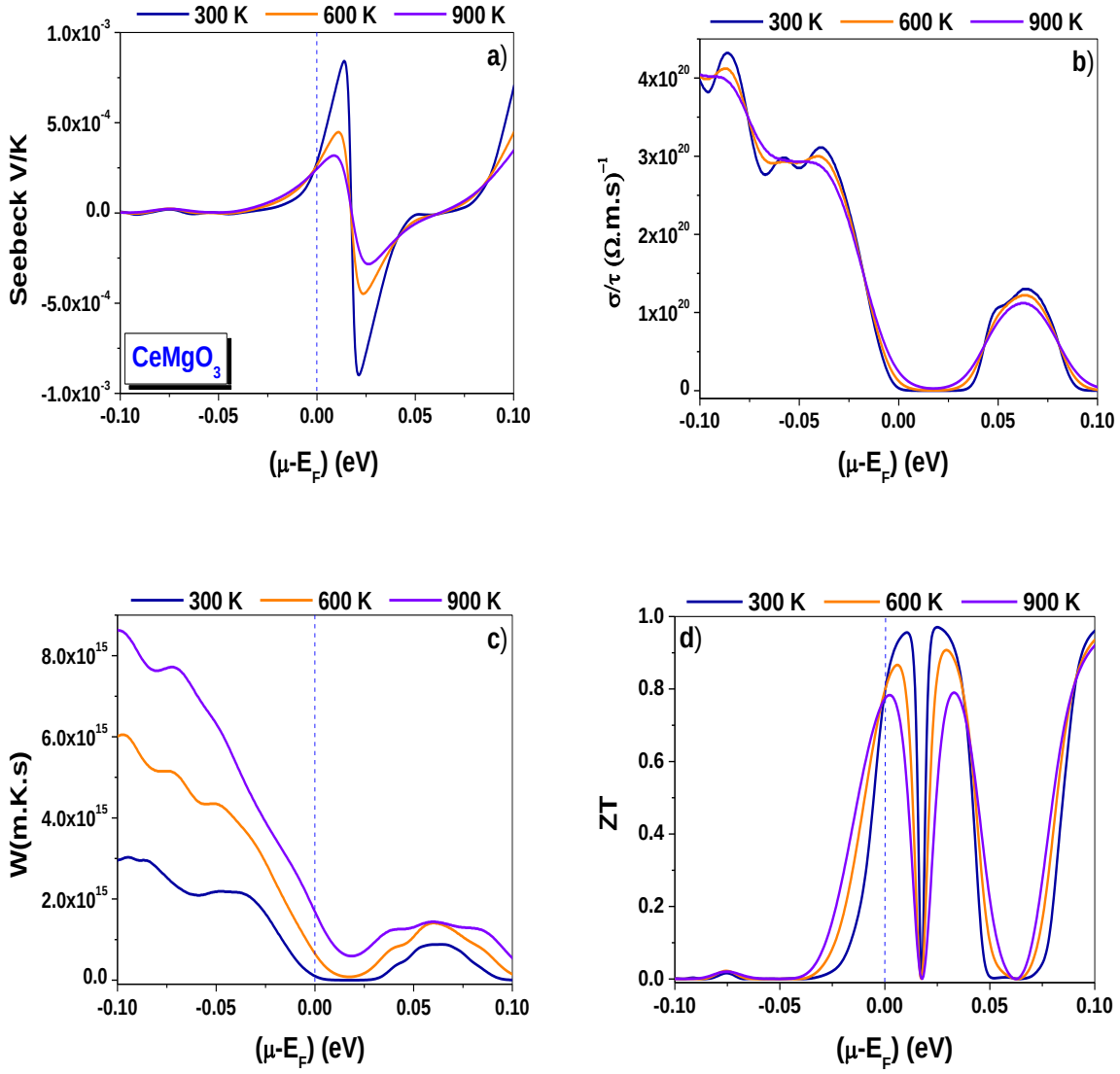

Figure III.8 Evolution versus chemical potential of (a) Seebeck coefficient, (b) electrical conductivity, (c) thermal conductivity and (d) Merit factor of $CeMgO_3$ at 300, 600 and 900K

Furthermore, the negligible influence of temperature implies that intrinsic scattering mechanisms dominate over thermal excitations in these materials. Such behavior is consistent with the semiconducting nature previously predicted from the band structure analysis, confirming that carrier concentration plays a more critical role than lattice vibrations in determining **σ/τ**.

c) Thermal conductivity

Figures 7c and **8c** illustrate the variation of electronic thermal conductivity (κ_e/τ) as a function of chemical potential. The maximum κ_e/τ values are observed in the p-type region. For **$CeBeO_3$**, these values occur at −0.1 eV and correspond to approximately 1.68×10^{16} $W\cdot m^{-1}\cdot K^{-1}\cdot s^{-1}$, 1.10×10^{16} $W\cdot m^{-1}\cdot K^{-1}\cdot s^{-1}$, and 5.29×10^{15} $W\cdot m^{-1}\cdot K^{-1}\cdot s^{-1}$ at 900 K, 600 K, and 300 K, respectively. For **$CeMgO_3$**, the corresponding values are 8.61×10^{15} $W\cdot m^{-1}\cdot K^{-1}\cdot s^{-1}$, 6.04×10^{15} $W\cdot m^{-1}\cdot K^{-1}\cdot s^{-1}$, and 2.96×10^{15} $W\cdot m^{-1}\cdot K^{-1}\cdot s^{-1}$. The κ_e/τ values increase with rising temperature, which is attributed to the enhancement of electron energy. This behavior reflects the metallic-like conduction trend in the **p**-type region at high temperatures. Moreover, **$CeBeO_3$** exhibits a significantly higher κ_e/τ compared to **$CeMgO_3$**, suggesting stronger electronic heat transport. Such a difference can be linked to variations in the electronic density of states near the Fermi level and the effective mass of charge carriers.

d) Merit Factor

Figures 7d and **8d** reveal that the maximum values of the merit factor (ZT) with respect to chemical potential consistently occur in the **n**-type region across the entire investigated temperature range. The highest ZT value, approximately **1**, is achieved at room temperature for both **$CeBeO_3$** and **$CeMgO_3$** materials. Although the optimal ZT values decrease with increasing temperature, they remain in the n-type region and stay above 0.8. These calculations provide a basis for further optimization of the thermoelectric properties of **$CeBeO_3$** and **$CeMgO_3$** perovskite semiconductors and may also have practical significance for room-temperature thermoelectric applications. This behavior suggests that the electronic structure of these compounds is particularly favorable for **n**-type conduction, which can be attributed to their band dispersion and density of states near the conduction band edge. The persistence of relatively high ZT values at elevated temperatures indicates good thermal stability, which is a critical requirement for reliable thermoelectric devices. Therefore, targeted doping strategies or nanostructuring techniques could further enhance their performance by reducing lattice thermal conductivity without compromising electrical properties.

III.8 Conclusion

Lattice constants of 3.60 Å and 3.85 Å, respectively, have been determined through structural optimization of cubic perovskite-type oxides **$CeBO_3$ (B = Be, Mg)**. The nonmagnetic phase is more stable than the ferromagnetic and antiferromagnetic phases. The thermodynamic stability and potential synthesizability of these perovskites are confirmed by the negative values of cohesive energy and formation enthalpy. With indirect band gaps of 0.73 eV (**$CeBeO_3$**) and

0.51 eV (**$CeMgO_3$**), the results indicate a semiconducting nature. Additionally, these materials exhibit elastic anisotropy: **$CeBeO_3$** behaves primarily in a ductile manner, whereas **$CeMgO_3$** shows a slight degree of brittleness. Their optical response demonstrates significant absorption in the visible to near-infrared spectrum, suggesting potential for energy-conversion and optoelectronic applications. These perovskites exhibit a broad energy range, highlighting their potential for optoelectronic applications and effective absorption of harmful UV radiation. In particular, **$CeMgO_3$** demonstrates exceptional transparency in the near-ultraviolet region, making it a strong candidate for transparent coatings. Both **$CeBeO_3$** and **$CeMgO_3$** show promise for thermoelectric generators, owing to their notably high merit factor values, especially near 300K. This study provides valuable reference data for researchers investigating perovskite oxides.

References

[1] D. Singh, Planes waves, pseudo-potentials and the LAPW method. Kluwer academic publishers, Boston, Dortrecht, London (1994).

[2] M.C. Payne, M.P. Teter, D.C. Allan, T.A. Arias, J.D. Joannopoulos. Iterative minimization techniques for ab-initio total-energy calculations: molecular dynamics and conjugate gradients. Rev Mod Phys 64 (1992) 1045.

[3] P. Blaha, K. Schwarz, G. K. H. Madsen, D. Kvasnicka, J. Luitz, R. Laskowski, F. Tran and L. D. Marks, *WIEN2k*, An Augmented Plane Wave + Local Orbitals Program for Calculating Crystal Properties (Karlheinz Schwarz, Techn. Universität Wien, Austria), 2018. ISBN 3-9501031-1-2.

[4] J.P. Perdew, K. Burke, M. Ernzerhof, Generalized gradient approximation made simple. Phys Rev Lett. 77(18), 3865 (1996).

[5] Z. Wu, R.E. Cohen, More accurate generalized gradient approximation for solids. Phys. Rev. B 73, 235116 (2006).

[6] F.Tran, P. Blaha, Accurate band gaps of semiconductors and insulators with a semilocal exchange-correlation potential. J. Phys. Rev. Lett. 102, 226401 (2009).

[7] M.A. Jamal, Package for Calculating Elastic Tensors of Cubic Phases by Using Second-Order Derivative with WIEN2k Package, 2013.

[8] T.S. Moss, Relations between the refractive index and energy gap of semiconductors, Phys. Status Solidi 131 (2) (1985) 415–427.

[9] S. Adachi, Properties of Semiconductor Alloys: Group-IV, III-V and II-VI Semiconductors (John Wiley & Sons, 2009).

[10] J.M. Hu, S.P. Huang, Z. Xie, H. Hu and W.D. Cheng, First-principles study of the elastic and optical properties of the pseudocubic Si_3As_4, Ge_3As_4 and Sn_3As_4, J. Phys.: Condens. Matter 19 (2007) 496215.

[11] G.K.H. Madsen, D.J. Singh, BoltzTraP. A code for calculating band-structure dependent quantities, Comput. Phys. Commun. 175 (2006) 67-71.

[12] K. Momma and F. Izumi, "VESTA 3 for three-dimensional visualization of crystal, volumetric and morphology data," J. Appl. Crystallogr., 44, 1272-1276 (2011).

[13] C.R. Kagan, D.B. Mitzi, C.D. Dimitrakopoulos, Organic-Inorganic Hybrid Materials as Semiconducting Channels in Thin-Film Field-Effect Transistors, Science 286 (1999) 945-947.

[14] Q. Chen, N. De Marco, Y. Yang, T.-B. Song, C.-C. Chen, H. Zhao, Z. Hong, H. Zhou, Y. Yang, Under the spotlight: The organic–inorganic hybrid halide perovskite for optoelectronic applications, Nano Today 10 (2015) 355-396.

[15] Y. Chen, M. He, J. Peng, Y. Sun, Z. Liang, Structure and growth control of organic–inorganic halide perovskites for optoelectronics: From polycrystalline films to single crystals, Adv. Sci. 3 *(*2016) 1500392.

[16] Q. Mahmood, S.A. Ali, M. Hassan, A. Laref, First principles study of ferromagnetism, optical and thermoelectric behaviours of AVO_3 (A = Ca, Sr, Ba) perovskites, Materials Chemistry and Physics 211 (2018) 428-437.

[17] A.M. Asiri, M.K. Shahzad, S. Hussain, K. Zhu, S.B Khan, K.A. Alamry, S.Y. Alfifi, H.M. Marwani, Analysis of $XGaO_3$ (X = Ba and Cs) cubic based perovskite materials for photocatalytic water splitting applications: a DFT study, Heliyon 9 (2023) e14112.

[18] Asif Mahmood, Shahid M. Ramay, Hafiz Muhammad Rafique, Yousef Al-Zaghayer, and Salah Ud-Din Khan, First-principles study of electronic, optical and thermoelectric properties in cubic perovskite materials $AgMO_3$ (M = V, Nb, Ta), Modern Physics Letters B20 (2014).

[19] J. Hornstra, W. Bartels, Determination of the lattice constant of epitaxial layers of III-V compounds. J. Cryst. Growth 44, (1978) 513–517.

[20] R. Sharma, A. Dey, S. Ahmed Dar, V. Srivastava, A DFT investigation of $CsMgX_3$ (X = Cl, Br) halide perovskites: Electronic, thermoelectric and optical properties, Computational and Theoretical Chemistry 1204 (2021) 113415.
[21] A. Dey, R. Sharma, S.A.Dar, I.H. Wani, Cubic $PbGeO_3$ perovskite oxide: A compound with striking electronic, thermoelectric and optical properties, explored using DFT studies, Computational Condensed Matter 26 (2021) e00532.
[22] R. Yadav, A. Srivastava, J.A. Abraham, R. Sharma, S.A. Dar, First-principles calculations to investigate structural, electronic, thermoelectric, and optical properties of heavy thallium perovskite $TlPbX_3$ (X = Cl, Br, I), Materials Science and Engineering B 283 (2022) 115781.
[23] M. Saeed, A. Ali, I. Ul Haq, S. Muhammad, A.R. Chaudhry, A. ur Rehman, Z. Ali, S. M. Siddeeg, I. Khan, First-principles study of the structural and optoelectronic properties of $ANbO_3$ (A = Na, K and Rb) in four crystal phases, Materials Science in Semiconductor Processing 139 (2022) 106364.
[24] C. Ma, L. Ye, Z. Yang, Electronic structures of perovskite $BaTbO_3$ studied by the LSDA $+U$ method, J. Phys. Condens. Matter 17 (2005) 7963.
[25] S. Rahman, A. Hussain, S. Noreen, N. Bibi, S. Arshad, J.Ur. Rehman, M.B. Tahir, Structural, electronic, optical and mechanical properties of oxide-based perovskite ABO_3 (A = Cu, Nd and B = Sn, Sc): A DFT study, Journal of Solid State Chemistry 317 (2023) 123650.
[26] A. Alin, H. I. Elsaeedyn I. Ul Haq, I. Khan, Ferroelectric, electronic and magnetic properties of Mn_2ScMO_6 (M = Nb, Ta) double corundum oxides via first principles, Applied Physics A (2023) 129:593.
[27] A. Ali, H.I. Elsaeedy, S. Ullah, S. Ali Khan, I. Khan, First-principles study of polar magnets corundum double-oxides Mn_2FeMO_6 (M = W and Mo), Journal of Magnetism and Magnetic Materials 563 (2022) 169942.
[28] A. Ali, I. Khan, Z. Ali, F. Khan, and I. Ahmad, First-principles study of $BiFeO_3$ and $BaTiO_3$ in tetragonal structure, International Journal of Modern Physics B 33 (2019) 1950231.
[29] T. Charpin, A Package for calculating elastic tensors of cubic phase using WIEN (Laboratory of Geometrix, Paris (2001).
[30] S. Wang, H. Ye, First-principles study on elastic properties and phase stability of III–V compounds. Phys. Status Solidi 240, (2003) 45.
[31] M. Born and K. Huang, Dynamics Theory of Crystal Lattices (Oxford University Press, 1954).
[32] M. Moin, A.W. Anwar, · M.A. Ahmad, A. Ali, Mehrunisa, Computational comparative analysis of (Ag, In)-doped $LaAlO_3$ for optoelectronic application: a first- principles study, Journal of Electronic Materials (2023) 52:5738–5753.
[33] A. Cheriet, S. Khenchoul, L. Aissani, B. Lagoun, M. Zaabat, A. Alhussein, First-principles calculations to investigate structural, magnetic, electronic and elastic properties of full-Heusler alloys Co_2MB (M=V, Mn). Solid State Commun. 337, 114426 (2021)
[34] J. Haines, J.M. Leger, G. Bocquillon, Synthesis and Design of Superhard Materials, Annu. Rev. Mater. Res. 31 (2001) 1.
[35] M. A. Hadi, S.R. G. Christopoulos, A. Chroneos, S. H. Naqib & A. K. M. A. Islam, DFT insights into the electronic structure, mechanical behaviour, lattice dynamics and defect processes in the first Sc-based MAX phase Sc_2SnC, Scientific Reports (2022) 12:14037.
[36] S. Sahin, Y.O. Ciftci, K. Colakoglu, N. Korozlu, First principles studies of elastic, electronic and optical properties of chalcopyrite semiconductor $ZnSnP_2$,J. Alloys Compd. 529 (2012) 1-7.

[37] S. Pugh, XCII. Relations between the elastic moduli and the plastic properties of polycrystalline pure metals, the London, Edinburgh, and Dublin philosophical magazine and journal of science, 45 (1954) 823.
[38] B. Sabir, G. Murtaza, R.M. Arif Khalil, Q. Mahmood, First principle study of electronic, mechanical, optical and thermoelectric properties of $CsMO_3$ (M = Ta, Nb) compounds for optoelectronic devices, J. Mol. Graph. Model. 86 (2019) 19–26.
[39] B. Amin, I. Ahmad, M. Maqbool, S. Goumri-Said, and R. Ahmad, Ab initio study of the bandgap engineering of $Al_{1-x}Ga_xN$ for optoelectronic applications, J. Appl. Phys. 109, (2011) 023109.
[40] G. Marius, the Physics of Semiconductors: Kramers-kronig Relations, Springer, Berlin Heidelberg (2010) 775–776.
[41] M. Gajdoš, K.Hummer, G. Kresse, J. Furthmüller, F. Bechstedt, Linear optical properties in the projector-augmented wave methodology. Phys. Rev. B. 73 (2006) 045112.
[42] C. Ambrosch-Draxl, J.O. Sofo, Linear optical properties of solids within the full potential linearized augmented planewave method. Comput. Phys. Commun 175 (2006) 1–14.
[43] M. Irfan, M.A. Kamran, S. Azam, M.W. Iqbal, T. Alharbi, A. Majid, S.B. Omran, R. Khenata, A. Bouhemadou, X. Wang, Electronic structure and optical properties of TaNO: an ab initio study, J. Mol. Graph. Model. 92 (2019) 296–302.
[44] R. D. L. Kronig, on the theory of dispersion of x-rays, J. Opt. Soc. Am. 12, 547–556 (1926).
[45] S. Laghzaoui, A.F. Lamrani, R. Ahl Laamara, E. Maskar, A. Laref, M.Ezzeldien, D.P. Rai, Realization of half-metal antiferromagnetic (HM-AFM) behaviour in double perovskite Sr_2CrReO_6 on substitution of Tc at Cr site: Promising material for optoelectronics and thermoelectric applications via DFT framework, Inorganic Chemistry Communications 146 (2022) 110172.
[46] H. Ehrenreich, H. Philipp, Optical properties of Ag and Cu, Phys. Rev. 128 (1962) 1622.
[47] M.K. Butt, M.Yaseen, J. Iqbal, A.S. Altowyan, A. Murtaza, M. Iqbal and A. Laref, Structural, electronic, half –metallic ferromagnetic and optical properties of cubic $MAlO_3$ (M=Ce, Pr) perovskites: A DFT study, Journal of Physics and Chemistry of Solids 154 (2021) 110084.
[48] M.K. Butt, M. Yaseen, A. Ghaffar, M. Zahid, First principle insight into the structural, optoelectronic, half metallic, and mechanical properties of cubic perovskite $NdInO_3$, Arabian Journal for Science and Engineering 45 (2020) 4967–4974.
[49] D.R. Lawati, H.K. Neupane, D.K. Chaudhary, P. Shrestha, R.P. Adhikari, L.P. Joshi, R. Parajuli, Structural, mechanical, electronic and optical properties of $MgZnO_3$ perovskite: First-principles study, Journal of Physics and Chemistry of Solids 181 (2023) 111547.
[50] K.M. Hossain, S.K. Mitro, M.M. Rahman, A.A. Khatun, F. Parvin, Analyzing the physical properties of perovskite oxides $BaMO_3$ (M = Ru, Os) for predicting potential applications, Computational Condensed Matter 34 (2023) e00782.
[51] D.M. Hoat, J.F. R. Silva, A. M. Blas, First principles study of structural, electronic and optical properties of perovskites $CaZrO_3$ and $CaHfO_3$ in cubic phase, Solid State Communications 275 (2018) 29–34.
[52] M.M. Fadhali, Abu Bakar, S. Ali, A. Afaq, H.H. Hegazy, Effect of pressure on structural, electronic dispersion relations, optical and thermoelectric properties of $CsNbO_3$ perovskite for photovoltaic and energy applications, Polyhedron 230 (2023) 116217.
[53] N.M. Ravindra, P. Ganapathy, J. Choi, Energy gap–refractive index relations in semiconductors, Infrared Phys. Technol. 50 (2007) 21–29.
[54] A.A. Mousa, M.S. Abu-Jafar, D. Dahliah, R.M. Shaltaf, and J.M. Khalifeh, Investigation of the perovskite $KSrX_3$ (X = Cl and F) compounds, examining the optical, elastic,

electronic and structural properties: FP-LAPW study, Journal of electronic materials, 47(1) (2018) 641-650.

[55] A. Ali, H. Elhosiny Ali, I. Khan, Investigations of the structural, magnetic, mechanical, electronic and ferroelectric properties of Mn_2MnWO_6 double corundum oxide, Materials Chemistry and Physics, 296 (2023) 127197.

[56] X. Liu, B. Xie, C. Duan, Z. Wang, B. Fan, K. Zhang, B. Lin, F.J.M. Colberts, W. Ma, R.A.J. Janssen, F. Huang, Y. Cao, A high dielectric constant non-fullerene acceptor for efficient bulk-heterojunction organic solar cells, J. Mater. Chem. A. 6 (2018) 395–403.

[57] A. Mera, G. Nazir, Q. Mahmood, N.A. Kattan, T. Alshahrani, A. Rehman, H. Sultana, Mohammed A. Amin H. Elhosiny Ali, the bandgap engineering of double perovskites Cs_2CuSbX_6 (X = Cl, Br, I) for solar cell and thermoelectric applications, Inorganic Chemistry Communications 148 (2023) 110303.

[58] M. Manzoor, M.W. Iqbal, N.A. Noor, H. Ullah, R.Sharma, S. S. Alarfaji, Exploring the structural, electronic, optical, and thermoelectric properties of potassium-based double perovskites K_2AgXI_6 (X = Sb, Bi) compounds: A DFT study, Materials Science and Engineering B 287 (2023) 116122.

[59] S. Iqbal, G.M. Mustafa, M. Asghar, N.A. Noor, M.W. Iqbal, A. Mahmood, Y-H. Shin, Tuning the optoelectronic and thermoelectric characteristics of narrow bandgap Rb_2AlInX_6 (X= Cl, Br, I) double perovskites: A DFT study, Materials Science in Semiconductor Processing 143 (2022) 106551.

[60] A.A. dewale, A. Chik, T. Adam, O.K. Yusuff, S.A. Ayinde, Y.K. Sanusi, First principles calculations of structural, electronic, mechanical and thermoelectric properties of cubic $ATiO_3$ (A= Be, Mg, Ca, Sr and Ba) perovskite oxide, Computational Condensed Matter 28 (2021) e00562.

[61] K. Yusupov and A.Vomiero, Polymer-based low-temperature thermoelectric composites, Adv. Funct. Mater. 30 (2020) 2002015.

[62] A.Yadav, P.C. Deshmukh, K. Roberts, N.M. Jisrawi and S.R. Valluri, An analytic study of the Wiedemann-Franz law and the thermoelectric figure of merit, Journal of Physics, Communications 3 (10) (2019) 105001.

[63] A. Waqdim, M. Agouri, A. Abbassi, B. Elhadadi, Z. Zidane, S. Taj, B. Manaut, M. Driouich, M. El Idrissi, Theoretical investigation of the physical properties of cubic perovskite oxides $SrXO_3$ (X = Sc, Ge, Si), Materials Science in Semiconductor Processing 158 (2023) 107340.

[64] H.Ohta, thermoelectrics based on strontium titanate, Materialstoday, 10 (10) (2007) 44-49.

[65] H. Absike, N. Baaalla, L. Attou, H. Labrim, B. Hartiti, H. Ez-zahraouy, Theoretical investigations of structural, electronic, optical and thermoelectric properties of oxide halide perovskite $ACoO_3$ (A=Nd, Pr or La), Solid State Communications 345 (2022) 114684.

[66] N. Tahiri, S. Dahbi, I. Dani, O. El Bounagui, H. Ez-Zahraouy, Magnetic, magnetocaloric and thermoelectric investigations of perovskite LaFeO3 compound: First principles and Monte Carlo calculations, Computational and Theoretical Chemistry 1204 (2021) 113421.

[67] M.I. Hussain, R.M.A. Khalil, F. Hussain, A.M. Rana, M. Imran, Ab-initio prediction of the mechanical, magnetic and thermoelectric behaviour of perovskite oxides $XGaO_3$ (X = Sc, Ti, Ag) using LDA+U functional: For optoelectronic devices, Journal of Molecular Graphics and Modelling 99 (2020) 107621.

CHAPTER IV

Double Perovskites K_2BBiBr_6 (B = Cu, Ag)

IV.1 Introduction

The general chemical formula for halide double perovskites (HDPs) is **$A_2BB'X_6$**, where **A** is a large alkali cation (e.g., Cs^+ or K^+), **B** and **B'** are metal cations (e.g., Ag^+, Bi^{3+}, Sc^{3+}, or Cu^{2+}), and **X** is a halide anion (Cl^-, Br^-, or I^-). This class of materials has garnered significant attention for potential applications in optoelectronics, including solar cells, light-emitting diodes (LEDs) **[1-2]**, and photodetectors. The absence of lead in HDPs, particularly in copper- or silver-based compounds **[3-4]**, makes them promising candidates for environmentally friendly technologies. These materials often exhibit wide band gaps, which can be advantageous in optoelectronic applications where low absorption of visible light is desirable. For example, $Cs_2AgBiBr_6$ has been reported as an effective solar material due to its strong light absorption and long carrier lifetime, according to a study by T. McClure et al. **[5]**. However, its solar energy conversion efficiency remains limited by its indirect and wide band gap. O. Oktay et al. **[6]** synthesized $Cs_2AgBiBr_6$ plates using a solvent-free solid-state technique, which produced larger and denser perovskite grains, thereby improving the material's reactivity and detectability.

As a result, $Cs_2AgBiBr_6$ demonstrates promising potential for photodetector applications. In a recent study, W. Shen et al. **[7]** significantly enhanced the performance of a $Cs_2AgBiBr_6$-based photodetector by employing a double electron transport layer (ETL) of SnO_2/ZnO, which improved the specific detectivity by 16.5 times and the responsivity by 12.7 times. The impact of iodine doping on the silver-containing double perovskite $Cs_2AgBiBr_6$ was investigated by B. Akenoun et al. **[8].** They reported that the band gap of $Cs_2AgBiBr_{6-x}I_x$ decreases from 1.841 eV to 1.677 eV as iodine concentration increases, while the absorption coefficient shifts from the ultraviolet to the visible range at 5% iodine substitution. These findings suggest that such materials are stable, non-toxic, and promising absorbers for solar cell applications. Furthermore, a study by S. Al-Qaisi et al. **[9],** based on DFT calculations for K_2CuSbX_6 (X = Cl, Br, I), reported extremely low lattice thermal conductivity and a high figure of merit at 300 K, highlighting the potential of HDPs for renewable energy and thermoelectric generators. Owing to their non-toxicity and diverse properties, several studies over the past three years have explored the elastic, optoelectronic, and thermoelectric characteristics of lead-free double perovskites such as $K_2CuSbBr_6$ **[10]**, $Cs_2SbAgBr_6$ **[11]**, and $Rb_2LiTlBr_6$ **[12]**. Compared to lead-based perovskites, lead-free double perovskites (LFDPs) exhibit superior chemical and thermal stability, ensuring greater reliability in harsh environments. This stability, combined with longer carrier lifetimes and lower non-radiative recombination rates, maximizes device energy efficiency and improves durability under demanding conditions.

In this context, the aim of the present study is to gain deeper insight into the physical properties of HDPs $K_2(Cu/Ag)BiBr_6$ to evaluate their potential for thermoelectric and optoelectronic applications. First, we assess their structural and elastic properties to confirm stability. Then, we analyze their electronic properties relevant to optical behavior, evaluated using the absorption coefficient, refractive index, and reflectivity. Finally, we investigate their thermoelectric properties, focusing on the Seebeck coefficient (S) and power factor (PF). The study concludes with a concise summary of the main findings. In general, perovskite materials can be classified into two categories simple perovskites and complex perovskites each with distinct structural and functional characteristics. The computational methodology adopted in this work has been described in detail in **Chapter III**. Therefore, this section is limited to presenting the obtained results along with their analysis and discussion.

IV.2 Structural properties

$K_2AgBiBr_6$ is reported to be stable in a cubic structure with space group Fm-3m (#225), according to a recent experimental study by S. Janaki et al. **[13]**. In this work, we verify this result by performing a detailed structural optimization for the nonmagnetic (NM), ferromagnetic (FM), and antiferromagnetic (AFM) phases. For these compounds, the atomic positions are as follows : Potassium at (0.25, 0.25, 0.25), Silver (or Copper) at (0, 0, 0), Bismuth at (0.5, 0.5, 0.5), and Bromine at (x, 0, 0), with x = 0.250 **[14]**. As illustrated in **Fig. IV.1**, which shows the unit cell structure of $K_2(Cu/Ag)BiBr_6$ compounds plotted using VESTA 4.5 software **[15]**, the bromine anions octahedrally coordinate the copper (or silver) and bismuth cations.

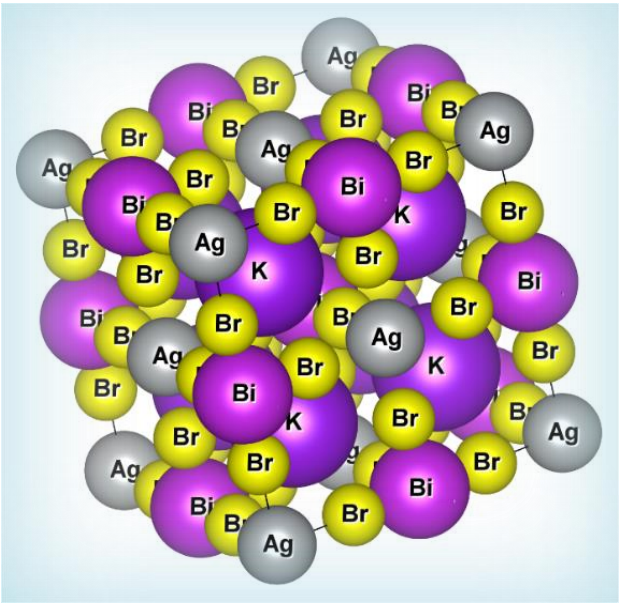

Figure IV. 1: Cubic structure of $K_2CuBiBr_6$ and $K_2AgBiBr_6$ double Perovskites

Each copper (or silver) cation is surrounded by six bismuth cations as its nearest neighbors, while each potassium cation is bonded to twelve bromine anions. This structural arrangement indicates a highly symmetric coordination environment that contributes to the overall stability of these compounds. Furthermore, the cubic symmetry minimizes structural distortions and ensures isotropic physical properties, which is advantageous for optoelectronic applications. **Table IV.1** summarizes the bulk modulus, its pressure derivative, the equilibrium lattice constant, and the ground-state energies for the NM, FM, and AFM configurations. The calculated lattice parameters, 11.90 Å for $K_2CuBiBr_6$ and 11.97 Å for $K_2AgBiBr_6$, are consistent with those reported for other halide double-perovskite semiconductors, such as $K_2RbTlBr_6$ (12.01 Å) **[16]**, $Cs_2CuAsBr_6$ (11.80 Å) **[17]**, and Rb_2KTlBr_6 (11.72 Å) **[18]**. This agreement confirms the reliability of our computational approach and validates the predicted structural stability of these compounds.

Using equations **(IV.1)** and **(IV.2)** **[19]**, we analyze the formation energies ($\Delta \boldsymbol{H_f}$) and cohesive energies ($\boldsymbol{E_{coh}}$) of K_2(Cu/Ag)$BiBr_6$ compounds to ascertain their chemical and structural stability.

$$\boldsymbol{E_{for} = E^{tot}_{K_2Cu(Ag)BiBr_6} - \left(2E^{bulk}_{K} + E^{bulk}_{Cu/Ag} + E^{bulk}_{Bi} + 6E^{bulk}_{Br}\right)} \qquad \textbf{(IV. 1)}$$

$$\boldsymbol{E_{Coh} = E^{tot}_{K_2Cu(Ag)BiBr_6} - \left(2E^{iso}_{K} + E^{iso}_{Cu/Ag} + E^{iso}_{Bi} + 6E^{iso}_{Br}\right)} \qquad \textbf{(IV. 2)}$$

Here, $\mathbf{E^{bulk}}$ indicates the total energy of the primitive cell, $\mathbf{E^{iso}}$ is the energy of the isolated atom, The thermochemical energy required to form K_2(Cu/Ag)$BiBr_6$ from its constituent elements K, (Cu/Ag), Bi, and Br under standard conditions is specified by the negative formation enthalpy ($\Delta \boldsymbol{H_f}$) values found for both compounds. The cohesive energy ($\boldsymbol{E_{coh}}$), which quantifies the energy needed to separate an alloy into its constituent atoms, also indicates how strongly the atoms are held together by chemical bonds. The observed negative values for ($\boldsymbol{E_{coh}}$) confirm the structural stability of all the examined alloys in their optimized states. The stability of the material is assessed using the Goldschmidt factor $\boldsymbol{t_G}$ **(eq. IV.3)**, which measures ion compatibility within perovskite structures. This component indicates whether the network's geometry is stable and whether the cations are positioned correctly in the structure. Depending on their ionic radius and the ionic radius of the position they may occupy, it explains how ions are preferentially incorporated into crystal structures.

$$\boldsymbol{t_G = \frac{r_K + r_{Br}}{\sqrt{2}\left[\left(\frac{r_{Cu(or\ Ag)} + r_{Bi}}{2}\right) + r_{Br}\right]}} \qquad \textbf{(IV. 3)}$$

Generally, a stable structure is expected to have a Goldschmidt factor in the range of 0.8 to 1. Non-perovskite structures are generally observed when t_G is either greater than 1 or less than 0.71 **[20]**.

Table IV.1 Calculated structural equilibrium lattice constant a(Å), pressure derivatives B', ground state energies E_{min} (Ry), formation energy ΔH_f (Ry), cohesive energy E_C (Ry), gap energy E_g(eV) and tolerance factor t_G of $K_2CuBiBr_6$ and $K_2AgBiBr_6$ double Perovskites.

Compounds	*State*	*a*	*B'*	E_{min}	ΔH_f	E_C	E_g	t_G
$K_2CuBiBr_6$	**NM**	**11.90**	**4.02**	**-80162.021508**	**-1.14**	**-1.92**	**0.74 (GGA-PBE) 1.73 (mBJ-GGA)**	**0.89**
	FM	11.89	4.01	-80162.021504	---	---		
	AFM	**11.90**	**4.91**	-80162.021493	----	---		
$K_2AgBiBr_6$	**NM**	**11.97**	**5.50**	**-87486.645199**	**-1.92**	**-1.45**	**1.39 (GGA) 2.82 (mBJ-GGA)**	**0.83**
	FM	11.97	5.54	-87486.645195	----	----		
	AFM	**11.96**	**5.11**	-87486.645186	----	----		

IV.3 Electronic properties

The electronic characteristics of the cubic halide double perovskites K_2(Cu/Ag)$BiBr_6$, as defined by their band structure and total and partial density of states (TDOS and PDOS), are examined in the section that follows. We are able to categorize our compounds as metallic, semiconducting, or insulating thanks to this investigation. Finding possible real-world uses is also aided by knowing the bandgap size and the kind of interband transitions (direct or indirect). The valence band maximum (VBM) and conduction band minimum (CBM) of the two double perovskites investigated in this study are located at the L and X points, respectively, as illustrated in **Figure IV.2**. It can be observed that the conduction band minimum shifts, and the band gap energy increases as the ionic radius increases $(R_{Ag} > R_{Cu})$. This trend has also been reported for several other double perovskite compounds, such as $K_2NaGaBr_6$ and $K_2RbTlBr_6$ **[16]**, as well as $Cs_2CuAsBr_6$ **[17]**. Our compounds, which exhibit indirect band gaps ranging from 1.73 to 2.82 eV, are highly versatile and hold great potential for various optoelectronic and electronic applications. These materials can influence conductivity and the color of emitted

or absorbed light. Furthermore, under sunlight exposure, they may act as photocatalysts, facilitating hydrogen generation or pollutant degradation **[21–22].** The observed increase in band gap with larger ionic radius can be attributed to the lattice expansion, which reduces orbital overlap and results in a wider energy separation between the valence and conduction bands. Such behavior is critical for tuning the optical absorption edge, enabling the design of materials suitable for photovoltaic cells or UV filtering devices. Additionally, these compounds maintain structural stability under ambient conditions, which further enhances their technological relevance.

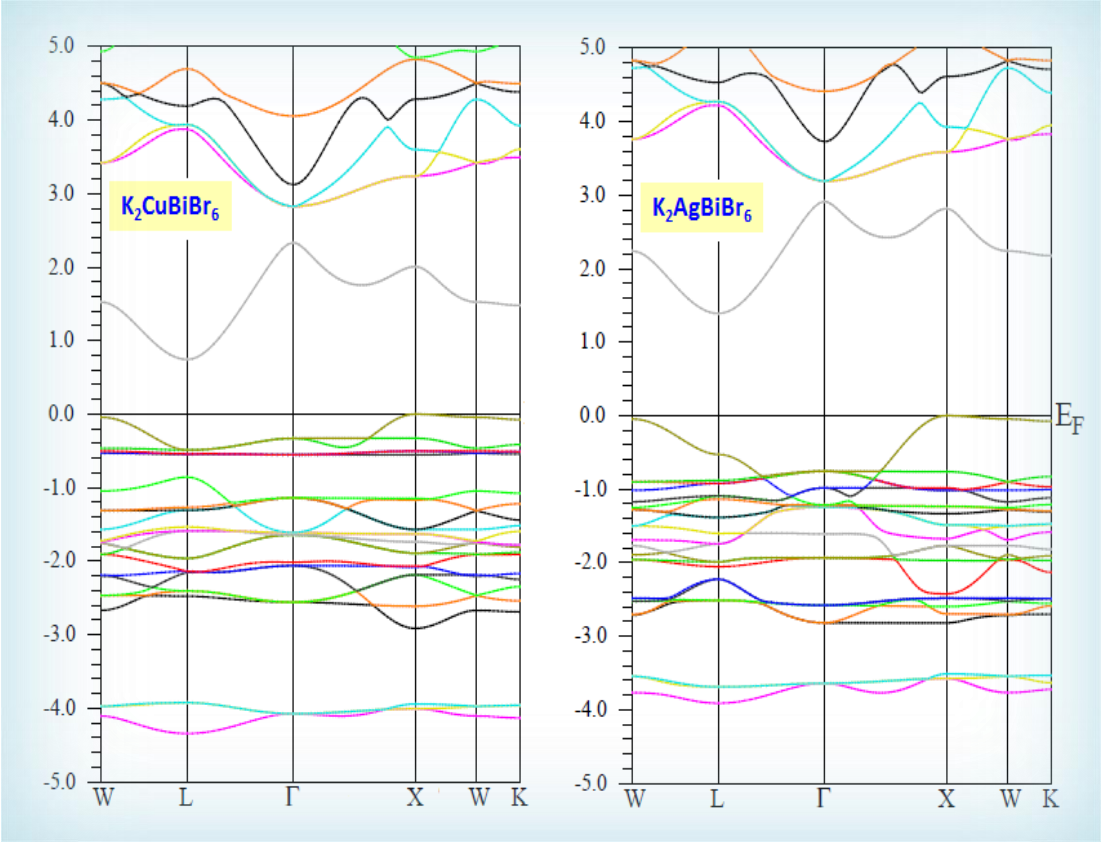

Figure IV. 2: Band structure of $K_2CuBiBr_6$ and $K_2AgBiBr_6$ double Perovskites

In summary, since electronic transitions require both photon absorption and phonon assistance, materials with indirect band gaps exhibit lower absorption coefficients compared to direct band gap materials. Despite their limitations in light absorption, they offer advantages such as enhanced durability and longer charge carrier lifetimes, making them promising candidates for stable and environmentally friendly optoelectronic devices when appropriately engineered. **Figures IV.3** and **IV.4** show the total (TDOS) and partial (PDOS) densities of states for the K_2CuBBr_6 (B = Cu, Ag) double perovskites, calculated using the TB-mBJ method within an

energy range from −6 to 6 eV. These results confirm the semiconducting nature of the compounds, as indicated by the presence of an energy gap around the Fermi level in the TDOS. The main contribution to the valence band comes from the Cu-d states in $K_2CuBiBr_6$ and the Ag-d states in $K_2AgBiBr_6$, whereas the conduction band is dominated by Bi-p states in both compounds, with minor contributions from the Cu-s and Ag-s states, respectively. The Fermi level lies closer to the top of the valence band than to the bottom of the conduction band, indicating a **p**-type semiconducting behavior. The conduction band is mainly composed of **p** and **s** states, while the valence band exhibits a strong contribution from d states.

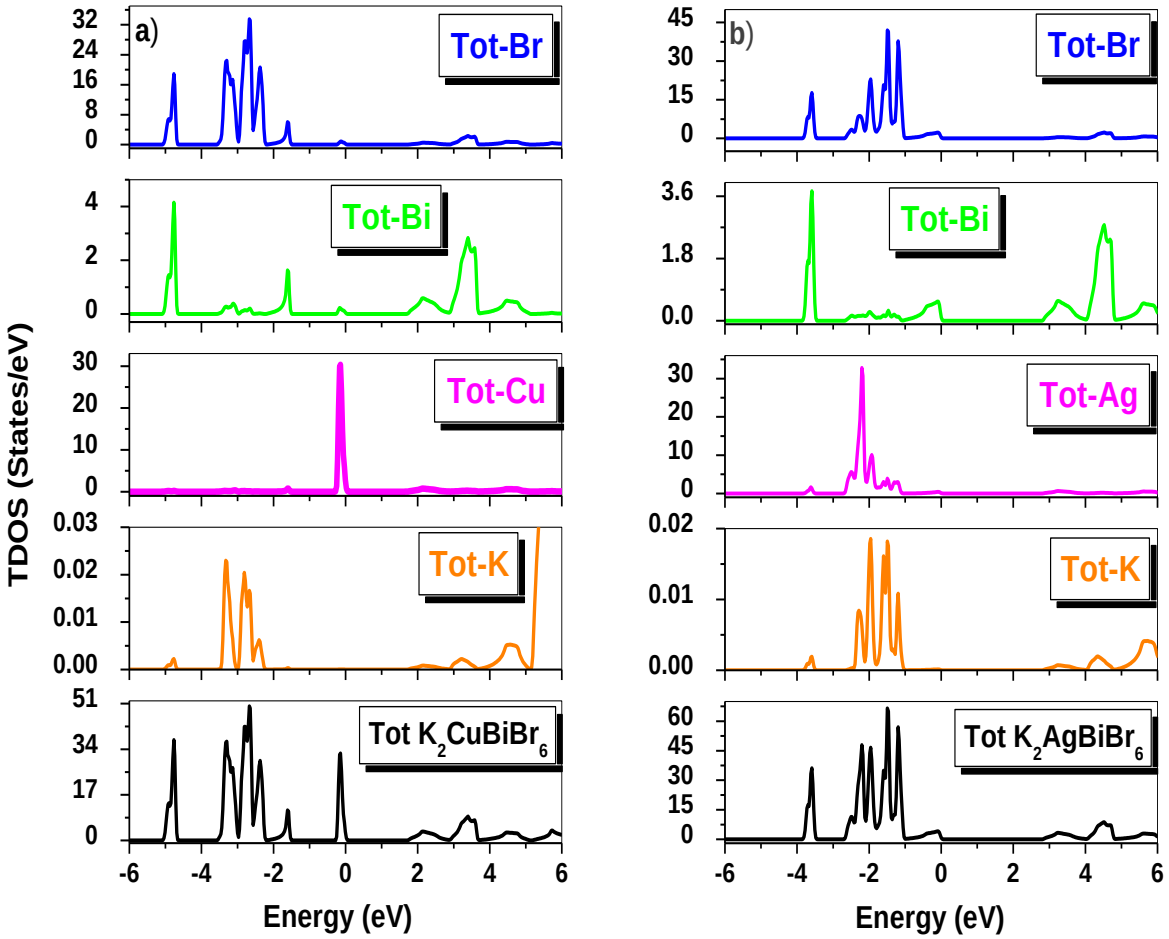

Figure IV. 3: Total density of states (TDOS) of $K_2CuBiBr_6$ and $K_2AgBiBr_6$ double Perovskites

As shown in **Figure IV.4a**, a significant hybridization occurs between Br-d and Bi-s states around −1.58 eV, playing a key role in the formation of the electronic bands in this energy region. This hybridization reflects a strong chemical interaction between Br anions and Bi cations, enhancing the electronic stability of the lattice.

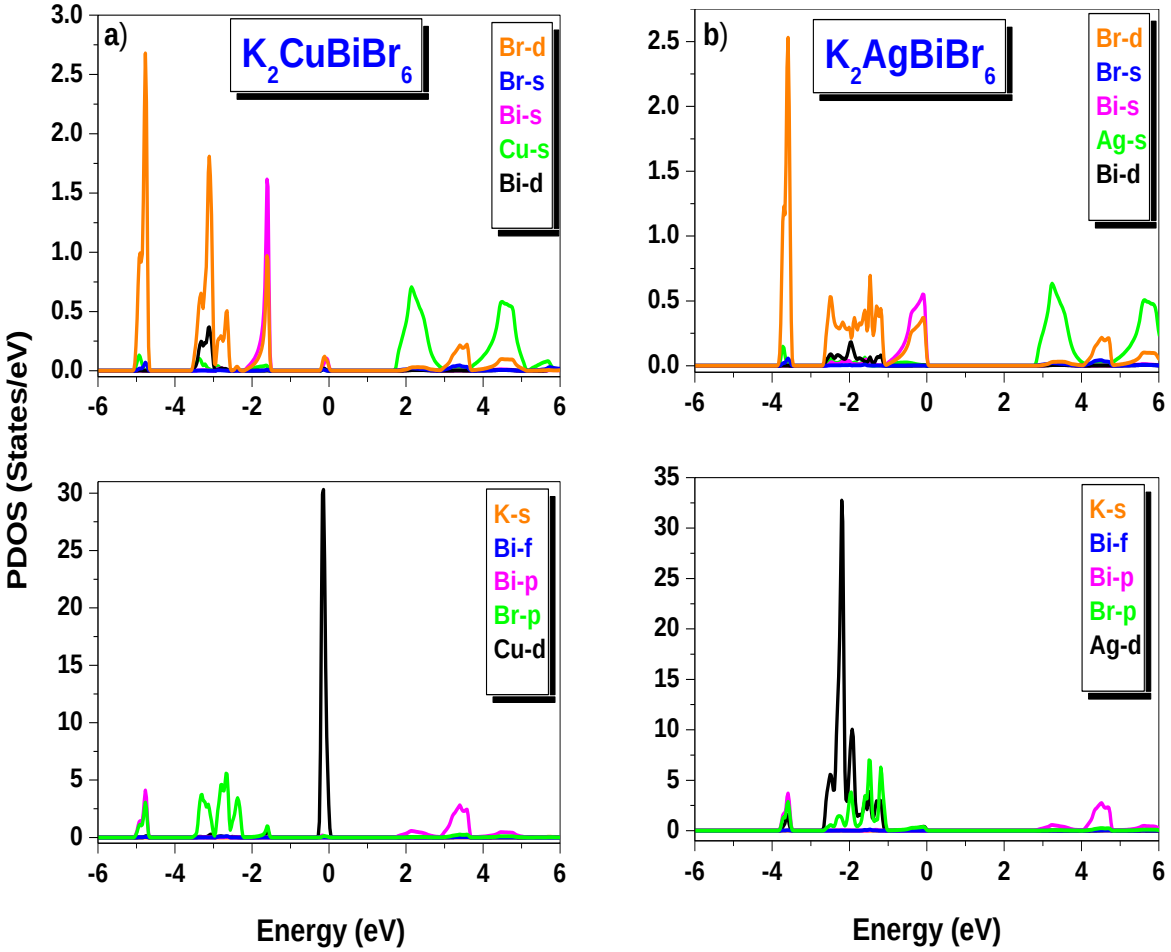

Figure IV.4: Partial density of states (PDOS) of $K_2CuBiBr_6$ and $K_2AgBiBr_6$ double Perovskites

Furthermore, possible electronic transitions include those from Cu-s and Bi-p states in the conduction band to Cu-d and Bi-s states near the Fermi level in $K_2CuBiBr_6$, as well as from Ag-s and Bi-p states to Ag-d and Bi-s states in $K_2AgBiBr_6$. These transitions are particularly important for improving optical properties, especially within the visible range, which could promote potential applications in optoelectronics and photovoltaics. Finally, the asymmetric distribution of d and p states in the valence and conduction bands suggests the possibility of strong optical absorption in the near-ultraviolet and visible regions, along with electronic mobility influenced by the dominant p states in the conduction band. This electronic configuration, combined with the moderate band gap predicted by the TB-mBJ method, confirms that these materials are promising candidates for stable, environmentally friendly, and lead-free optoelectronic devices.

IV.4 Elastic properties

It should be noted that the theoretical background and computational details of the elastic stability criteria, including the Born conditions and the derivation of the associated moduli, were already discussed in **Chapter III**. Therefore, in this section, we focus only on presenting and analyzing the obtained results for $K_2(Cu/Ag)BiBr_6$. The Born criteria, which determine whether atoms remain stable under minor deformations, were used to evaluate the mechanical stability of $K_2(Cu/Ag)BiBr_6$ double perovskites. The elasticity of the material is directly related to these criteria, which are expressed in terms of the elastic constants $\mathbf{C_{11}}$, $\mathbf{C_{12}}$, and $\mathbf{C_{44}}$ **[23].** Other significant elastic parameters, including the bulk modulus (**B**), shear modulus **(G)**, Young's modulus **(E)**, Poisson's ratio **(v)**, and elastic anisotropy factor **(A)**, can be calculated using these constants **[24]**.

According to **Table IV.2**, which provides the independent elastic constants, we can infer that, at zero pressure, the $K_2(Cu/Ag)BiBr_6$ double perovskites are mechanically stable as they meet all of Born's elastic stability criteria **[25]** $\mathbf{(C_{11} - C_{12} > 0)}$; $\mathbf{(C_{11} + 2C_{12} > 0)}$; $\mathbf{(C_{11} > 0)}$; $\mathbf{(C_{44} > 0)}$ and $\mathbf{(C_{12} < B < C_{11})}$. The $K_2CuBiBr_6$ compound meets the condition $\mathbf{C_{11} > C_{22} > C_{33}}$, indicating it is more resistant to unidirectional compression than to shear deformation. However, the $K_2AgBiBr_6$ compound does not satisfy this condition, which suggests that its rigidity varies in different directions and could have implications for its practical applications and performance under various loads. The two compounds exhibit a moderate bulk modulus (B) of around 13 GPa, indicating comparable resistance to compression.

Table IV.2 The computed elastic constants (Cij) in GPa, bulk modulus (B), Shear modulus (G), Young's modulus (E), Poisson's ratio (ν), anisotropic factor (A), and Pugh's ratio (B/G) of $K_2CuBiBr_6$, and $K_2AgBiBr_6$ double Perovskites.

Compounds	C_{11}	C_{12}	C_{44}	$B(GPa)$	$G(GPa)$	$E(GPa)$	ν	A	B/G
$K_2CuBiBr_6$	25.58	7.48	1.91	13.51	4.76	12.77	0.34	0.21	2.83
$K_2AgBiBr_6$	34.85	3.12	7.78	13.69	11.01	26.04	0.18	0.49	1.24

This similarity suggests that the crystalline structures and interatomic interactions of the two materials are comparatively alike, allowing them to exhibit consistent compressibility under high pressure. Moreover, the higher shear modulus (G) of $K_2AgBiBr_6$ compared to $K_2CuBiBr_6$ indicates greater resistance to shear deformation. Our calculations further reveal that

$K_2AgBiBr_6$ has a Young's modulus of 26.04 GPa, which is more than twice that of $K_2CuBiBr_6$ (12.77 GPa), confirming its superior mechanical rigidity. This suggests that under applied stress, the compound $K_2AgBiBr_6$ resists deformation. With a Poisson's ratio (v) of 0.18 for $K_2AgBiBr_6$, the material exhibits ionic bonds and deforms less transversely than longitudinally. On the other hand, the higher value of 0.34 for $K_2CuBiBr_6$ signifies a higher degree of transverse deformation and the presence of covalent and metallic bonding **[26]**. The $K_2CuBiBr_6$ and $K_2AgBiBr_6$ compounds exhibit an anisotropy coefficient (A) that deviates from unity, indicating their anisotropic mechanical properties. However, the low degree of anisotropy for $K_2AgBiBr_6$ suggests a minimal risk of microcracking compared to $K_2CuBiBr_6$, which exhibits a higher value of A. According to Pugh's criterion **[27]**, a material exhibits brittle behavior when the B/G ratio is less than 1.75, as observed for the compound $K_2AgBiBr_6$. Conversely, a B/G ratio greater than 1.75, as in the case of the compound $K_2CuBiBr_6$, indicates ductile behavior.

IV.5 Optical properties

The theoretical framework and formalism for evaluating optical properties, including the derivation of the dielectric function and related expressions, were presented in **Chapter III** (**Equations III.10 to III.17**). Building on this foundation, the present chapter applies these formulations within the TB-mBJ approach to investigate the optical response of the double perovskites $K_2CuBiBr_6$ and $K_2AgBiBr_6$. The optical response of these semiconductors is primarily governed by inter-band transitions between occupied and unoccupied states, which are captured by the imaginary part of the dielectric function, $\boldsymbol{\varepsilon_2(\omega)}$, while the real part, $\boldsymbol{\varepsilon_1(\omega)}$, represents the electronic polarization response.

a) Dielectric function

The dielectric function $\boldsymbol{\varepsilon(\omega)}$ is essential for describing a material's optical properties and its response to an external electromagnetic field. **Figure IV.5a** shows the progress of the real part $\boldsymbol{\varepsilon_1(\omega)}$ across an incident energy spectrum from 0 to 8 eV. The real part $\boldsymbol{\varepsilon_1(\omega)}$ mainly represents the material's degree of polarization, which is derived from the Kramers-Kronig transformation **[28]**. The static dielectric constant, $\boldsymbol{\varepsilon_1(\omega)}$, is distinctly observed in $K_2CuBiBr_6$ and $K_2AgBiBr_6$, with respective values of 4.84 and 4.17. It is noted that $\boldsymbol{\varepsilon_1(\omega)}$ increases with photon energy, reaching peaks associated with optical transitions at energies of approximately 1.27 eV (infrared) and 1.94 eV (visible) for $K_2CuBiBr_6$ and $K_2AgBiBr_6$, respectively. At energy levels higher than those of the maxima, $\boldsymbol{\varepsilon_1(\omega)}$ exhibits a series of fluctuations, characterized by peaks of lower intensity. In the energy range examined in these graphs, the $\boldsymbol{\varepsilon_1(\omega)}$ values remain positive, indicating that photons are not reflected by the two double

perovskites. The substitution of copper, with an electronic configuration of [Ar] $3d^{10}$ $4s^1$, by silver, which has an electronic configuration of [Kr] $4d^{10}$ $5s^1$, leads to a decrease in $\boldsymbol{\varepsilon_1(\omega)}$.

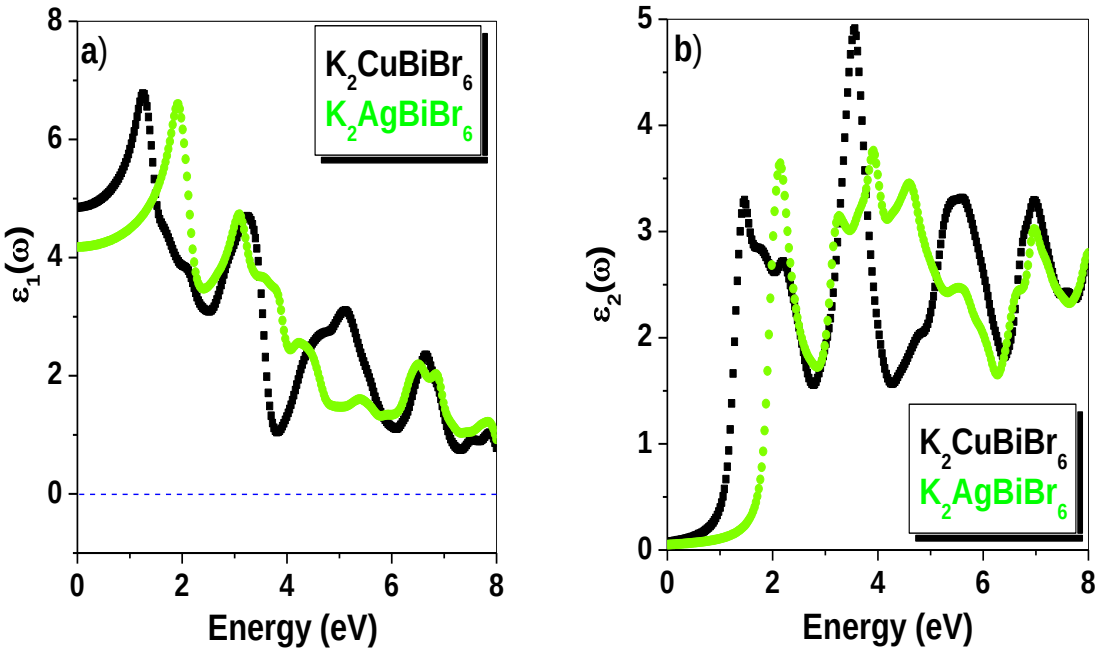

Figure IV.5 Illustration of **a)** real part $\varepsilon_1(\omega)$ and **b)** imaginary part $\varepsilon_2(\omega)$ component of dielectric function of $K_2CuBiBr_6$, and $K_2AgBiBr_6$ double Perovskites

The differences in energy levels and electronic interactions alter th movement of electrons within the material, thereby influencing the dielectric function. As illustrated in **Figure IV.5b**, $\boldsymbol{\varepsilon_2(\omega)}$, which describes the absorption of photon energy in the $K_2CuBiBr_6$ and $K_2AgBiBr_6$ double perovskites, shows a series of peaks, with the maximum peaks observed in the infrared region. The peaks originate from electron transitions between the occupied Cu-d and Bi-s states, located in the highest valence band, and the unoccupied Cu-s and Bi-p states, found in the lowest conduction band. For both compounds, $\boldsymbol{\varepsilon_2(\omega)}$ exhibits a non-zero value for energies below the band gap. This can be attributed to transitions between energy levels within the valence band or to electronic excitations associated with localized states**.** The maximum value of the real component of the dielectric function for the $K_2CuBiBr_6$ compound is found in the infrared region (1.27 eV), while that of the imaginary part appears in the ultraviolet region (3.55 eV). In contrast, for the $K_2AgBiBr_6$ compound, the maximum value of the real component is located in the visible region (1.91 eV), and that of the imaginary part in the infrared region (3.91 eV). The two double perovskites examined in this study exhibit remarkable optical absorption across a wide range of electromagnetic frequencies, thereby promoting the expansion of polarized electrons into conductive states and enhancing photovoltaic conversion efficiency.

The profiles of $\boldsymbol{\varepsilon_1(\omega)}$ and $\boldsymbol{\varepsilon_2(\omega)}$ obtained resemble those observed in halide double perovskites such as Ba_2InNbO_6 **[29]** and $K_2ScAgBr_6$ **[30]**.

b) Absorption coefficient

To assess the suitability of a semiconductor for a photocatalytic application, it is essential to calculate its absorption coefficient $\boldsymbol{\alpha(\omega)}$. As shown in **Figure IV.6a**, all observed peaks of $\boldsymbol{\alpha(\omega)}$ originate from the baseline, showing no photon absorption when there is no light, especially for zero incident photon energy. The ions Cu^+ and Ag^+ modify the optical properties by disturbing the electronic bands and energy levels. In $K_2CuBiBr_6$, Cu^+ strongly interacts with Br^-, shifting the optical gap and altering the absorption response. In contrast, the Ag^+ ion, due to its size and electronic configuration, causes more subtle changes, slightly affecting the optical transitions in $K_2AgBiBr_6$. The two double perovskites exhibit a comparable absorption rate in the visible range, approximately 17×10^4 cm^{-1}. However, in the ultraviolet range, $K_2CuBiBr_6$ shows slightly higher $\boldsymbol{\alpha(\omega)}$ values compared to the $K_2AgBiBr_6$ compound. The maximum absorption coefficients, $\boldsymbol{\alpha(\omega)}$, for $K_2CuBiBr_6$ and $K_2AgBiBr_6$ are significant, achieving values of 78×10^4 cm^{-1} and 69×10^4 cm^{-1}, respectively, at an energy of 7.10 eV.

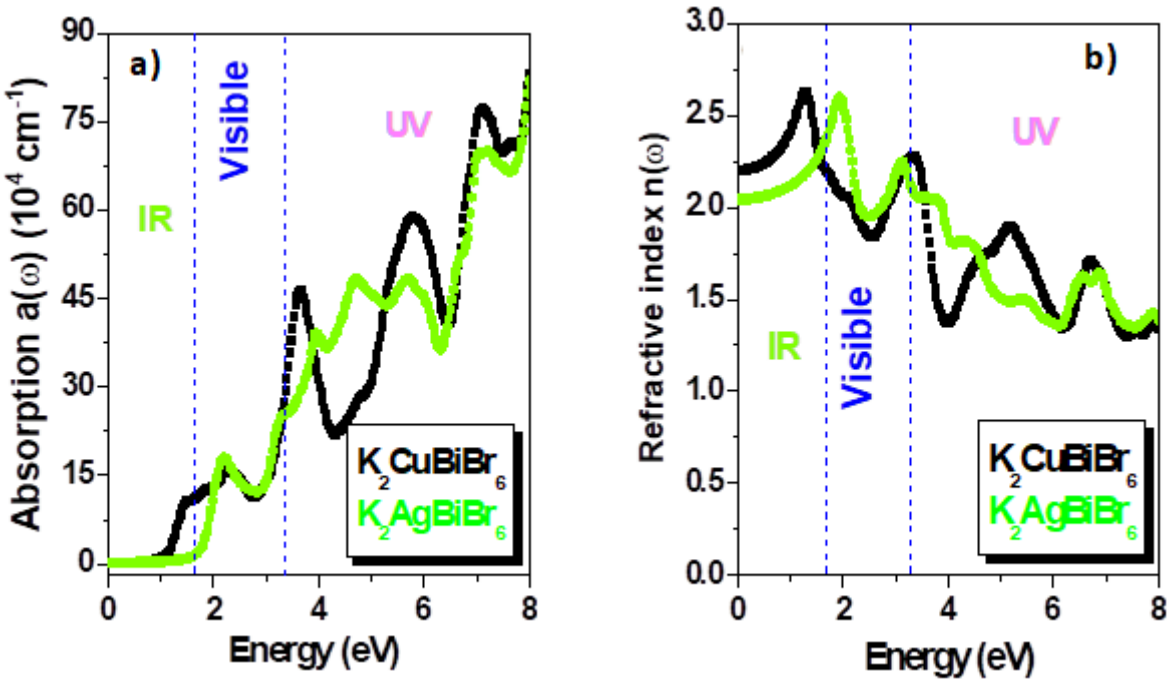

Figure IV.6 Illustration **a)** absorption coefficient a(ω) and b) refractive index n(ω) of $K_2CuBiBr_6$, and $K_2AgBiBr_6$ double Perovskites

The absorption spectra of $K_2CuBiBr_6$ and $K_2AgBiBr_6$ cover a broad range of energies, indicating their ability to absorb frequencies throughout the spectrum, especially in the visible

and ultraviolet regions. Conversely, their absorption in the infrared range is minimal. A high absorption coefficient in the visible spectrum increases photon-to-electron conversion, thus optimizing cell efficiency. The absorption rate of the compounds we investigated exceeds the values reported for several halide double perovskites, including $Li_2AgBiCl_6$, $Li_2AgBiBr_6$ **[31]**, Rb_2YCuCl_6 **[32]**, and $K_2AgSbBr_6$ **[33]**.

c) Refractive index

The propagation of photons through different optical media is governed by the refractive index $\mathbf{n(\omega)}$ **[34].** At 0 eV, the compound $K_2CuBiBr_6$ has a value of 2.20, while the compound $K_2AgBiBr_6$ has a value of 2.05, as shown in **Figure IV.6b**. These slightly higher values indicate that these materials significantly refract light. Substituting the copper atom with a silver atom shifts the main peak of $\mathbf{n(\omega)}$ from the infrared region to the visible region. Of the two double perovskites studied, $K_2CuBiBr_6$ exhibits a slightly higher $\mathbf{n(\omega)}$ than $K_2AgBiBr_6$, indicating that the incident photons interact with a greater number of valence electrons. This interaction leads to increased polarization and a reduction in the speed of light. The highest refractive index values 2.64 for $K_2CuBiBr_6$ and 2.61 for $K_2AgBiBr_6$ make these materials well-suited for use in light-emitting diodes (LEDs) and solar cells **[35]**. The refractive index follows a model similar to that of the real part of the dielectric function $\boldsymbol{\varepsilon_1(0) = n^2(0)}$ **[36]**, indicating that the optical properties of these materials are strongly correlated with their electronic properties.

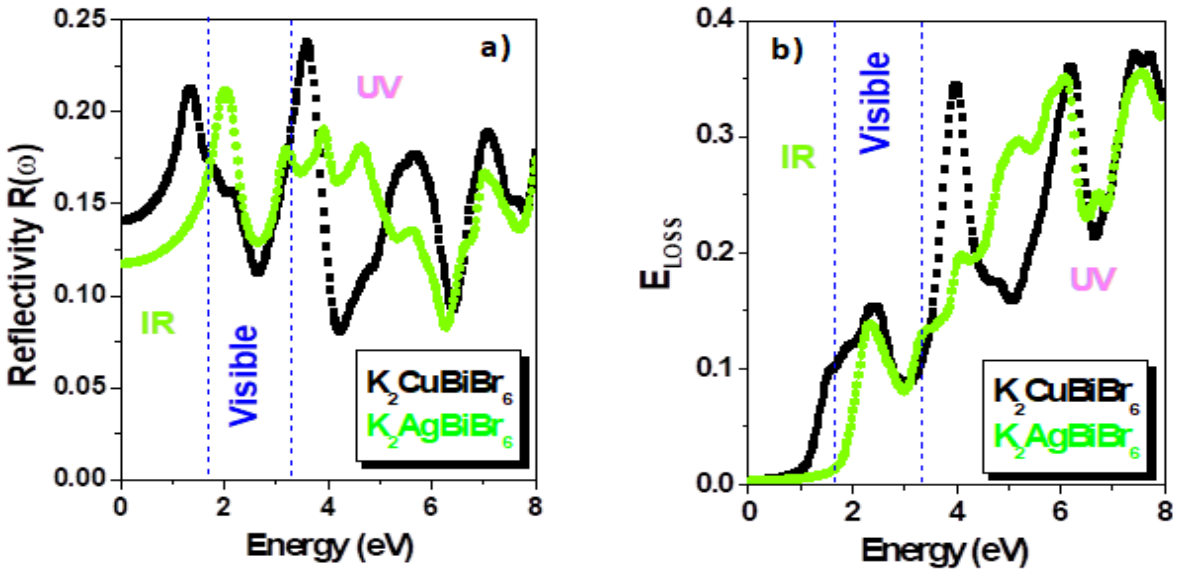

Figure IV.7 Illustration of a**)** reflectivity R(ω), and b) electron energy loss L(ω) of $K_2CuBiBr_6$, and $K_2AgBiBr_6$ double Perovskites

d) Reflectivity

Figure IV.7a shows how reflectivity $\mathbf{R}(\boldsymbol{\omega})$ changes with phonon energy, where reflectivity is defined as the ratio of the intensity of radiation reflected by a surface to the intensity of the incident radiation. One can observe that the static values of $\mathbf{R}(\boldsymbol{\omega})$ are 14% for $K_2CuBiBr_6$ and 11.5% for $K_2AgBiBr_6$, respectively.

The $K_2CuBiBr_6$ alloy shows its highest value of 24% in the ultraviolet range, while the $K_2AgBiBr_6$ alloy reaches its peak value of 21% in the visible range. With reflectivity around 20% across a broad spectrum, our two double perovskites can be used in solar panels to optimize absorption while minimizing unwanted reflections and they can also be utilized in optics for anti-reflective coatings [37]. Low reflectivity allows for greater light capture, reducing reflection losses and maximizing the absorption of incident light.

e) Energy loss function

Figure IV.7b shows the variation of the energy loss function $\boldsymbol{L}(\boldsymbol{\omega})$ with photon energy for $K_2CuBiBr_6$ and $K_2AgBiBr_6$ compounds. In the visible range, $\boldsymbol{L}(\boldsymbol{\omega})$ is less than 0.16 for $K_2CuBiBr_6$ and 0.14 for $K_2AgBiBr_6$. Both double perovskites exhibit a significant increase in $\boldsymbol{L}(\boldsymbol{\omega})$ in the ultraviolet (UV) range. $K_2CuBiBr_6$ features three distinct peaks in the UV region at 4.00 eV, 6.20 eV, and 7.50 eV, with peak intensities of 0.35, 0.36, and 0.37, respectively. In contrast, $K_2AgBiBr_6$ shows its main peaks at 6.06 eV and 7.62 eV, with peak intensities around 0.35. The highest $\boldsymbol{L}(\boldsymbol{\omega})$ values are linked to decreases in $\boldsymbol{\varepsilon_1}(\boldsymbol{\omega})$. These energy losses are attributed to electronic excitations and the movement of fast electrons through the material. As a conclusion to this optical study, it can be said that with a band gap of 1.73 eV for $K_2CuBiBr_6$ and 2.82 eV for $K_2AgBiBr_6$, these compounds exhibit great versatility and are applicable in various fields. They can be used for producing LEDs that cover a broad color spectrum, from red for $K_2CuBiBr_6$ to blue/violet for $K_2AgBiBr_6$, providing vibrant lighting and displays. Additionally, $K_2CuBiBr_6$ is suitable for detecting wavelengths ranging from red to near-infrared, while $K_2AgBiBr_6$ is effective for detecting shorter wavelengths, from blue to ultraviolet. In solar cell technologies, the band gap of $K_2CuBiBr_6$ is well-suited for standard applications, whereas the band gap of $K_2AgBiBr_6$ is ideal for specialized, high-efficiency photovoltaic applications.

IV.6 Thermoelectric properties

The thermoelectric properties of $K_2(Cu/Ag)BiBr_6$ double perovskites are analyzed within the framework of semi-classical Boltzmann transport theory. The governing relations for key parameters, including the Seebeck coefficient, electrical and thermal conductivity, and the

thermoelectric figure of merit (ZT), were presented in **Chapter III (Equations III.18–III.21)**. This section emphasizes the computed results and their implications for the thermoelectric performance of the investigated compounds.

a) Seebeck coefficient

For a temperature range of 100 to 900 K, **Figure IV.8a** shows the variation of the Seebeck coefficient (**S**), which expresses the potential difference as a function of the temperature gradient. The value of **S** for both compounds exhibits an inverse relationship with electrical conductivity and decreases with increasing temperature. This can be explained by the thermal excitation of charge carriers, which increases electrical conductivity but lowers thermoelectric voltage because of the increased carrier concentration.

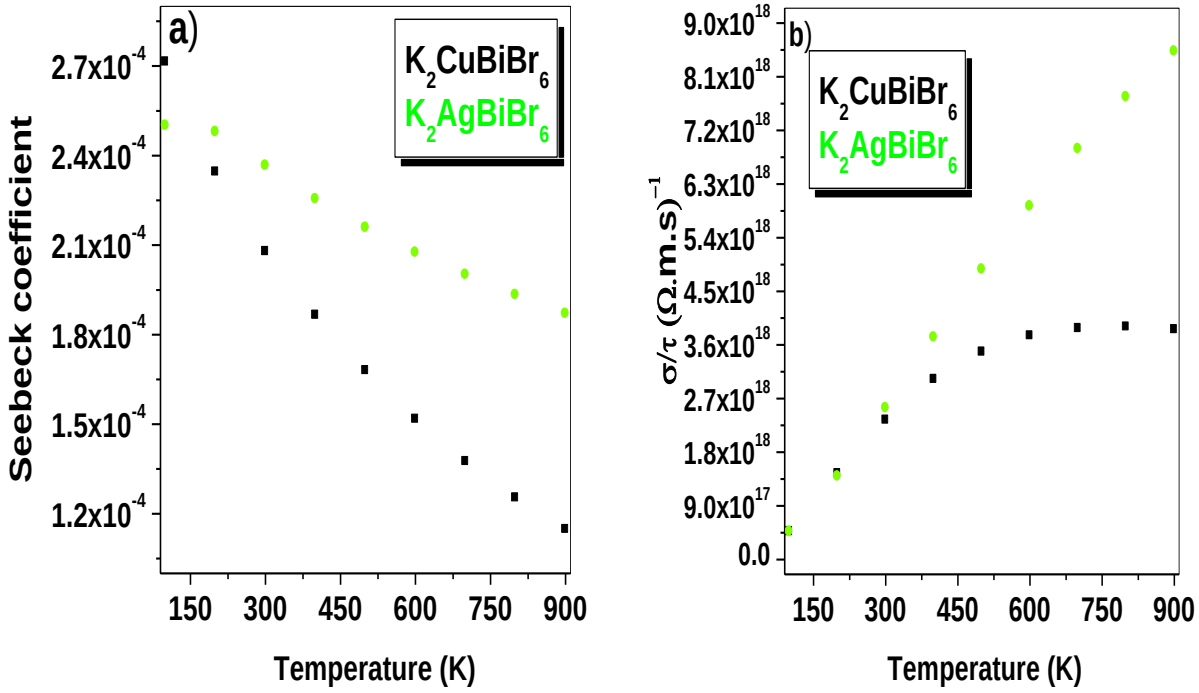

Figure IV.8 (a) Seebeck coefficient (S) and (b) Electrical conductivity (σ/τ), of $K_2CuBiBr_6$, and $K_2AgBiBr_6$ double Perovskites

The maximum values of S observed were $2.72 \times 10^{-4}\ V/K$ for $K_2CuBiBr_6$ and $2.52 \times 10^{-4}\ V/K$ for $K_2AgBiBr_6$, respectively. The positive values of S observed for $K_2CuBiBr_6$ and $K_2AgBiBr_6$ compounds indicate their behavior as **p**-type semiconductors **[38]**.

b) Electrical conductivity

Electrical conductivity (**σ**), shown as a function of temperature **(Figure IV.8b)**, rises with temperature due to the thermal agitation of electrons transitioning from the valence band to the conduction band. In other words, this increase may be attributed to bond breaking and the

enhanced kinetic energy of electrons, which improves conduction in the studied compounds. At temperatures below ambient, the two compounds exhibit similar variation in **σ**. At 300K, both compounds exhibit the same value, approximately $2.4 \times 10^{18} (\Omega . m . s)^{-1}$. Beyond 300 K, the electrical conductivity profiles diverge, with $K_2AgBiBr_6$ maintaining substantially higher values than $K_2CuBiBr_6$. This difference can be attributed to the presence of different cations in the two compounds, which affects electron mobility and conduction mechanisms. Specifically, the Ag cation in $K_2AgBiBr_6$ may introduce additional energy levels that facilitate conduction, whereas the Cu cation in $K_2CuBiBr_6$ might present greater resistance to electron mobility, thereby reducing conductivity. The maximum values of **σ** observed were $3.90 \times 10^{18} (\Omega . m . s)^{-1}$for $K_2CuBiBr_6$ at 800K and $8.52 \times 10^{18} (\Omega . m . s)^{-1}$ for $K_2AgBiBr_6$ at 900K, respectively. The high Seebeck coefficient (S) allows significant voltage generation from small temperature variations, thus optimizing the conversion of thermal energy into electrical energy, and the high electrical conductivity reduces resistive heat losses, thereby improving electron flow and efficiency.

c) Electronic thermal conductivity

The temperature variation of electronic thermal conductivity (**κe/τ**) is illustrated in **Figure IV.9a**. At 300K, $K_2CuBiBr_6$ exhibits a value of 3.78×10^{13} $(W/m.K.s)$, while $K_2AgBiBr_6$ shows a slightly larger value of 5.45×10^{13} $(W/m.K.s)$. The maximum values of (**κe/τ**) observed were 6.23×10^{13} $(W/m.K.s)$ for $K_2CuBiBr_6$ at 600K and 3.48×10^{14} $(W/m.K.s)$ for $K_2AgBiBr_6$ at 900K, respectively. It is observed that the double perovskite $K_2CuBiBr_6$ exhibits lower electronic conductivity values compared to the compound $K_2AgBiBr_6$. This can be explained by the fact that copper (Cu) and silver (Ag) have different electronic configurations: [Kr] $4d^{10}$ $5s^1$ for copper and [Ar] $3d^{10}$ $4s^1$ for silver. These variations have an impact on the electronic thermal conductivity and, in turn, the density of electronic states at the Fermi level.

Because of their unique electronic characteristics and interactions with the crystal lattice, silver's orbitals may have a higher thermal conductivity than copper's. Additionally, the conduction band of $K_2AgBiBr_6$ is wider than that of $K_2CuBiBr_6$, indicating that the double perovskite containing silver has higher electron mobility and, as a result, higher electronic thermal conductivity. The lattice thermal conductivity (κ_L/τ) was not addressed due to a lack of software and powerful computing stations.

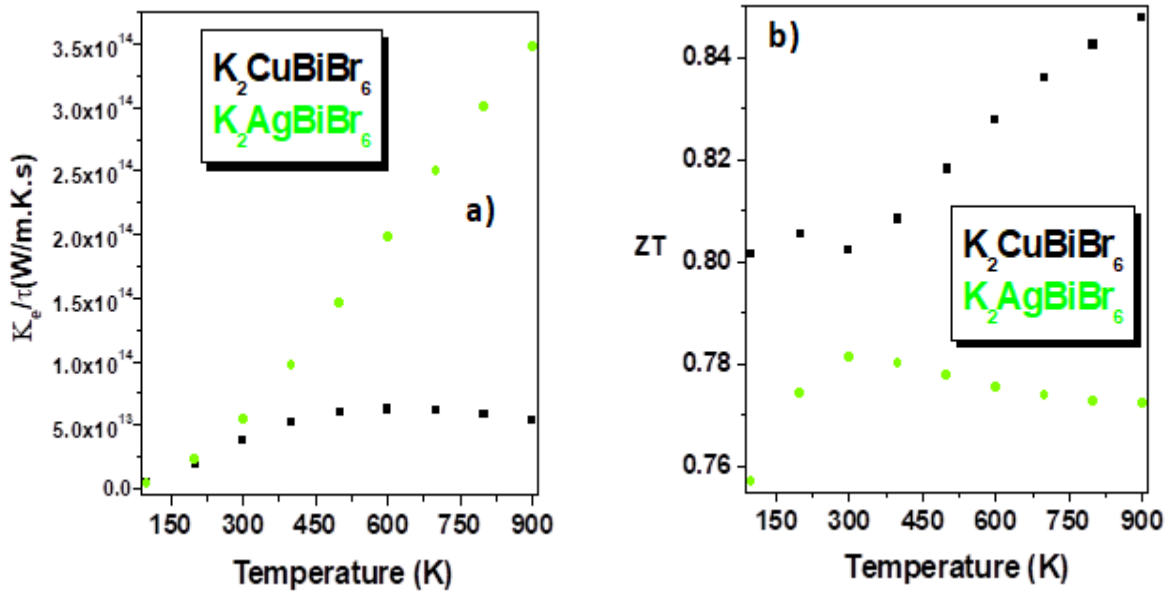

Figure IV.9 (a) Electronic thermal conductivity (Ke/τ), and (b) Merit factor (ZT) of $K_2CuBiBr_6$, and $K_2AgBiBr_6$ double Perovskites

However, in semiconductors, at low temperatures, lattice thermal conductivity is higher than electronic conductivity due to the low scattering of phonons **[39]**. Lattice conductivity falls at high temperatures due to increased phonon interactions, which restricts their capacity to transfer heat, while electronic conductivity becomes dominant due to increased thermal agitation of electrons.

d) Merit factor

Figure IV.9b illustrates the variation of the merit factor (ZT) versus temperature. For the compounds $K_2CuBiBr_6$ and $K_2AgBiBr_6$, the ZT values at 300 K are 0.80 and 0.78, respectively. As the temperature increases, $K_2CuBiBr_6$ shows a progressive increase, reaching 0.84 at 900 K, while $K_2AgBiBr_6$ exhibits a very slight decline, with a value of 0.77 around 900 K. As the temperature increases, thermal vibrations (phonons) in the $K_2CuBiBr_6$ compound become more significant, and the material manages to limit the rise in thermal conductivity while improving its electrical conductivity, leading to this progressive increase in the ZT value. The small variation in ZT (from 0.78 to 0.77 between 300 K and 900 K) suggests that $K_2AgBiBr_6$ has relatively stable thermal and electronic properties. This is due to its low phonon thermal conductivity, good electrical conductivity, and a very slight variation in the Seebeck coefficient over a wide temperature range, which limits the decrease in thermoelectric efficiency at high temperatures. The high ZT values over a wide temperature range for the double perovskite $K_2CuBiBr_6$ indicate that it has a superior ability to convert heat into electricity compared to the

$K_2AgBiBr_6$ compound. In this context, at room temperature, our compounds exhibit ZT values higher than those of several other DP compounds, such as $Rb_2LiTlBr_6$ **[18]**, Ba_2InNbO_6 **[29]** and Rb_2YCuCl_6 **[40]**.

IV.7 Conclusion

The structural stability of the $K_2CuBiBr_6$ and $K_2AgBiBr_6$ compounds, along with their electronic, elastic, optical, and thermoelectric properties, was investigated using first-principles calculations based on density functional theory (DFT). Structural optimization indicates that the non-magnetic (NM) phase is the most stable compared to the ferromagnetic (FM) and antiferromagnetic (AFM) phases. The negative values of formation enthalpy and cohesive energy confirm their thermodynamic stability and synthesizability. The electronic structure analysis reveals that both compounds are semiconductors with indirect band gaps. At the atomic scale, $K_2CuBiBr_6$ and $K_2AgBiBr_6$ exhibit distinct mechanical behaviors. $K_2CuBiBr_6$ is more resistant to compression than to shear deformation, whereas $K_2AgBiBr_6$ shows directional variations in rigidity. Both compounds have similar bulk moduli; however, $K_2AgBiBr_6$ possesses a higher shear modulus, indicating greater stiffness. According to Pugh's criterion, $K_2AgBiBr_6$ is classified as brittle, while $K_2CuBiBr_6$ exhibits ductility. In terms of optical properties, both compounds demonstrate significant absorption in the visible and ultraviolet regions. Their refractive indices indicate an efficient ability to refract light, making them suitable candidates for light-emitting diode (LED) applications. Additionally, their reflectivity values suggest potential use in solar panel coatings. Thermoelectric analysis shows that the Seebeck coefficient decreases with increasing temperature for both compounds, indicating p-type semiconductor behavior. In contrast, electrical conductivity increases with temperature due to thermal excitation, reaching approximately 2.4×10^{18} $(\Omega \cdot m \cdot s)^{-1}$ at 300 K. At 300 K, $K_2CuBiBr_6$ exhibits a figure of merit (ZT) of 0.80 compared to 0.78 for $K_2AgBiBr_6$. At 900 K, $K_2CuBiBr_6$ improves slightly to 0.84, while $K_2AgBiBr_6$ decreases marginally to 0.77. This increase in ZT for $K_2CuBiBr_6$ results from enhanced electrical conductivity and reduced thermal conductivity due to increased phonon scattering. Therefore, $K_2CuBiBr_6$ appears to be more efficient for thermoelectric energy conversion.

References

[1] S. Zuhair A. Shah, S. Niaz, Lead-free indium-silver based double perovskites for thermoelectric applications: Structural, electronic and thermoelectric properties using first-principles approach, Materials Today Communications 28 (2021) 102609.
[2] D. Abdullah, D.C. Gupta, Understanding the mechanical, opto-electronic, and thermoelectric properties of lead-free Silver based perovskites Cs_2YAgX_6 computational study, Computational Condensed Matter 40 (2024) e00924.
[3] J. Qiua, C. Lia, F. Lianga, J. Wanga, L. Taoa, D. Mo, L. Dong, Bin Li, Surface B-site exsolving double perovskite supported copper use for control the catalytic performance for high-temperature CO-SCR, Surfaces and Interfaces 51 (2024) 104635.
[4] Md Roknuzzaman, J.A. Alarco, H. Wang, Kostya (Ken) Ostrikov, Structural, electronic and optical properties of lead-free antimony-copper based hybrid double perovskites for photovoltaics and optoelectronics by f irst principles calculations, Computational Materials Science 186 (2021) 110009.
[5] E.T. McClure, M.R. Ball, W. Windl, P.M. Woodward, Cs_2AgBiX_6 (X= Br, Cl): new visible light absorbing, lead-free halide perovskite semiconductors, Chem. Mater. 28 (5) (2016) 1348–1354.
[6] O. Oktay, U. Uzun, I.C. Kaya, Simple and solvent-free procedure for fabricating Ag/Bi-based halide double perovskite polycrystalline wafers and investigating their photodetector properties, Journal of solid-state chemistry 338 (2024) 124876.
[7] W. Shen, U. Jung, Z. Xian, B. Jung, J. Park, Enhanced device performance of $Cs_2AgBiBr_6$ double perovskite photodetector by SnO_2/ZnO double electron transport layer, Journal of Alloys and Compounds 929 (2022) 167329.
[8] B. Akenoun, S. Dahbi, N. Tahiri, O.El Bounagui, H. Ez-Zahraouy, Engineering the optoelectronic and thermoelectric properties of Cs_2BiAgY_6 (Y= Br or Cl) double perovskites through doping with iodine: A DFT study, Journal of Physics and Chemistry of Solids 194 (2024) 112229.
[9] S.Al-Qaisi, Q. Mahmood, N.A. Kattan, S. Alhassan, T. Alshahrani, N. Sfina, S. Brini, A. Hakamy, A. Mera, M.A. Amin,Tuning of band gap by variation of halide ions in K2CuSbX6 (X =Cl, Br, I) for solar cells and thermoelectric applications, journal of physics and chemistry of solids 174 (2023) 111184.
[10] H. Albalawi, S.A. Rouf, T. Zelai, N. A. Kattan, S. Bouzgarrou, Q. Mahmood, S. Al-Qaisi, El Sayed Yousef, The study optical, thermoelectric, and thermodynamic properties of double perovskites $K2CuBiX_6$ (X= Cl, Br, I) forenergy harvesting, Mater. Sci. Eng. B 298 (2023) 116851.
[11] J.A. Mashot, K.A. Khalaph, H. B. Al Husseini, Study of the structural, electronic, mechanical, electro-thermal and optical properties of double perovskite structures Cs_2SbAgX_6,(X= I, Br, or Cl), Phys. Scripta 97 (2022) 085509.
[12] M. Manzoor, M.W. Iqbal, M. Imran, N.A. Noor, A.Mahmood, Y.M. Alanazi, S. Aftab, Probing direct bandgap of double perovskites Rb_2LiTlX_6 (X= Cl, Br) and optoelectronic characteristics for Solar cell applications: DFT calculations, J. Mater. Res. Technol. 18 (2022) 4775.
[13] S. Janaki, S. Lephe, S.M. Gifrin Fredik Raj, S. Sahaya Jude Dhas, L. Arun Jose, Synthesis and characterization of novel double perovskite $K_2AgBiBr_6$, optical materials 156 (2024) 115941.
[14] E. Haque, M. A. Hossain, Origin of ultra-low lattice thermal conductivity in Cs_2BiAgX_6 (X=Cl, Br) and its impact on thermoelectric performance, Journal of alloys and compounds. 748 (2018) 63.
[15] K. Momma, and F. Izumi, VESTA 3 for three-dimensional visualization of crystal, volumetric and morphology data, J. Appl. Crystallogr. 44, 1272-1276 (2011).

[16] H. Murtaza, Q. Ain, J. Munir, H. Ullah, H.M. Ghaithan, A.A.Ali Ahmed, S.M.H. Qaid, Unveiling the mechanical, structural, thermoelectric, and optoelectronic potential of K2NaGaBr6 and K2RbTlBr6 double perovskites for sustainable technologies, solar energy 273 (2024) 112502.
[17] M. Q. Shah, M. Shafiq, A. Naeem, G. Murtaza, A. Ayyaz, A. Usman, S.M. Deen, M.A. El-Sheikh, Effect of position occupancy of different elements on the structural stability, optoelectronic, thermoelectric and elastic properties of Cs_2CuAsX_6 (X: Cl, Br, I) halide double perovskite: DFT analysis, Materials science in semiconductor processing 174 (2024) 108187.
[18] A. Ayyaz, G. Murtaza, N. Algethami, A. Usman, M.B. Shakir, Q. Mahmood, Influence of alkali metal cation modifications on physical characteristics of double perovskites Rb_2XTlBr_6 (X=Li, Na, K): First-principles study for solar energy and thermoelectric applications, Physica B 690(2024) 416245.
[19] G. Hautier, S.P. Ong, A. Jain, C.J. Moore, G. Ceder, Accuracy of density functional theory in predicting formation energies of ternary oxides from binary oxides and its implication on phase stability, Phys. Rev. B 85 (2012) 155208.
[20] M.D. Kassa, N.G. Debelo, M.M.J. Woldemariam, First-principles calculations to investigate small band gap Ca_2ZrHfS_6 double chalcogenide perovskites for optoelectronic application, Indian J. Phys. (2023) 1–12.
[21] M. Roudgar-Amoli, E. Abedini, A. Alizadeh, Z. Shariatinia, Understanding double perovskite oxides capabilities to improve photocatalytic contaminants degradation performances in water treatment processes: A review, Journal of Industrial and Engineering Chemistry 129 (2024) 579-619.
[22] A.Kumar, P. Sharma, G. Sharma et al., Simultaneous hydrogen production and photocatalytic pollutant removal: a review, Environmental Chemistry Letters 22 (2024) 2405–2424.
[23] J. Hornstra, W. Bartels, Determination of the lattice constant of epitaxial layers of III-V compounds. J. Cryst. Growth 44, (1978) 513–517.
[24] S. Wang, H. Ye, First-principles study on elastic properties and phase stability of III–V compounds. Phys. Status Solidi 240, (2003) 45.
[25] M. Born and K. Huang, Dynamics Theory of Crystal Lattices (Oxford University Press, 1954).
[26] J. Haines, J.M. Leger, G. Bocquillon, Synthesis and Design of Superhard Materials, Annu. Rev. Mater. Res. 31 (2001) 1.
[27] S. Pugh, XCII. Relations between the elastic moduli and the plastic properties of polycrystalline pure metals, the London, Edinburgh, and Dublin philosophical magazine and journal of science, 45 (1954) 823.
[28] G. Marius, the Physics of Semiconductors: Kramers-kronig Relations, Springer, Berlin Heidelberg (2010) 775–776.
[29] A.Dixit, J.A. Abraham, M. Manzoor, M. Altaf, Y.A. Kumar, R. Sharma, A comprehensive DFT analysis of the physical, optoelectronic and thermoelectric attributes of Ba_2lnNbO_6 double perovskites for eco-friendly technologies, Materials Science & Engineering B 307 (2024) 117530.
[30] S. Ahmad, J. Feng, M. Zakria, S.H. Shah, A. Alam, S. Shakeel, D. Muhammad, I. ullah, DFT-based nano architectonics: Exploring Structural, Mechanical, and optoelectronic properties of halide double perovskites $K_2ScAgX6$ (X=Cl, Br and I), Materials Science & Engineering B 309 (2024) 117641.
[31] M.A. Rehman, Z.Ur Rehman, M. Usman, S.Y. Alomar, M. Sohaib, A. Hamad, Computational insights into the multifunctional properties of Li_2AgBiX_6 (X=Cl, Br, I)

double perovskite materials, Materials Science in Semiconductor Processing 184 (2024) 108793.

[32] N. Rahman, M. Husain, A. Azzouz-Rached et al., Theoretical investigations of double perovskites Rb_2YCuX_6 (X =Cl, F) for green energy applications: DFT study, Journal of physics and chemistry of solids 193 (2024) 112171.

[33] A. Ejjabli, M. Karouchi, M. Al-Hattab, O. Bajjou, K. Rahmani, Y.Lachtioui, Investigation of lead-free halide K2AgSbBr6 double Perovskite's structural, electronic, and optical properties using DFT functionals, chemical physics impact 9 (2024) 100656.

[34] Md.F. Rahman, Z.R. Melody, Md.H. Ali, A. Ghosh, P. Barman, Md.R. Islam, M. K. Hossain, First-principles analysis of how Cobalt doping affects the structural, electronic, and optical properties of α-MoO3, Indian J. Phys. (2023).

[35] Ming Ma, Frank W. Mont, Xing Yan and al., Effects of the refractive index of the encapsulant on the light-extraction efficiency of light-emitting diodes**,** Optics Express 19 (S5) (2011) A1135-A1140.

[36] D. Poelman, P.F. Smet, Methods for the determination of the optical constants of thin films from single transmission measurements: a critical review. J. Phys. D Appl. Phys. **36**, 1850 (2003).

[37] N. Rodkey, K. P. S. Zanoni, M. Piot, C. Dreessen, R. Grote, P. Carroy, J. E. Sebastian Alonso, A. Paliwal, D. Muñoz, H. J. Bolink, Efficient Micrometer Thick Bifacial Perovskite Solar Cells. *Adv. Energy Mater.* (2024) 14, 2400058.

[38] A.H. Reshak, Thermoelectric properties of fully hydrogenated graphene: semi-classical Boltzmann theory, J. Appl. Phys. 117 (2015) 225104.

[39] J. Yuan, M. Li and H. Wang, Intrinsically ultralow lattice thermal conductivity and giant thermoelectric effect in Ag-based intercalated layered crystalline solids. *Physical Review B*, 109(23) (2024) 235202.

[40] N. Rahman, M. Husain, A. Azzouz-Rached, et al., Theoretical investigations of double perovskites Rb_2YCuX_6 (X =Cl, F) for green energy applications: DFT study, Journal of Physics and Chemistry of Solids 193 (2024) 112171.

CHAPTER V

Application to embedded systems

V.1 Introduction

The rise of embedded systems has transformed energy and environmental technologies by enabling intelligent monitoring, control, and optimization of complex processes **[1]**. Their integration into renewable energy, environmental monitoring, and photocatalytic reactors promotes autonomous and efficient solutions. At the same time, perovskites open new prospects for light-driven processes such as solar conversion, pollutant degradation, and hydrogen production **[2][3]**. This chapter highlights the synergy between embedded systems and perovskite materials **[4]**, drawing on DFT and modeling approaches to design intelligent and sustainable photocatalytic systems **[5]**.

V.2 Embedded Systems and Energy Applications

V.2.1 Definition of Embedded Systems

Embedded systems are specialized computing devices, optimized for specific functions under constraints of size, energy, and real-time performance **[6]**. Comprising a microcontroller, memory, interfaces, and dedicated software **[7]**, they provide efficiency, reliability, and autonomy across various domains, from automotive to energy. In energy and environmental applications, they enable real-time monitoring, control, and process optimization, thereby enhancing sustainability and performance.

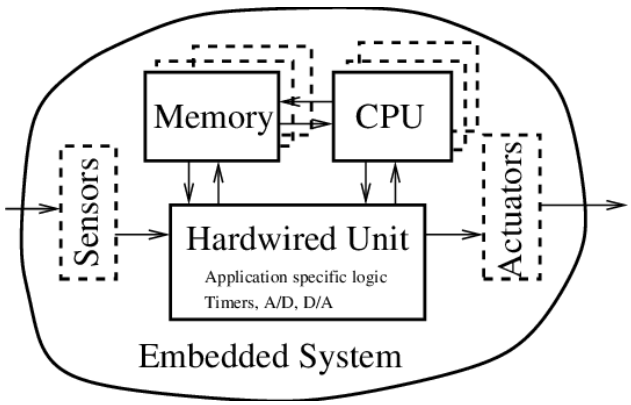

Figure V.1 Schematic Representation of Embedded System Components

V.2.2 Embedded Systems in Renewable Energy and Environmental Monitoring

Embedded systems have become essential in renewable energy due to their role in performance optimization, reliability, and automation. They regulate power conversion, track the maximum power point (MPPT), manage storage, and ensure grid integration, thereby improving efficiency and reducing costs. In photovoltaic and wind applications, they dynamically adapt operating conditions in real time to maximize energy production and ensure stability. Moreover, they play a key role in environmental monitoring by enabling the autonomous collection and

processing of data (air quality, water quality, pollution). With sensors and low-power microcontrollers, they provide real-time monitoring, even in remote areas.

Coupling energy-harvesting technologies with embedded systems paves the way for self-powered devices, particularly useful in photocatalysis to regulate light sources and optimize chemical reactions. Thus, embedded systems serve as a bridge between renewable energy, environmental sustainability, and intelligent control.

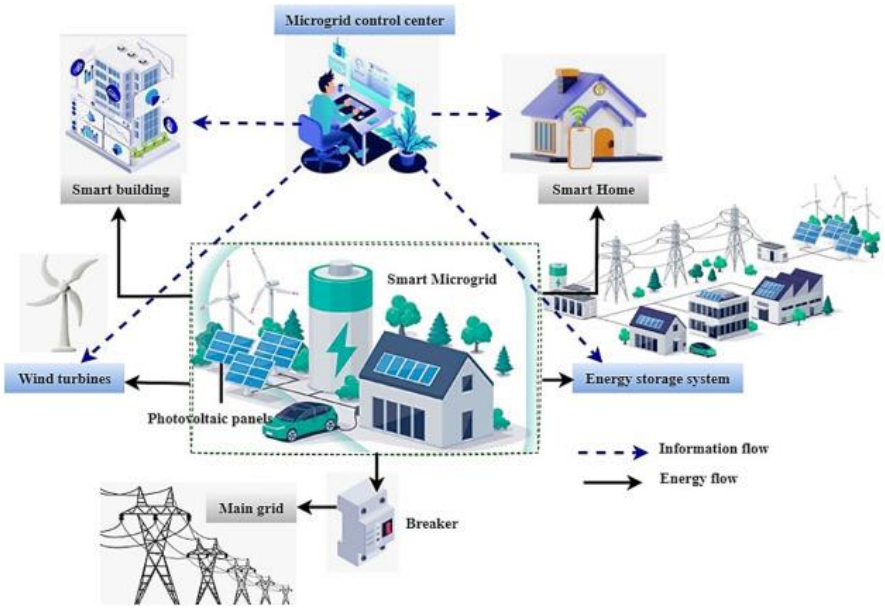

Figure V.2 Schematic Representation of a Smart Microgrid with Embedded System Integration

V.2.3 Integration of Photocatalysis into Embedded Systems

The integration of photocatalysis into embedded systems represents a major step toward autonomous and intelligent environmental technologies. Based on the activation of semiconductors under light irradiation, photocatalysis offers promising applications in water purification, pollutant degradation, and solar-driven hydrogen production **[9]**. However, its practical deployment requires precise control of reaction conditions (light intensity, duration, pH, temperature) and real-time monitoring of catalytic efficiency. Embedded systems provide the necessary platform to ensure such control and automation **[10]**.

By integrating microcontrollers, sensors, and actuators, they can regulate light sources, monitor parameters such as dissolved oxygen or pollutant concentration, and dynamically adjust operating conditions. With embedded communication modules, these devices can also be remotely monitored and deployed in isolated environments.

The synergy between photocatalysis and embedded systems thus enables the development of smart, sustainable, and autonomous devices. When coupled with renewable energy sources

(e.g., solar panels), these integrated systems operate as self-powered units for long-term environmental remediation and clean energy generation, particularly in water treatment, air purification, and green hydrogen production.

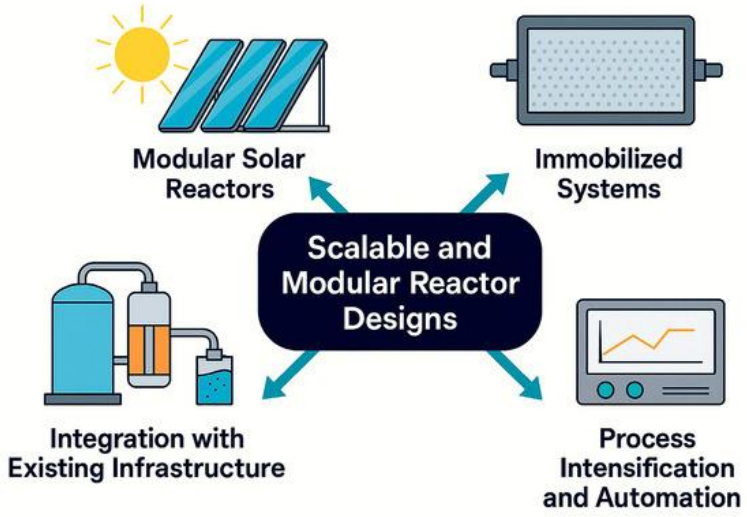

Figure V.3 Modular photocatalytic reactor design

V.3 Motivation for Perovskite-Based Photocatalysis in Embedded Systems

Perovskite materials are versatile semiconductors with remarkable optoelectronic properties (strong light absorption, tunable bandgap, long carrier diffusion length), well-suited for embedded systems where efficiency, compactness, and flexibility are essential. Their low-cost solution processing enables lightweight and flexible devices.

The most studied application is in perovskite solar cells (PSCs) **[11]**, which integrate embedded systems for maximum power point tracking (MPPT), fault detection, and performance optimization. Compact microcontroller-based units regulate power conversion and energy storage, making these devices suitable for portable and autonomous platforms. Similarly, perovskite photodetectors and sensors exhibit high sensitivity and fast response times **[12]**, useful in imaging, environmental monitoring, and communication.

Beyond photovoltaics and sensing, perovskites are promising for photocatalysis in embedded systems, for instance in water purification, hydrogen production, or pollution control. Embedded controllers manage illumination, monitor catalytic efficiency, and ensure autonomous operation **[13]**. Thus, integrating perovskites into energy-related embedded systems highlights their dual role as active functional materials and enablers of innovative architectures, bridging advanced material science and intelligent system design. The motivation for using perovskites in photocatalysis within embedded systems lies in their tunable

optoelectronic properties and low-cost synthesis. Unlike conventional photocatalysts (TiO_2), they offer adjustable bandgaps matching the solar spectrum, as well as band positions favorable to water redox reactions, enabling efficient H_2 and O_2 evolution under visible light **[14]**. From an embedded systems perspective, photocatalysis requires intelligent control of conditions (light intensity, temperature, reaction medium). Embedded systems enable regulation, automation, and real-time monitoring **[15]**, paving the way for autonomous and smart photocatalytic devices. This integration is promising for pollution remediation and sustainable energy conversion **[16]**. For example, a perovskite-based reactor equipped with sensors and microcontrollers can degrade pollutants or optimize hydrogen generation while adapting to fluctuating conditions. Thus, the interest of perovskites in embedded photocatalysis lies in the synergy between material performance and intelligent design, supporting the development of autonomous, adaptive, and sustainable technologies **[17]**.

V.4 Fundamentals of Photocatalysis

V.4.1 Principles of Photocatalysis

Photocatalysis is a light-driven process where a semiconductor absorbs photons to generate electron–hole pairs, enabling surface redox reactions such as water splitting and pollutant degradation **[18]**. Efficiency depends on minimizing charge carrier recombination through strategies like bandgap engineering, surface modification, and heterojunction design. The process involves three key steps: light absorption and carrier generation, carrier transport and separation, and surface reactions. Proper band alignment (CBM above H^+/H_2, VBM below H_2O/O_2) ensures thermodynamic feasibility **[19]**. Photocatalysis thus offers a promising route for energy conversion and environmental remediation, especially when coupled with embedded control systems to enhance stability and efficiency.

V.4.2 Criteria for an Efficient Photocatalyst

The performance of a photocatalyst depends on structural, electronic, and chemical factors governing light absorption **[20]**, charge carrier dynamics, and surface reactivity. An efficient photocatalyst requires a visible-range bandgap (1.5–3.0 eV) with band edges properly aligned to redox potentials (CBM < H^+/H_2; VBM > H_2O/O_2) to ensure thermodynamic feasibility **[21]**. Efficiency also relies on charge separation and transport **[22]**, demanding low defect density and passivation. Chemical and structural stability is essential under irradiation and in aqueous media **[23]**. Practical viability requires low-cost, non-toxic, and earth-abundant materials compatible with embedded systems **[24]**.

V.5 DFT-Based Evaluation of Photocatalytic Suitability

V.5.1 Theoretical Framework and Methodology

The evaluation of photocatalytic performance in the studied materials builds upon the theoretical foundations presented in **Chapter II** and the structural, electronic, and optical analyses detailed in **Chapters III** and **IV**. As outlined previously, Density Functional Theory (DFT) provides the basis for investigating ground-state properties, while in this chapter the same framework is extended to assess photocatalytic suitability.

All calculations were carried out within the Generalized Gradient Approximation (GGA) using the Perdew-Burke-Ernzerhof (PBE) functional, which was already employed for structural optimization and electronic structure determination in earlier sections. The optimized lattice parameters and band structures obtained in **Chapters III** and **IV** form the starting point for photocatalytic analysis.

The methodology focuses on relating the electronic band edge positions of the compounds to the thermodynamic redox potentials for water splitting. Specifically, the conduction band minimum (CBM) is compared with the reduction potential of H^+/H_2, while the valence band maximum (VBM) is aligned against the oxidation potential of H_2O/O_2. This comparison enables evaluation of whether the materials meet the fundamental energetic requirements for photocatalytic activity.

V.5.2 Band Edge Positions and MATLAB Validation

The determination of the band edge positions of a semiconductor is a crucial step in assessing its suitability as a photocatalyst for water splitting and related environmental processes. In this study, the band edges were calculated using the absolute electronegativity approach, which directly links the conduction band minimum (CBM) and valence band maximum (VBM) to the material's electronegativity and band gap. The equations used for this purpose are given by**[25]**.

$$\mathbf{E_{CBM} = \chi - E_e - \frac{1}{2}E_g} \qquad (\mathbf{V.1})$$

$$\mathbf{E_{VBM} = E_{CBM} + E_g} \qquad (\mathbf{V.2})$$

where χ represents the absolute electronegativity of the compound, $\mathbf{E_e}$ is the free-electron energy on the hydrogen scale (taken as 4.5 eV), and $\mathbf{E_g}$ is the band gap obtained from density functional theory calculations. Mulliken absolute electronegativity is defined as **[26]**:

$$\mathbf{\chi = \frac{1}{2}(IP + EA)} \qquad (\mathbf{V.3})$$

where IP is the ionization potential and EA the electron affinity (both in eV). For a solid, this can be expressed using absolute (vacuum-referenced) band edges [27].

$$\mathbf{IP} = \mathbf{E_{VAC}} - \mathbf{E_{VBM}} \quad (\mathbf{V.4})$$

$$\mathbf{EA} = \mathbf{E_{VAC}} - \mathbf{E_{CBM}} \quad (\mathbf{V.5})$$

To facilitate the evaluation of multiple compounds, these equations were implemented in a MATLAB environment, where the code was designed to automatically process the input parameters, calculate the band edge positions, and generate graphical outputs. The graphical representation included the calculated CBM and VBM values plotted with respect to the redox potentials of water splitting, namely the oxygen evolution potential ($E_{O_2/H_2O} \approx -5.67$ eV) and the hydrogen reduction potential ($E_{H^+/H_2} \approx -4.44$ eV), represented as reference lines. In this way, the MATLAB code [28] not only eliminated the risk of manual computational errors but also enabled the automated generation of band alignment diagrams, which allowed for direct visual inspection of photocatalytic feasibility. A material is deemed suitable for photocatalysis only if its conduction band lies above the hydrogen reduction potential and its valence band lies below the oxygen evolution potential.

V.5.3 Selection of Promising Perovskite Compounds

Table V.I summarizes the calculated electronic band gaps and absolute band-edge positions of the studied perovskite and double perovskite compounds, expressed relative to both the vacuum level and the normal hydrogen electrode (NHE). For efficient photocatalytic water splitting, two criteria must be simultaneously satisfied: (i) the band gap should lie within the visible-light range (1.5–3.0 eV), and (ii) the conduction band minimum (CBM) must be more negative than the H^+/H_2 reduction potential (0 V vs. NHE), while the valence band maximum (VBM) must be more positive than the O_2/H_2O oxidation potential (+1.23 V vs. NHE) as shown in **Figure V.4**.

Table V.I Calculated Band-Gap, absolute electronegativity, and Band-Edge Positions of the perovskites and double perovskite compounds

Compound	Eg (eV)	χ (eV)	E_{CBM}	E_{VBM}
$CeBeO_3$	0.73	7.80	+2.935	+3.665
$CeMgO_3$	0.51	7.50	+2.745	+3.255
$K_2CuBiBr_6$	1.73	5.90	-0.335	+1.195
$K_2AgBiBr_6$	2.83	6.20	-0.285	+2.545

From the results, **$CeBeO_3$** and **$CeMgO_3$** exhibit very narrow indirect band gaps of 0.73 eV and 0.51 eV, respectively. While these narrow gaps suggest strong electronic conductivity, they are unsuitable for photocatalysis because they fall well below the optimal energy range and lead to excessive carrier recombination. Moreover, their band edges do not straddle the redox potentials, further excluding them as viable candidates for photocatalytic water splitting.

In contrast, the double perovskites **$K_2CuBiBr_6$** and **$K_2AgBiBr_6$** show band gaps of 1.73 eV and 2.83 eV, respectively both of which fall within the visible-light absorption window. Importantly, their CBM values (−0.335 V for $K_2CuBiBr_6$ and −0.285 V for $K_2AgBiBr_6$ vs. NHE) lie above the hydrogen reduction potential, providing sufficient driving force for H_2 generation. Similarly, their VBMs (+1.195 V and +2.545 V vs. NHE) are well above the oxygen oxidation potential, ensuring strong hole-driven O_2 evolution. This combination of suitable band gaps and favorable band-edge alignment indicates that both $K_2CuBiBr_6$ and $K_2AgBiBr_6$ possess the thermodynamic requirements for overall water splitting under visible light irradiation.

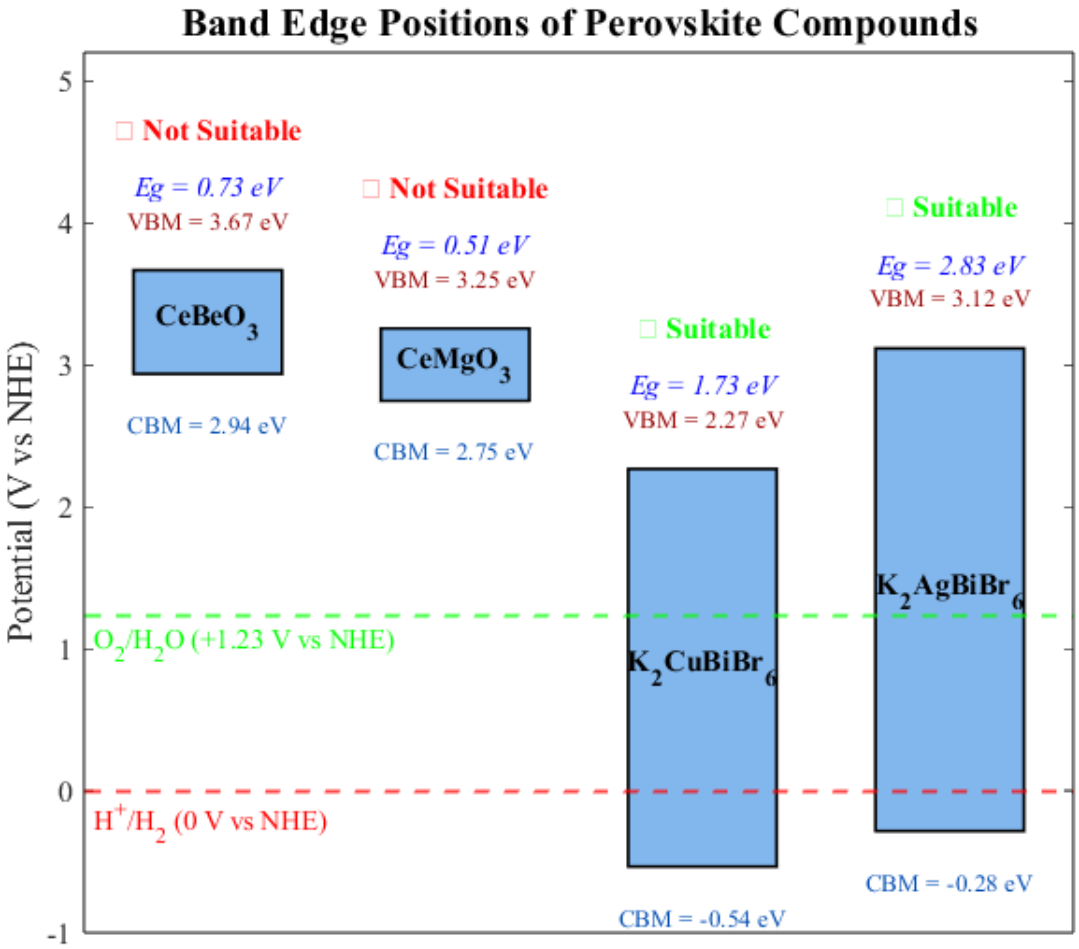

Figure V.4 Band Alignment of Perovskites with Water Redox Potentials

V.6 Conclusion

In conclusion, the analysis of band edge positions using the absolute electronegativity method clearly distinguished promising photocatalytic materials from ineffective compounds. The perovskites $CeBeO_3$ and $CeMgO_3$, although conductive, exhibit excessively narrow gaps and unfavorable band alignment, rendering them unsuitable for water splitting. In contrast, the double perovskites $K_2CuBiBr_6$ and $K_2AgBiBr_6$ simultaneously satisfy the two fundamental criteria, namely a band gap within the visible range and favorable alignment with respect to redox potentials, positioning them as strong candidates for H_2 and O_2 generation under visible-light irradiation. These results confirm the relevance of the electrostatic approach combined with numerical modeling for the rational screening of new photocatalysts.

References

[1] I. Sofianidis, V. Konstantakos, and S. Nikolaidis, Reducing Energy Consumption in Embedded Systems Applications, Technologies, 13 (2025) 82.

[2] N. Subha, A. Ravi Sankar, S. Navaneethakrishnan, J. Lavanya, and M. Aakash, Perovskite-based Z-scheme photocatalytic system for hydrogen production, Catalysis Communications, 187 (2024) 106903.

[3] X. Wang, Y. Peng, S. Yang, H. G. Yang, and Y. Hou, "Recent progress in metal halide perovskite photocatalysts for hydrogen evolution," Mater. Chem. Front. 7 (2023) 4635–4657.

[4] J. Ma et al. Self-powered and self-calibrated sensing system for real-time environmental monitoring, Science Advances, 11 (2025) 3745.

[5] O. H. Romero Ocampo, Environmental Information System Using Embedded Systems Aimed at Improving the Productivity of Agricultural Crops in the Department of Meta, in Proceedings of the Future Technologies Conference, Springer, (2022) 837–849.

[6] I. Sofianidis, V. Konstantakos, and S. Nikolaidis, Reducing Energy Consumption in Embedded Systems Applications, Technologies, 13 (2025) 82.

[7] M. Bitar, T. El Tawil, M. Benbouzid, V. B. Dinh, and M. Benaouicha, On Hybrid Nanogrids Energy Management Systems - An Insight into Embedded Systems, Applied Sciences, 14 (2024) 1563.

[8] Y. Lisboa et al. Design and Implementation of a Sustainable IoT Embedded System for Monitoring Temperature and Humidity in Photovoltaic Power Plants in the Amazon, Sustainability, 17 (2025) 2347.

[9] X. Wang, Y. Peng, S. Yang, H. G. Yang, and Y. Hou, Recent progress in metal halide perovskite photocatalysts for hydrogen evolution, Materials Chemistry Frontiers, 7 (2023) 4635–4657.

[10] O. H. Romero Ocampo, Environmental Information System Using Embedded Systems Aimed at Improving the Productivity of Agricultural Crops in the Department of Meta, in Proceedings of the Future Technologies Conference, Springer, (2022) 837–849.

[11] N. S. Kumar and K. C. B. Naidu, A review on perovskite solar cells (PSCs), materials and applications, Journal of Materiomics, 7 (2021) 940–956.

[12] J. Wolanyk et al. Tunable perovskite-based photodetectors in optical sensing, Sensors and Actuators B : Chemical 321(2020) 128462.

[13] W. Han et al. All Irradiance-Applicable, Perovskite Solar Cells-Powered Flexible Self-Sustaining Sensor Nodes for Wireless Internet-of-Things, Advanced Functional Materials, (2025) 2425697.

[14] L. Yue, B. Yan, M. Attridge, and Z. Wang, Light absorption in perovskite solar cell : Fundamentals and plasmonic enhancement of infrared band absorption, Solar Energy, vol. 124 (2016) 143–152.

[15] M. Nagl, Embedded Systems: Rules to Improve Adaptability, in Software Architectures: Topics Usually Missed in Textbooks, Springer (2024) 69–94.

[16] W. Wang, M. O. Tade, and Z. Shao, Research progress of perovskite materials in photocatalysis-and photovoltaics-related energy conversion and environmental treatment, Chemical Society Reviews, 44 (2015) 5371–5408.

[17] W. Han et al. All Irradiance-Applicable, Perovskite Solar Cells-Powered Flexible Self-Sustaining Sensor Nodes for Wireless Internet-of-Things, Advanced Functional Materials, (2025) 2425697

[18] R. Ameta, M. S. Solanki, S. Benjamin, and S. C. Ameta, Photocatalysis, in Advanced oxidation processes for waste water treatment, Elsevier, (2018) 135–175.

[19] Z. Zhang et al. Benzotrifuran-Based Covalent Organic Frameworks for Artificial Photosynthesis of H_2O_2 from H_2O, O_2, and Sunlight, Angewandte Chemie (2025).

[20] K. E. Karakitsou and X. E. Verykios, Effects of altervalent cation doping of titania on its performance as a photocatalyst for water cleavage,The Journal of Physical Chemistry, 97 (1993) 1184–1189.

[21] E. A. Abdullah, Band edge positions as a key parameter to a systematic design of heterogeneous photocatalyst,European journal of chemistry 10 (2019) 82–94.

[22] R. Marschall, Semiconductor composites : strategies for enhancing charge carrier separation to improve photocatalytic activity, Advanced Functional Materials, 24 (2014) 2421–2440

[23] Q. Dai et al. Effects of templates on the structure, stability and photocatalytic activity of mesostructured TiO2, Journal of Photochemistry and Photobiology A: Chemistry, 148 (2002) 295–301.

[24] S. Younis and K.-H. Kim, Heterogeneous Photocatalysis Scalability for Environmental Remediation : Opportunities and Challenges, Catalysts, 10 (2020) 1109.

[25] A. Walsh and K. T. Butler, “Prediction of Electron Energies in Metal Oxides, Acc. Chem. Res., 47 (2014) 364–372.

[26] C.-G. Zhan, J. A. Nichols, and D. A. Dixon, Ionization Potential, Electron Affinity, Electronegativity, Hardness, and Electron Excitation Energy : Molecular Properties from Density Functional Theory Orbital Energies, J. Phys. Chem. A, 107 (2003) 4184–4195.

[27] Y. Xu and M. A. A. Schoonen, The absolute energy positions of conduction and valence bands of selected semiconducting minerals, American Mineralogist, 85 (2000) 543–556.

[28] D. Kumar, A Tutorial on Gassmann Fluid Substitution : Formulation, Algorithm and Matlab Code. Geohorizons (2006).

General Conclusion

This thesis represents a comprehensive theoretical investigation into two classes of lead-free perovskite materials: the simple perovskites $CeBO_3$ (B = Be, Mg) and the double perovskites K_2BBiBr_6 (B = Cu, Ag). The central motivation behind this work was to address two major scientific and technological challenges: the environmental hazards associated with lead-based perovskites and the urgent need for high-performance alternatives in energy conversion and optoelectronic devices. By employing advanced computational techniques based on density functional theory (DFT), complemented with semi-classical Boltzmann transport theory, this research has provided an in-depth understanding of the structural, electronic, elastic, optical, and thermoelectric properties of these materials. The overarching aim was to identify compounds that combine chemical stability, excellent optoelectronic performance, and environmental safety, thus contributing to the global effort of developing sustainable and high-efficiency functional materials.

The structural analysis carried out in this study revealed that all the investigated compounds exhibit remarkable stability, an essential prerequisite for practical applications. The simple perovskites $CeBeO_3$ and $CeMgO_3$ crystallize in a nearly ideal perovskite structure, with Goldschmidt tolerance factors close to 0.98 and 0.99, respectively, confirming minimal structural distortion from the cubic symmetry. These values fall well within the stability range reported in literature for robust perovskite frameworks. The optimized lattice parameters were found to be approximately 3.60 Å for $CeBeO_3$ and 3.85 Å for $CeMgO_3$, consistent with the size difference between Be and Mg cations. Furthermore, their formation enthalpies were negative, around −1.18 eV/atom. for $CeBeO_3$ and −1.11 eV/atom. for $CeMgO_3$, indicating excellent thermodynamic stability.

Similarly, the structural investigation of the double perovskites $K_2CuBiBr_6$ and $K_2AgBiBr_6$ demonstrated robust phase stability and well-ordered crystal frameworks. Their optimized lattice constants were found to be 11.90 Å and 11.97 Å, respectively, while their tolerance factors approached unity, ensuring minimal octahedral tilting within the lattice. These observations are consistent with the general structural trends observed for halide double perovskites, reinforcing their viability as a replacement for lead-based compounds in

optoelectronic technologies. The calculated cohesive energies were negative for both materials, further supporting their thermodynamic stability. Taken together, these findings establish a strong foundation for the potential large-scale synthesis and integration of these compounds into functional devices.

Electronic structure calculations revealed distinct characteristics between the two material families, highlighting their potential for different technological applications. The simple perovskites $CeBeO_3$ and $CeMgO_3$ were found to be narrow-bandgap semiconductors, with band gaps of approximately 0.73 eV and 0.51 eV, respectively, as obtained using the modified Becke–Johnson (mBJ) approximation, which offers a more reliable estimation of electronic band structures compared to standard GGA functionals. These relatively small gaps suggest that the $CeBO_3$ family is better suited for applications in the infrared (IR) or near-infrared (NIR) region, such as IR sensors, thermophotovoltaics, and optoelectronic devices operating at longer wavelengths, rather than ultraviolet (UV) optoelectronics. The electronic density of states (DOS) analysis showed that the conduction band minimum (CBM) is primarily composed of Ce-4f and O-2p states, while the valence band maximum (VBM) mainly consists of O-2p orbitals. This pronounced orbital separation reduces the likelihood of mid-gap defect states and promotes efficient charge transport, which is crucial for achieving high-performance electronic and optoelectronic functionalities.

In contrast, the double perovskites $K_2CuBiBr_6$ and $K_2AgBiBr_6$ exhibit band gaps of approximately 1.73 eV and 2.82 eV, respectively, as calculated using the mBJ approximation. The gap of $K_2CuBiBr_6$ falls within the ideal range for single-junction photovoltaic applications, enabling efficient absorption of visible light, whereas the wider gap of $K_2AgBiBr_6$ makes it more suitable for photodetectors and tandem solar cells as a top-cell absorber rather than for standalone photovoltaics. These properties are promising because they combine favorable optical absorption with the potential for high open-circuit voltages, which are essential for thin-film solar devices. Additionally, the hybridization between Bi-s and Br-d orbitals at the conduction and valence band edges contributes to strong optical transitions and facilitates exciton dissociation critical factors for enhancing solar energy conversion efficiency. Overall, the electronic structure results indicate that K_2BBiBr_6 compounds represent promising candidates for next-generation lead-free perovskite-based optoelectronic devices, offering an environmentally safer alternative without compromising performance.

The mechanical and elastic properties of the investigated compounds were also analyzed in detail to assess their suitability for different operational environments. $CeBeO_3$ exhibits high

stiffness with elastic constants of approximately C_{11} = 251 GPa, C_{12} = 126 GPa, and C_{44} = 106 GPa, leading to a bulk modulus (B) of around 168 GPa. $CeMgO_3$ shows similar behavior, albeit with slightly lower stiffness due to the larger ionic radius of Mg. These results confirm that $CeBO_3$ compounds are mechanically robust and capable of maintaining structural integrity under high pressure and temperature conditions, making them suitable for applications in harsh environments, such as aerospace electronics and radiation shielding.

The double perovskites, while mechanically less rigid than their Ce-based counterparts, offer significant advantages in terms of flexibility. For instance, $K_2CuBiBr_6$ exhibits a Poisson's ratio of approximately 0.34, indicating a high degree of ductility, whereas $K_2AgBiBr_6$, with a Poisson's ratio of around 0.18, strikes a balance between ductility and brittleness. This mechanical adaptability is essential for thin-film processing and for the development of flexible electronic and photovoltaic devices, where mechanical compliance is as important as electronic performance. The combination of structural stability and ductility in these compounds ensures their long-term durability under mechanical stress during device fabrication and operation.

The optical properties of these materials further highlight their complementarity and technological relevance. $CeBeO_3$ and $CeMgO_3$ display strong absorption in the ultraviolet region, with absorption edges near 250–300 nm, making them highly suitable for UV filtering, laser optics, and transparent electronic applications. By contrast, $K_2CuBiBr_6$ and $K_2AgBiBr_6$ show strong absorption within the visible spectrum, featuring absorption coefficients greater than 10^5 cm^{-1}.

Such strong absorption in the visible spectrum is crucial for achieving high-efficiency light-harvesting in solar cells and for enabling sensitive photodetection in optoelectronic devices. These optical characteristics, combined with the electronic and mechanical properties discussed earlier, clearly indicate the versatility and functional diversity of these lead-free perovskite systems.

The thermoelectric properties of the double perovskites add another dimension to their potential applications. At room temperature (300 K), $K_2AgBiBr_6$ exhibits a Seebeck coefficient of approximately 240 μV/K and maintains a relatively high electrical conductivity compared to $K_2CuBiBr_6$, resulting in a superior power factor. This suggests that $K_2AgBiBr_6$ could be utilized in waste heat recovery systems and thermoelectric energy conversion applications, particularly in scenarios where moderate power generation from low-grade heat sources is required.

The integration of these findings opens exciting possibilities for advanced device architectures. For example, a tandem solar cell design that combines $CeBO_3$-based layers as UV-protective coatings with K_2BBiBr_6 absorbers for visible-light harvesting could significantly enhance overall efficiency while improving device stability and longevity. Future research should therefore prioritize experimental validation of these theoretical predictions, optimization of material synthesis techniques, and defect passivation strategies to minimize non-radiative recombination losses. Additionally, nanostructuring approaches and strain engineering could be employed to further enhance the thermoelectric and optical properties of these compounds.

For the application of the materials studied in this thesis, the analysis of band edge positions using the absolute electronegativity method allowed a clear distinction between promising photocatalysts and ineffective compounds. The perovskites $CeBeO_3$ and $CeMgO_3$, although conductive, exhibit gaps that are too narrow and an unfavorable band alignment, rendering them unsuitable for water splitting. In contrast, the double perovskites $K_2CuBiBr_6$ and $K_2AgBiBr_6$ simultaneously satisfy the two fundamental criteria: a band gap within the visible range and favorable alignment with respect to redox potentials. These compounds thus emerge as strong candidates for H_2 and O_2 generation under visible-light irradiation. These results confirm the relevance of the electrostatic approach combined with numerical modeling for the rational screening of new photocatalysts.

By advancing the understanding of these materials and outlining clear directions for future work, this thesis contributes significantly to the ongoing effort to develop sustainable, high-efficiency, and environmentally responsible functional materials for a wide range of technological applications.

الملخص: تتناول هذه الأطروحة دراسة نظرية لمركبات البيروفسكايت البسيط $CeBO_3$ (B = Be, Mg) **والبيروفسكايت** المزدوجة K_2BBiBr_6 (B = Cu, Ag) باستخدام نظرية دالة الكثافة (DFT) بطريقة FP-LAPW المطبقة في برنامج Wien2k. تم تقييم الاستقرار البنيوي عبر عامل غولدشميت وطاقات التشكيل، كما جرى تحليل الخواص الإلكترونية، المرنة، البصرية والحرارية الكهربائية بشكل معمق. أظهرت النتائج أن هذه المركبات الخالية من الرصاص تتمتع باستقرار بنيوي جيد، امتصاص بصري مرتفع، وأداء حراري كهربائي واعد، مما يجعلها مرشحة لتطبيقات في مجال الطاقة، الأجهزة البصرية الإلكترونية والأنظمة المدمجة.
الكلمات المفتاحية: بيروفسكايت، FP-LAPW، DFT ، الخصائص البصرية، الخصائص الحرارية الكهربائية

Abstract: This thesis focuses on the theoretical study of simple perovskites $CeBO_3$ (B = Be, Mg) and double perovskites K_2BBiBr_6 (B = Cu, Ag) using Density Functional Theory (DFT) within the FP-LAPW method implemented in Wien2k. Structural stability was assessed through Goldschmidt's tolerance factor and formation energies, while electronic, elastic, optical, and thermoelectric properties were systematically analyzed. The findings reveal that these lead-free perovskites combine good structural stability, strong optical absorption, and interesting thermoelectric performance, making them promising candidates for energy, optoelectronic, and embedded system applications.
Keywords: Perovskite, DFT, FP-LAPW, optical properties, thermoelectric properties.

Résumé: Cette thèse est consacrée à l'étude théorique des pérovskites simples $CeBO_3$ (B = Be, Mg) et pérovskites doubles K_2BBiBr_6 (B = Cu, Ag) à l'aide de la théorie de la fonctionnelle de la densité (DFT) appliquée dans la méthode FP-LAPW avec le code Wien2k. La stabilité structurale a été évaluée à travers le facteur de tolérance de Goldschmidt et les énergies de formation, tandis que les propriétés électroniques, élastiques, optiques et thermoélectriques ont été étudiées en détail. Les résultats obtenus montrent que ces pérovskites sans plomb possèdent une bonne stabilité structurale, une absorption optique élevée et des performances thermoélectriques intéressantes, ce qui les rend prometteuses pour des applications dans les domaines de l'énergie, de l'optoélectronique et des systèmes embarqués.
Mots clés: Pérovskite, DFT, FP-LAPW, propriétés optiques, propriétés thermoélectriques.